

Diss. ETH No. 15965

Soil moisture determination with TDR: Single-rod probes and profile reconstruction algorithms

A dissertation submitted to the
SWISS FEDERAL INSTITUTE OF TECHNOLOGY ZÜRICH
for the degree of
DOCTOR OF TECHNICAL SCIENCES

presented by
MATHIS NUSSBERGER
Dipl. El.-Ing. ETH
born September 11, 1972
citizen of Zürich

accepted on the recommendation of
Prof. Dr. Werner Bächtold, examiner
Prof. Dr. Hannes Flühler, co-examiner
Prof. Dr. Kurt Roth, co-examiner

2005

Preface

This work was carried out in the context of a joint research project entitled “Measuring Spatially Resolved Soil Water Content using a Novel Single-Rod TDR Probe”. The project was jointly sponsored by the Microwave Laboratory (IFH), department of electrical engineering and by the Institute of terrestrial Ecology (IT Ö), department of environmental sciences, both at the Swiss Federal Institute of Technology (ETH) Zürich.

I am very much indebted to all the following individuals and institutions who contributed to the success of this study.

Prof. Dr. Hannes Flüehler and Prof. Dr. Werner Bächtold initiated the research project. They enabled me to carry out my studies with a maximum of scope and with all the support I needed. Hans-Ruedi Benedickter provided essential assistance in the Microwave Lab. Hans Wunderli helped me throughout countless trials and experiments, he inspired me with ideas and with his personal interest in the matter. Hanspeter Läser was invaluable in the way he met my wishes for unusual experimental setups. Prof. Dr. Kurt Roth was co-examiner of this work.

I am also grateful to the following people who helped this work in one way or another: Hannes Wydler, Mike Schwank, Patrick Lazzarotto, Gilbert Gradinger, Peter Lehmann, Robin Penfield.

Contents

- 1 Introduction 1**
 - 1.1 Soils and water 1
 - 1.2 Soil water content measurement methods 5
 - 1.3 Electrical characteristics of soils 6
 - 1.3.1 Magnetic permeability 6
 - 1.3.2 Electrical conductivity 7
 - 1.3.3 Permittivity 9
 - 1.4 Electromagnetic waves and transmission lines 12
 - 1.4.1 Harmonic electromagnetic waves in a homogeneous medium 12
 - 1.4.2 Wave propagation in layered media 14
 - 1.4.3 Two conductor transmission line 16
 - 1.4.4 Transmission line protruding a layered media 17
 - 1.4.5 Transmission line waves and free waves 18
 - 1.4.6 Single conductor waveguide 20
 - 1.5 Conventional soil water measurement with TDR 23
 - 1.5.1 Direct readout of the mean dielectric constant 23
 - 1.5.2 Direct readout of the electrical conductivity with TDR . . . 25
 - 1.5.3 TDR measurement systems 26
 - 1.6 Advanced TDR measurement evaluation 27
 - 1.6.1 The differential equation for the reflection coefficient of the nonhomogeneous transmission line 27
 - 1.6.2 Attempts to solve the Riccati equation 28
 - 1.6.3 Modelling the medium 30

- 2 Single-rod probes: sensitivity and calibration 35**
 - 2.1 Calculated properties of coated and uncoated SRP waveguides . . . 37
 - 2.1.1 Wave velocity 38
 - 2.1.2 Losses 39
 - 2.1.3 Electromagnetic fields 42
 - 2.1.4 3-D Simulations 44
 - 2.2 Waveguide coupler 46

2.2.1	Horn loss experiments	48
2.3	Realization of coated rods	50
2.4	Sensitivity analysis: SRP vs. TRP	53
2.4.1	Sensitivity of the probes in a quasi-homogeneous medium	53
2.4.2	Sensitivity of the probes to scattering objects	55
2.4.3	Conclusions regarding the sensitivity investigations	59
2.5	Calibration	61
2.5.1	Very fine grain material	62
2.5.2	Coarse grain material	62
2.5.3	Solid particles	62
2.5.4	Liquids	63
2.5.5	Gelating agents	64
2.5.6	Calibration with a vertically inhomogeneous medium	70
3	Profile reconstruction algorithms	73
3.1	Electric soil model	73
3.1.1	Coupling of water content and conductivity	74
3.2	Simulation of the TDR curve	76
3.3	Inclusion of limited signal rise-time	78
3.4	Distributed probe head transition	79
3.5	Optimization	80
3.5.1	Error functions	80
3.5.2	Parameter adaptation	82
3.5.3	Filtering of the difference function	84
3.6	Initialization of the layer variables	84
3.7	Laboratory experiment	86
3.8	Field experiment	87
3.9	Discussion and conclusion	91
4	Coplanar strips for TDR measurements	93
4.1	Theory	93
4.2	Simulations	96
4.3	Experiments	96
4.4	Discussion and conclusion	98
5	Outlook	101
A	Notation	109

Abstract

Efficient irrigation and fertilization, early detection of landslide risks, the monitoring of soil remediation processes and many other issues of soil physics require knowledge of the spatial water content distribution in the soil. Established soil water content measurement methods can only partially deliver the information needed. This work focussed on the improvement of the time domain reflectometry (TDR) method.

TDR probes consisting of one conducting rod and a wave mode converter are an alternative configuration which overcomes some of the disadvantages of conventional two-rod probes. Four different single-rod probes and a two-rod probe were examined for sensitivity to a small and a large conductive scatterer in their vicinity. The single-rod probes were assembled combining a small/large wave mode converter with an uncoated/coated rod. It was found that the volume sampled by single-rod probes is larger and more symmetrical than the volume sampled by a two-rod probe of equal size. A comparison of the mode converters showed a higher loss for the smaller converter but only a small difference concerning the spatial sensitivity. Coating the conducting rod with a high dielectric constant material reduces the spatial sensitivity. One of the single-rod probes and the two-rod probe were calibrated in a sand tank (particle size 0.08-0.2 mm) with volumetric water content up to $0.35 \text{ m}^3 \text{ m}^{-3}$. The calibration showed only small differences between the single-rod and the two-rod probe regarding the measured bulk dielectric constant.

TDR profile reconstruction algorithms reconstruct the water content along the probe from the recorded TDR trace. Available algorithms are restricted to specific soil classes. The more general approach of a multi-layer soil model with Debye parameters allows the inclusion of knowledge about the soil matrix and the soil-water exchange processes. The establishment of a relationship between local water content and pore water conductivity allowed the development of a profile reconstruction algorithm for this model. The new method is fast (a few minutes on an average laptop) and converges well for the laboratory tested case of a sand column with variable water content. In a field experiment, the correct water content profile was indicated without any further knowledge of the pore water conductivity.

Coplanar strips (CPS) attached horizontally to a container wall are an advantageous alternative TDR probe setup for laboratory column experiments. Contrary to con-

ventional two-rod probes protruding through the container wall into the column, CPS probes do not interfere with the medium in the container. A typical example for a CPS probe was studied theoretically and experimentally. 2-D field simulations allowed the establishment of a relationship between the measured apparent dielectric constant and the water content in the proximity of the CPS. Experiments with a sand column with variable water content confirmed these calculations. In principle, CPS conduct a different electromagnetic wave mode than protruding two-rod probes, but this difference was found to be negligible in the studied case.

Zusammenfassung

Effizientes Bewässern und Düngen, frühzeitiges Erkennen von Erdbeben-Risiken, Überwachen von Bodensanierungs-Prozessen und viele weitere Themen in der Bodenphysik verlangen Wissen über die räumliche Wassergehaltsverteilung im Boden. Etablierten Methoden für die Wassergehaltsmessung können dabei nur partiell die benötigten Informationen liefern. Diese Arbeit konzentrierte sich auf die Verbesserung der Time Domain Reflectometry (TDR) Methode.

TDR Sonden, die aus einem leitfähigen Stab und einem Wellen-Mode-Konverter bestehen, stellen eine alternative Konfiguration dar, die einige Vorteile gegenüber konventionellen Zweistabsonden aufweist. Vier verschiedene Einstabsonden und eine Zweistabsonde wurden bezüglich ihrer Empfindlichkeit auf ein kleines und ein grosses Metallobjekt in der Umgebung der Sonde untersucht. Die Einstabsonden wurden zusammengesetzt, indem ein kleiner/grosser Wellen-Mode-Konverter und ein beschichteter/unbeschichteter Stab kombiniert wurden. Es stellte sich heraus, dass das Messvolumen einer Einstabsonde grösser und symmetrischer ist, als das einer Zweistabsonde vergleichbarer Grösse. Ein Vergleich der Moden-Konverter zeigte einen höheren Konversionsverlust für den kleineren Konverter, aber die Differenz bezüglich der Empfindlichkeit war gering. Die Beschichtung des leitfähigen Stabes mit einem Material mit hoher Dielektrizitätszahl reduzierte die Empfindlichkeit. Eine der Einstabsonden und eine Zweistabsonde wurden in einem Sandtank (Partikelgrösse 0.08-0.2 mm) mit volumetrischem Wassergehalt bis $0.35 \text{ m}^3 \text{ m}^{-3}$ kalibriert. Die Kalibration ergab nur kleine Differenzen zwischen der Einstabsonde und der Zweistabsonde, was die gemessene Dielektrizitätszahl des Mediums betrifft.

Algorithmen zur Profilrekonstruktion mit TDR rekonstruieren den Wassergehalt entlang der Sonde von einer aufgezeichneten TDR Kurve. Verfügbare Algorithmen sind beschränkt auf gewisse Bodentypen. Der allgemeinere Ansatz eines Bodenmodells mit mehreren Schichten, die durch Debye Parameter beschrieben werden, erlaubt, Wissen über die Bodenmatrix und die Matrix-Wasser Austauschprozesse einzuschliessen. Das Aufstellen einer Beziehung zwischen lokalem Wassergehalt und Porenwasser-Leitfähigkeit ermöglichte die Entwicklung eines 'Rekonstruktionsalgorithmus' für dieses Modell. Die neue Methode ist schnell (einige Minuten auf einem gewöhnlichen Laptop) und konvergierte gut für das Beispiel einer Labor-

Sandsäule mit variablem Wassergehalt. Für ein Feldexperiment wurde das Wassergehaltsprofil dem Trend nach korrekt angezeigt, ohne weiteres, verfügbares Wissen über die Porenwasserleitfähigkeit.

Koplanare Streifen, welche horizontal an Wänden von Tanks angebracht werden, stellen eine vorteilhafte, alternative Konfiguration für Säulenexperimente im Labor dar. Im Gegensatz zu konventionellen Zweistabsonden, die durch die Tankwand in die Säule hineinragen, interferieren Sonden aus koplanaren Streifen nicht mit dem Medium im Tank. Ein typisches Beispiel für eine Sonde aus koplanaren Streifen wurde theoretisch und experimentell studiert. Zweidimensionale Feldberechnungen erlaubten, eine Beziehung zwischen der gemessenen Dielektrizitätszahl und dem Wassergehalt in der Sondennähe herzustellen. Experimente mit einer Sandsäule mit variablem Wassergehalt bestätigen diese Berechnungen. Im Prinzip führt eine koplanare Streifen-Sonde einen anderen elektromagnetischen Mode als Zweistabsonden, die ins Medium hineinragen, aber im studierten Fall ergab sich nur ein vernachlässigbarer Unterschied.

Chapter 1

Introduction

Due to rainfall and subsurface flow, the local soil water and air content are the dynamically varying state variables of the vadoze zone, that is the partly unsaturated region between the ground water table and soil surface. The local water content governs many important aspects in the agricultural practice, e.g. plowing time, fertilizer application or irrigation scheduling, and is critical for the stability of slopes, desalinisation, soil remediation and construction work. Current measurement methods, which are presented below, have - as all measurements - some imitations. There is a wide-spread interest for the improvement of such methods. This dissertation focusses on the improvement of soil moisture determination with time domain reflectometry (TDR). Chapter 2 renders new insights about the single-rod time domain reflectometry probe (SRP), introduced by Oswald et al. (2004). Chapter 3 presents a new algorithm for the spatial reconstruction of the soil water content from two-rod probe measurements, where a two-rod probe (TRP) is installed vertically into the soil. Chapter 4 is dedicated to a laboratory measurement technique, where two-rod probes inserted into a measurement tank are replaced by coplanar metal strips (CPS) attached to the tank wall. The following sections of chapter 1 cover the basics of soil water content measurements including a summary of elementary electromagnetics.

1.1 Soils and water

Soil as a typical porous medium is in the most simple model a composite of three phases: the solid soil matrix, liquid soil water, and gaseous soil air. The rigid solid soil matrix consists predominantly of mineral particles. Pore water encompasses water and dissolved chemicals. Soil air may have different compositions, but is generally inert. If the soil air is completely displaced by pore water, it is saturated, else the soil is unsaturated. The effective saturation, S_e , is expressed as a function

of θ , the volumetric water content:

$$S_e = \frac{\theta - \theta_r}{\theta_s - \theta_r} \quad \text{Saturation} \quad [\text{m}^3\text{m}^{-3}] \quad (1.1)$$

where θ_s is the volumetric water content at saturation and θ_r is the residual volumetric water content. It is often experimentally found that the maximum water content is smaller than the porosity. This is caused by air entrapment and the presence of very large pores which drain so rapidly that they cannot be saturated. The residual water content on the other hand is usually attributed to strongly sorbed water.

With the volume of soil water, V_w , and the volume of soil air, V_a , the total volumetric pore space in the rigid soil model is $V_0 = V_w + V_a$ and the volumetric fractions of the two fluid phases are

$$\theta = \frac{V_w}{V_0} \quad \text{Volumetric water content} \quad [\text{m}^3\text{m}^{-3}] \quad (1.2)$$

$$\eta = \frac{V_a}{V_0} \quad \text{Volumetric air content} \quad [\text{m}^3\text{m}^{-3}] \quad (1.3)$$

with θ , the volumetric water content, and with η , the volumetric air content. The porosity ϕ of the soil is equal to the sum

$$\phi = \theta + \eta \quad \text{Porosity} \quad [\text{m}^3\text{m}^{-3}] \quad (1.4)$$

The density of the solids is ρ_r (soil mass per volume of solids). The bulk density ρ_s (soil mass per bulk soil volume including pore space) is

$$\rho_s = \rho_r(1 - \phi) \quad \text{Bulk density} \quad [\text{kg m}^{-3}] \quad (1.5)$$

With the mass density of the fluid phase ρ_w , the gravimetric water content θ_g can be determined:

$$\theta_g = \frac{\rho_w}{\rho_s} \theta \quad \text{Gravimetric water content} \quad [\text{kg kg}^{-1}] \quad (1.6)$$

Cohesion of water (mutual attraction of fluid molecules) and especially adhesion (attraction of water molecules by solid surface) varies considerably in soils. The usually hydrophilic grain surfaces adsorb water molecules due van der Waals and electrostatic forces as well as due to hydrogen bonds. These water molecules are firmly bound at the surface (Stern, 1924). The thickness of the adsorbed water film depends on numerous factors such as temperature and vapor pressure in the soil, type of solids, amount of clay content, surface charge of the particles and cation allocation. In grainy materials, e.g. sand, the portion of adsorbed water is negligibly small.

Adsorption and desorption of soil water is a dynamic process. Menisci connecting adsorbed water of neighboring particles are formed by cohesive forces in the soil

pores, similarly as in cylindrical capillaries. The higher the water content of a soil, the more the capillary water outweighs the adsorbed water. Since the interaction between matrix and molecules of the water phase decreases rapidly with distance, the total energy of the pore water becomes dominated by forces between its molecules and by gravity.

In order to extract soil water in the course a drying process, forces must be applied against the binding connections. Since the connection strength is usually not directly measurable, an energy consideration is adopted to analyze the system. The potential is defined as the work, which is necessary, to transport a unit quantity of water in a force field from a given point to a point of reference. Water moves from points of higher potential to points of lower potential, until the difference of potential is vanished. The total potential ψ_w can be split up into partial potentials:

$$\psi_w = \psi_g + \psi_s + \psi_{tp} \quad \text{Total potential} \quad [\text{kg m}^{-1} \text{s}^{-2}] \quad (1.7)$$

The gravitation potential ψ_g describes the influence of the force of gravity on the soil water. The osmotic potential ψ_s measures the energy density required to add dissolved molecules. The tensiometer pressure potential ψ_{tp} is the energy density which is needed to add or remove soil water (including the dissolved molecules) in an isothermally, reversible way. This potential is the sum of the effects of surface adsorption, surface tension, air pressure, and hydrostatic pressure.

In the important special case of a rigid, unsaturated soil at constant air pressure, the only component of the tensiometer pressure potential is the energy required to remove water from the porous matrix to a free water state at a given elevation. Since this potential is solely determined by the soil matrix it is called the matric potential ψ_m , and in this special case

$$\psi_{tp} = \psi_m \quad (1.8)$$

Instead of the matric potential, the matric head may be used, which is defined as

$$h = \frac{\psi_m}{\rho_w g} \quad \text{Matric head} \quad [\text{m}] \quad (1.9)$$

with the gravitation constant g .

The soil water characteristic is defined as the relation between the matric potential ψ_m and the volumetric water content θ . Since this relationship is hysteretic, the desorptive curve $\theta_d(\psi_m)$, obtained by slowly and monotonically removing the water from an initially water saturated soil, is not identical to the the adsorption curve $\theta_a(\psi_m)$ obtained by the reverse process.

Air can only enter the porous medium after the matric potential has dropped below the air-entry value ψ_m^0 , which is determined by the largest pore at the surface of the soil. The decrease of the water content with increasingly negative matric potential is irregular, once air has entered the porous medium. Discontinuities result when

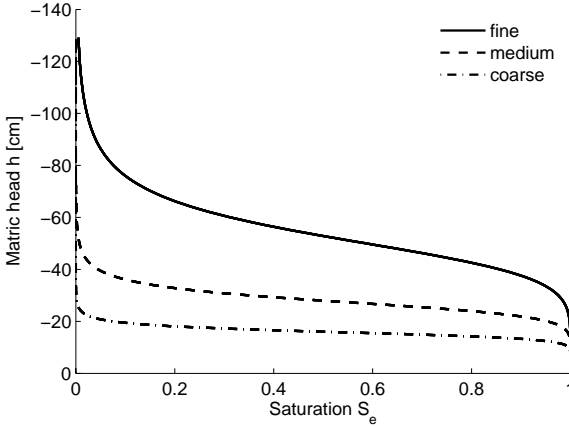


Figure 1.1: Soil water characteristics for the three sand types specified in Table 1.1.

pores are connected to the surface through thin channels. In these channels, a process, which is similar to the air entry into the entire medium, occurs.

The soil water characteristic is usually parametrized with Van Genuchten's equation

$$S_e(h) = (1 + (-\alpha h)^n)^{-m} \quad (1.10)$$

where α , n and m are positive parameters. The parametrization is often simplified by choosing

$$m = 1 - 1/n \quad (1.11)$$

which results in

$$S_e(h) = (1 + (-\alpha h)^n)^{-1+1/n} \quad (1.12)$$

Assumption 1.11 allows to explicitly express h as $h(S_e)$ which is required for solving the local mass balance equation. Given a set of pairwise measurements of θ and ψ_m , these parameters are chosen such that the deviation between $S_e(h)$ and the set of measured points is a minimum. The soil water characteristic is then described by the parameters θ_s , θ_r , α , n and eventually m .

The parameters for some quartzsands of different particle size are presented in Table 1.1 and their soil water characteristic is plotted in Figure 1.1.

Table 1.1: Van Genuchten parameters for some sand types (unpublished, data by Lehmann, P., Institute of Terrestrial Ecology, ETHZ).

Sand type	fine	medium	coarse
Grain diameter range [μm]	80-200	100-500	300-900
θ_s	0.35	0.32	0.32
θ_r	0.00	0.02	0.02
α [1/cm]	0.0196	0.0364	0.0631
n	6.63	9.19	12.0

1.2 Soil water content measurement methods

Soil water content can be measured directly or indirectly. Direct methods are those, where the water of the sample is removed and measured by evaporation, extraction or chemical reaction. Indirect methods are based on physical characteristics, which are influenced by soil moisture. A calibration function then relates the measured quantity to the soil water content.

The most accurate method for the measuring the water content is to determine of the weight loss by drying, termed gravimetric procedure. This procedure serves usually as a reference method, to which other methods are compared. A soil sample is taken in the field, weighed, oven-dried at 105 °C for 24 hours, and weighted again. The weight loss related to initial sample mass is the gravimetric water content θ_g . The main drawback of this method is the destructive sampling. An observation of water content changes over the time is practically not possible, except in case of spatially dense and intense sampling. The procedure is time and labor intensive and depends on the temperature distribution and air humidity in the furnace and on the sample container.

The most common indirect methods are time domain reflectometry, frequency domain reflectometry and resistivity measurements. They are based on the effect, that soil water heavily influences the electric and dielectric properties of soils. These methods are described in detail in the following sections. Their advantages are a fast measurement process with accurate estimation of water content except for the resistivity method and the possibility of automated measurements. Disadvantages are the cost of the equipment, the invasive character and a limited sampling volume. As these methods are wide-spread, any improvements in this field would have a large impact.

Alternatively, methods using radioactive sources, e.g. the fast neutron moderation and gamma ray attenuation, can be used. The neutron probe allows volumetric water content measurements, the gamma probe allows for density measurements and direct gravimetric measurement of soil water content. The drawbacks of these two methods are high costs and radiation safety concerns.

Remote sensing technologies as passive microwave remote sensing or ground penetrating radar may be used to measure soil water content. These non-invasive, larger-scale methods have the draw back of high equipment cost. The quantitative determination of soil water content from such measurements has not been routinely established yet.

1.3 Electrical characteristics of soils

This work focuses on measuring water content with time domain reflectometry, an indirect method which relies on determining soil electrical properties. Electromagnetic characteristics of materials are described by the constitutive parameters, permittivity ϵ , permeability μ , and zero-frequency conductivity σ . For stationary electromagnetic conditions the frequency dependance can be expressed by the complex permittivity ϵ and permeability μ

$$\epsilon = \epsilon' - j\epsilon'' \quad \text{complex permittivity [As/Vm]} \quad (1.13)$$

$$\text{and } \mu = \mu' - j\mu'' \quad \text{complex permeability [Vs/Am]} \quad (1.14)$$

If the permittivity and permeability of a material are normalized with respect to the permittivity and permeability of vacuum, ϵ_0 and μ_0 , respectively:

$$\kappa = \frac{\epsilon}{\epsilon_0} = \kappa' - j\kappa'' \quad \text{relative permittivity} \quad (1.15)$$

$$\mu_{\text{rel}} = \frac{\mu}{\mu_0} = \mu'_{\text{rel}} - j\mu''_{\text{rel}} \quad \text{relative permeability} \quad (1.16)$$

$$(1.17)$$

The conductivity σ is associated with the zero-frequency current. Losses due to polarization and due to conduction cannot be distinguished, as they are in-phase and are measured together. An “effective” imaginary permittivity can be defined as

$$\kappa''_{\text{eff}} = \kappa'' + \frac{\sigma}{\epsilon_0\omega} \quad \text{effective imaginary permittivity} \quad (1.18)$$

The ratio between κ''_{eff} and κ' is called the loss tangent:

$$\tan \delta = \frac{\kappa''_{\text{eff}}}{\kappa'} \quad \text{loss tangent} \quad (1.19)$$

1.3.1 Magnetic permeability

Permeability values for selected substances are presented in Table 1.2. Most soil constituents are either paramagnetic or diamagnetic. Therefore, from the point of view of wave propagation, the non-ferromagnetic assumption $\mu = \mu_0$ is appropriate in most cases.

Table 1.2: Real relative magnetic permeability μ'_{rel} of selected materials

Material	μ'_{rel}
<i>Diamagnetic, μ'_{rel} slightly < 1</i>	
water	0.99991
quartz (SiO ₂)	0.9999988
kaolinite	0.99999995-1.0000023
<i>Paramagnetic μ'_{rel} slightly > 1</i>	
montmorillonite (2.8% FeO, 3% Fe ₂ O ₃)	1.000026
illite (1.4% FeO, 3.4% Fe ₂ O ₃)	1.000034
shale	1.000005-1.0015
granite	1-1.004
hematite	1.002-1.003
<i>Ferromagnetic μ'_{rel} > 1</i>	
iron (commercial)	≈ 550 (may exceed 6000)

Source: Santamarina et al. (2001)

1.3.2 Electrical conductivity

Most soil minerals exhibit a very low conductivity relative to the conductivity of the fluid phase, see Table 1.3. The latter is composed of water and ions. It is an aqueous electrolyte. Hydrated ions are not electrically neutral. They are accelerated in the presence of an electric field up to a terminal velocity, which depends on the viscosity of the fluid. If the electrolyte is completely ionized, the molar conductivity of the electrolyte is the sum of the molar conductivities of the individual ions. In general, σ_{el} is

$$\sigma_{el} = \sum_i c_i \Lambda_i \quad \text{electrolyte conductivity} \quad [\text{S/m}] \quad (1.20)$$

where c_i [mol/m³] is the concentration and Λ_i is the molar conductivity of the i th ion. For a mono-ionic electrolyte

$$\sigma_{el} = c\Lambda \quad [\text{S}\cdot\text{m}^2/\text{mol}] \quad (1.21)$$

These equations are restricted to the case, where ion-ion interactions can be neglected, i.e. for low concentrations as those in fresh water environments (Santamarina et al., 2001).

In wet soils the conduction occurs within connected pore spaces, influenced by the porosity and the structure of the pore space. The continuity of the water phase is critical. Below a certain level of saturation, called the percolation saturation, the conductivity decreases abruptly (Santamarina et al., 2001).

Table 1.3: Electrical conductivity of selected materials

Material	Conductivity [S/m]	Material	Conductivity [S/m]
Quartz	$5.0 \cdot 10^{-15}$	Oil	10^{-11}
Calcite	10^{-14}	Pure water	10^{-6}
Glass	10^{-12}	Fresh water	10^{-3}
Granite	10^{-11}	Seawater	4
Kaolinite	10^{-8}		
Iron	10^7		
Aluminium	$3.7 \cdot 10^7$		
Copper	$5.9 \cdot 10^7$		

Table 1.4: Conductivity of NaCl solutions ($T = 20^\circ\text{C}$)

Concentration (mol/L)	Conductivity [S/m]
0.01	0.12
0.1	8.5
4.0	22.0

Ions in the counterion clouds near particle surfaces are mobile and can contribute to the conductivity. Soils with a large specific surface and negative surface charge, e.g. clays, may therefore exhibit considerable conductivity even when saturated with deionized water. This additional conduction term is called “surface conduction”. The broad range of particle shapes and sizes, as well as a high tortuosity in conduction paths limit the accuracy of physical models describing surface conduction.

For low ion concentrations and soils with low specific surface an approximate empirical relationship can be applied to estimate the conductivity:

$$\sigma_{el} = 0.15 \text{ TDS} \quad \text{approximate conductivity} \quad [\text{mS/m}] \quad (1.22)$$

with TDS, the total amount of dissolved salts in [mg/L], at $T = 20^\circ\text{C}$. Without considering surface conduction, Archie’s law relates σ_{el} , the porosity ϕ , the degree of saturation $S = \theta/\theta_s$ to the conductivity σ of the porous medium with a, c and m as fitting coefficients (m varies between 1 and 2.4, c is generally about 4 to 5)

$$\sigma = a\sigma_{el}S^c\phi^m \quad \text{Archie’s law} \quad [\text{S/m}] \quad (1.23)$$

1.3.3 Permittivity

Polarization occurs, when charges are moved out of some equilibrium state, the amount of polarization, expressed as \vec{P} , is equivalent to the vectorial sum of the n_d elementary dipoles $\vec{\mu}_d$ in the unit volume. The maximum polarization \vec{P}_0 is reached at zero frequency. Because of inertia of the charge carriers, polarization processes requires time. The polarisation \vec{P} is therefore in general not in-phase with the electric field \vec{E} . A frequency-dependent complex permittivity $\kappa = \kappa' - j\kappa''$ is used to capture both amplitude and phase information:

$$\vec{P} = \kappa \epsilon_0 \vec{E} \quad \text{Polarization} \quad [\text{As/m}^2] \quad (1.24)$$

The spectra of polarization mechanisms have the form of relaxation or resonance. If the charge is moved against a restoring force, a resonance spectrum results. This is the case for electronic and ionic polarization. Electronic polarization occurs in atoms, when the electron cloud is moved out of the equilibrium trajectory by an applied alternating electric field. The relative displacement is well below one angstrom. The polarization is resonant at ultraviolet frequencies. Ionic polarization occurs in molecules, when atoms are moved out of the equilibrium state. Ionic polarisation is resonant at infrared frequencies. Resonance polarization can be modeled as a single degree freedom system with a mass, a velocity dependent loss due to radiation and a spring representing the stiffness of electrical forces. The complex permittivity follows then as

$$\kappa = \kappa'_\infty + \frac{\kappa'_0 - \kappa'_\infty}{1 + 2j\nu \frac{\omega}{\omega_{res}} - \left(\frac{\omega}{\omega_{res}}\right)^2} \quad (1.25)$$

where κ'_0 and κ'_∞ are the real permittivities at frequencies well below and well above the resonant frequency ω_{res} , and ν represents the damping coefficient. Plotting the equation in the complex plane of κ , i.e. performing a Cole-Cole plot, results in a full circle.

In absence of restoring forces, e.g. when they vanish by diffusion or if the system is severely damped, the material exhibits a relaxation spectrum, which is the case for molecular, spatial, and double layer polarizations (as explained below). A typical relaxation equation is then given by Debye (1929):

$$\kappa = \kappa'_\infty + \frac{\kappa'_0 - \kappa'_\infty}{1 + j \frac{\omega}{\omega_{rel}}} \quad \text{Debye relaxation model} \quad (1.26)$$

where ω_{rel} is the characteristic relaxation frequency, which is the inverse of the relaxation time $\tau = 1/\omega_{rel}$. The Cole-Cole plot of relaxation is a half circle (cf. Figure 1.2). The intersections with the real axis are at the points κ'_0 and κ'_∞ . As the electromagnetic wave velocity is inversely proportional to the square root of the real permittivity, relaxation renders anomalous dispersion, which means increase in velocity with frequency.

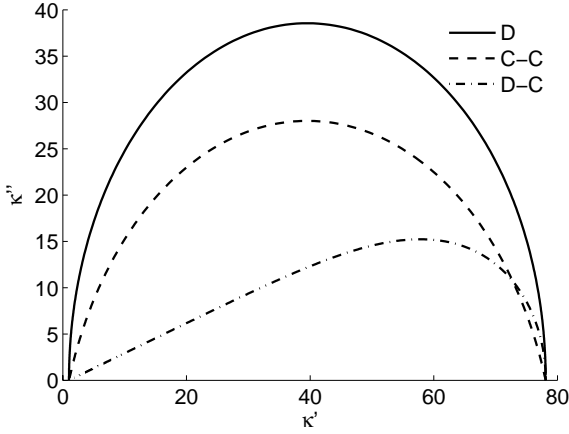


Figure 1.2: Cole-Cole plots of the real, relative permittivity κ' versus the imaginary, relative permittivity κ'' for free water according to the Debye (D), the Cole-Cole (C-C) and the Davidson-Cole (D-C) model of relaxation.

Soils with their complex structure exhibit multiple relaxation times, which follow a statistical distribution. Modifications to Debye’s equation capture this effect. Cole and Cole (1941) introduced a spread in relaxation times with the factor α :

$$\kappa = \kappa'_{\infty} + \frac{\kappa'_0 - \kappa'_{\infty}}{1 + (j\omega\tau)^{1-\alpha}} \quad \text{Cole-Cole relaxation model} \quad (1.27)$$

A skewed spread in relaxation times may be obtained with the Davidson and Cole Model (Hasted, 1973):

$$\kappa = \kappa'_{\infty} + \frac{\kappa'_0 - \kappa'_{\infty}}{(1 + j\omega\tau_a)^{\alpha}} \quad \text{Davidson-Cole relaxation model} \quad (1.28)$$

where τ_a is the characteristic value in the distribution of relaxation times and α shifts the semi-circle from the x-axis and reflects the spread in the relaxation times. Below the relaxation frequency, the permittivity κ'_0 is higher than the permittivity at frequencies above. Ultimately, $\kappa'_{\infty} = 1$, because of the inertia of the charge carriers.

Orientalional polarization

Orientalional polarisation occurs, when polar molecules are aligned by an external electric field. Only very few solids show relevant orientational polarization, as the movement of molecules is restricted. Orientalional polarisation is prominent

Table 1.5: Real relative permittivity κ' of selected materials

Material	κ' (upper MHz to GHz)
Quartz	4.2-5.0
Halite	5.7-6.2
Gypsum	5.0-11.5
Calcite	7.7-8.5
Mica	6.0
Water	78.5

in fluids, which consist of polar molecules. The polarity, i.e. the resulting dipole moment of a molecule depends on the shape of the molecule; the dipole moment of each bond is added vectorially. For example, the linear O-C-O arrangement in CO₂ results in a non-polar molecule; the opposite situation is the case for the unaligned hydrogen atoms in H₂O. Orientational polarization exhibits relaxation at microwave frequencies.

Electrolyte polarization

In electrolytes with low concentration, water is involved in hydrating ions, which results in a lower permittivity than that of free water. However, as the concentration of ions increases, ion pairs are formed which again increase the dipole moment per unit volume, and add an additional relaxation term with a longer relaxation time than that of pure water, according to the magnitude of the dipole moment of the ion pairs.

Spatial polarisation

Mixtures of constituents with different polarizability and conductivity exhibit spatial polarization as the result of charge accumulations at interfaces. The relaxation occurs within radio frequencies. Equations for the complex permittivity were first solved by Maxwell and Wagner. Therefore, spatial polarization is also known as Maxwell-Wagner interfacial polarization. Wet soils with a high specific surface (particle surface per volume) are strongly affected by spatial polarization.

The complex permittivity of soils

At low frequencies in the kHz range the permittivity spectrum reflects the composition of the solid and fluid phases, and their interactions. The effective imaginary permittivity κ''_{eff} in wet soils is then usually governed by conductivity losses. Orientational polarization losses start to prevail over conductivity losses at about 100

MHz. In the upper MHz and in the GHz band the permittivity mainly depends on the volume fraction of free water (the real relative permittivity of soil constituents in this frequency range is listed in Table 1.5). Various models were proposed to express the relationship between permittivity and volumetric water for fresh water environments in the frequency range $f = 10^8 - 10^9$ Hz:

$$\kappa' = \kappa_m^{1-\phi} \kappa_w^{\phi S} \quad \text{Lichtenecker's geometric mixing} \quad (1.29)$$

with porosity ϕ , degree of saturation S and κ_m, κ_w the relative dielectric constants of soil matrix and soil water,

$$\kappa'^{\alpha} = (1 - \phi)\kappa_m^{\alpha} + \theta\kappa_w^{\alpha} + (\phi - \theta)\kappa_a^{\alpha} \quad \text{Roth et al. (1990)} \quad (1.30)$$

with the relative dielectric constant κ_a of soil air, the volumetric water content θ , and the geometry factor $\alpha = -1 \dots 1$ (most soils $\alpha = 0.46 \pm 0.007$ according to Roth et al. (1990)), and the complex, refractive index model

$$\sqrt{\kappa'} = \phi(1 - S) + \phi S \sqrt{\kappa_w' + (1 - \phi)\sqrt{\kappa_m'}} \quad \text{Complex refractive index model} \quad (1.31)$$

For the use of soil water determination, where the fractions are not known, the empiric relationship proposed by Topp et al. (1980) has proven to perform well for bulk densities in the range $\rho_s = 1.35 - 1.5 \text{ g/cm}^3$ and low specific surface $A_s = 0 - 100 \text{ m}^2/\text{g}$, i.e. for most mineral soils

$$\kappa' = 3.03 + 9.3 \theta + 146.0 \theta^2 - 76.7 \theta^3 \quad (1.32)$$

for $f = 10^8 - 10^9$ Hz.

The temperature dependence of the dielectric constant of free water in the MHz and GHz range was empirically regressed as

$$\kappa' = 78.54(1 - 4.6 \cdot 10^{-3}(T - 25) + 1.2 \cdot 10^{-5}(T - 25)^2 - 2.8 \cdot 10^{-8}(T - 25)^3)$$

with temperature T in $^{\circ}\text{C}$ according to Weast (1988). The dielectric constant of free water changes from $\kappa' = 86$ at $T = 5^{\circ}\text{C}$ linearly down to $\kappa' = 80$ at $T = 20^{\circ}\text{C}$.

1.4 Electromagnetic waves and transmission lines

Time domain reflectometry relies on electromagnetic wave propagation, which is summarized in the following sections.

1.4.1 Harmonic electromagnetic waves in a homogeneous medium

Within the assumption of a linear time-invariant material behavior (which is applicable to soils regarding the high velocity of electromagnetic waves), any discrete

signal can be Fourier transformed and expressed as the summation of sinusoids. It is thus sufficient to analyse the stationary case of harmonic field vectors, and the following complex notation for the electric field vector \vec{E} can be applied:

$$\vec{E}(\vec{r}, t) = \operatorname{Re}(\underline{\vec{E}}(\vec{r}) e^{j\omega t}) \quad (1.33)$$

$$\text{with } \underline{\vec{E}}(\vec{r}) = \vec{E}_0 \cdot e^{j\varphi} \quad \text{complex amplitude} \quad (1.34)$$

with the imaginary unit $j^2 = -1$. The magnetic field vector \vec{H} becomes:

$$\vec{H}(\vec{r}, t) = \operatorname{Re}(\underline{\vec{H}}(\vec{r}) e^{j\omega t}) \quad (1.35)$$

$$\text{with } \underline{\vec{H}}(\vec{r}) = \vec{H}_0 \cdot e^{j\varphi} \quad (1.36)$$

If we consider an isotropic, homogeneous medium with complex constitutive parameters ϵ, μ and σ (real-valued), the Maxwell equations are formulated as follows:

$$\begin{aligned} \nabla \times \vec{E} &= -j\omega\mu\vec{H} && \text{Faraday's law of induction} \\ \nabla \times \vec{H} &= j\omega\epsilon\vec{E} + \sigma\vec{E} && \text{Ampere-Maxwell's law} \\ \nabla \cdot \epsilon\vec{E} &= \rho && \text{Gauss' law of electricity} \\ \nabla \cdot \mu\vec{H} &= 0 && \text{Gauss' law of magnetism} \end{aligned}$$

Assuming no excess free charges $\rho = 0$. These relations can be rearranged to the Helmholtz equations

$$(\Delta - j\omega\mu\sigma + \omega^2\mu\epsilon) \vec{E}(\vec{r}) = 0 \quad (\Delta - j\omega\mu\sigma + \omega^2\mu\epsilon) \vec{H}(\vec{r}) = 0 \quad (1.37)$$

The Helmholtz equations have solutions of the form

$$\vec{E}(\vec{r}) = \vec{E}_0 e^{-j\vec{k}\vec{r}} \quad \vec{H}(\vec{r}) = \vec{H}_0 e^{-j\vec{k}\vec{r}} \quad (1.38)$$

which are traveling waves in the \vec{k} direction with full wave number

$$|k| = \sqrt{k_x^2 + k_y^2 + k_z^2} = \sqrt{\omega^2\epsilon\mu - j\omega\mu\sigma} \quad \text{Wave number} \quad [\text{m}^{-1}]$$

The wave number is complex and thus it can be written as a complex number as follows:

$$k = \beta - j\alpha \quad (1.39)$$

The variation of the electric field along the propagation direction is then

$$\vec{E}(\vec{r}, t) = \operatorname{Re}(\vec{E}_0 e^{-\alpha\vec{r}} e^{j\omega t - j\beta\vec{r}}) \quad (1.40)$$

where the first exponential describes the attenuation with distance according to the attenuation coefficient $\alpha = -\operatorname{Im}(k)$. On the other hand, $\beta = \operatorname{Re}(k)$ is the phase constant, describing the velocity of the wave:

$$v = \frac{\omega}{\beta} \quad \text{Wave velocity} \quad [\text{m s}^{-1}] \quad (1.41)$$

For a wave propagating in z-direction we find from Maxwell's equations

$$\nabla \times \vec{E} = -j\vec{k}_z \times \vec{E}_0 = -j\omega\mu\vec{H}$$

and

$$\nabla \times \vec{H} = -j\vec{k}_z \times \vec{H}_0 = (\sigma - j\omega\epsilon)\vec{E}$$

This means, that if $E_z \neq 0$ the wave mode must have $H_z = 0$ and if $H_z \neq 0$ the wave mode must have $E_z = 0$. Nonzero values for E_z and H_z , the field components in z-direction, are mutually exclusive. The case $H_z = 0$ is called “transverse magnetic” mode (TM), $E_z = 0$ is called “transverse electric” mode (TE) and $H_z = E_z = 0$ is called “transverse electromagnetic” mode (TEM).

In the case of a TEM wave, where \vec{E} and \vec{H} lie in the same plane perpendicular to the propagation direction, an impedance Z of a medium can be defined as the ratio of the electric to the magnetic field vector, which is simplified due to the Maxwell equations to

$$Z = \frac{E}{H} = j \frac{\omega}{|k|} \mu = \frac{c_0}{\sqrt{\kappa}} \quad \text{Impedance} \quad [\Omega] \quad (1.42)$$

For non-ferromagnetic materials, the electromagnetic impedance becomes

$$Z = \frac{c_0}{\sqrt{\kappa' - j(\kappa'' + \frac{\sigma}{\omega\epsilon_0})}} \quad (1.43)$$

If the medium is loss-less and non-ferromagnetic, then the impedance of the medium is real, and the fields \vec{E} and \vec{H} vary in-phase. Finally,

$$Z = \mu_0 c_0 = 377\Omega \quad (1.44)$$

is the characteristic impedance of vacuum.

1.4.2 Wave propagation in layered media

Soils in the vadose zone rarely represent a homogeneous dielectric medium. As the local water content varies, the spatial electric properties change. Maxwell's equations define the boundary conditions, that the electromagnetic fields \vec{E} and \vec{H} must fulfill at the interface between two media with different electrical properties. Condition for the normal component of \vec{E} :

$$\epsilon_1 E_{1\perp} - \epsilon_2 E_{2\perp} = \rho_s \quad (1.45)$$

with the amount of free surface charge ρ_s at the boundary. If there are no free charges in the media, the ratio $E_{2\perp}/E_{1\perp} = \epsilon_1/\epsilon_2$ and the normal components of \vec{E} are discontinuous.

Condition for the normal component of \vec{H} :

$$\mu_1 H_{1\perp} = \mu_2 H_{2\perp} \quad (1.46)$$

The normal components of \vec{H} are discontinuous, if the media have different permeabilities.

Condition for the tangential component of \vec{E} :

$$E_{1\parallel} = E_{2\parallel} \quad (1.47)$$

The tangential component of \vec{E} is continuous across the boundary.

Condition for the tangential component of \vec{H} :

$$H_{1\parallel} - H_{2\parallel} = J_{surf} \quad (1.48)$$

The tangential component of \vec{H} is discontinuous across the boundary by the amount of the surface sheet current that develops along the boundary. If the media have finite conductivities, then no surface sheet current J_{surf} can exist, in this case, the tangential component of \vec{H} is continuous across the boundary.

A vertically layered soil with homogeneous electric properties in horizontal direction is an often encountered case in the field. For a plane electromagnetic wave approaching the interfaces between two layers with normal incidence, a part of the energy is transmitted and part of it is reflected. The resulting fields in the two layers follow from the boundary conditions as:

$$(E_i + E_r)_{1\parallel} = (E_t)_{2\parallel} \quad (1.49)$$

$$(H_i + H_r)_{1\perp} = (H_t)_{2\perp} \quad (1.50)$$

where the subscripts 'i', 'r' and 't' refer to incident, reflected and transmitted, respectively. These are two equations with four unknowns, H_r, H_t, E_r, E_t . However, the magnetic field and the electric field in each medium are related by the impedance of the medium:

$$Z_1 = \frac{E_{i\parallel}}{H_{i\perp}} = \sqrt{\frac{\mu_0}{\epsilon_1}} \quad (1.51)$$

and

$$Z_2 = \frac{E_{t\parallel}}{H_{t\perp}} = \sqrt{\frac{\mu_0}{\epsilon_2}} \quad (1.52)$$

The resulting two equations with two unknowns are solved to obtain:

$$E_r = R E_i, \text{ where } R = \frac{1 - (Z_1/Z_2)}{1 + (Z_1/Z_2)} \quad \text{Reflection coefficient} \quad (1.53)$$

The reflection coefficient R is real-valued in loss-less media.

1.4.3 Two conductor transmission line

If a two conductor transmission line is embedded in a linear time-invariant dielectric material, any discrete signal can be Fourier transformed and expressed as the summation of sinusoids. It is sufficient to analyse the stationary case of harmonic signals, and the following complex notation for the voltage U can be applied:

$$U(z,t) = \operatorname{Re}(U(z) e^{j\omega t}) \quad (1.54)$$

$$\text{with } U(z) = U_0 \cdot e^{j\phi} \quad \text{complex amplitude} \quad (1.55)$$

with the imaginary unit $j^2 = -1$. The current I becomes:

$$I(z,t) = \operatorname{Re}(I(z) e^{j\omega t}) \quad (1.56)$$

$$\text{with } I(z) = I_0 \cdot e^{j\phi} \quad (1.57)$$

A cylindrical transmission line with a fixed cross-section shape can be modeled as a lumped circuit with

$$C' \quad \text{capacitance per meter [F/m]} \quad (1.58)$$

$$L' \quad \text{inductance per meter [H/m]} \quad (1.59)$$

$$R' \quad \text{resistance per meter } [\Omega/\text{m}] \quad (1.60)$$

$$G' \quad \text{conductivity per meter [S/m]} \quad (1.61)$$

$$(1.62)$$

The telegraph equations, derived from circuit analysis,

$$\frac{\partial^2 U}{\partial z^2} = (j\omega L' + R')(j\omega C' + G')U$$

$$\frac{\partial^2 I}{\partial z^2} = (j\omega L' + R')(j\omega C' + G')I$$

have solutions of the form

$$U(z,t) = U_0 e^{\pm\gamma z} \quad I(z,t) = I_0 e^{\pm\gamma z}$$

which are traveling waves in the $\pm z$ direction with the propagation constant

$$\gamma = \sqrt{(j\omega L' + R')(j\omega C' + G')} \quad \text{Propagation constant} \quad [\text{m}^{-1}]$$

The propagation constant is complex and thus it can be written as a complex number:

$$\gamma = \alpha + j\beta \quad (1.63)$$

The variation of the voltage along the transmission line is

$$U = U_0 e^{-\alpha z} e^{j(\omega t - \beta z)} \quad (1.64)$$

where the first exponential describes the attenuation with distance according to the attenuation coefficient $\alpha = \text{Re}(\gamma)$. On the other hand, $\beta = \text{Im}(\gamma)$ is the phase constant, describing the velocity of the wave:

$$v = \frac{\omega}{\beta} \quad \text{Wave velocity} \quad [\text{m s}^{-1}] \quad (1.65)$$

The ratio between the amplitudes U and I , derived from circuit analysis, turns out to be constant for a given frequency:

$$Z_w = \frac{U_0}{I_0} = \sqrt{\frac{R' + j\omega L'}{G' + j\omega C'}} \quad \text{Transmission line impedance} \quad [\Omega]$$

1.4.4 Transmission line protruding a layered media

A transmission line protruding a layered media, where the layers are perpendicularly orientated, can be divided into consecutive, connected transmission line sub elements with homogeneous dielectric environment. On one of these transmission line elements, the voltage at a certain location z is

$$U(z) = U_a + U_b \quad (1.66)$$

with U_a the complex amplitude of the forward travelling wave, and U_b the backward travelling wave. Similarly the current is

$$I(z) = I_a - I_b \quad (1.67)$$

with I_a the complex amplitude of the forward travelling current, and I_b the backward travelling wave, the impedance of the element is

$$Z = \frac{U_a}{I_a} = \frac{U_b}{I_b} \quad (1.68)$$

At the boundary of two transmission line elements no. 1 and no. 2, the voltage is the same for both elements:

$$U_{a1} + U_{b1} = U = U_{a2} + U_{b2} \quad (1.69)$$

where as the current must fulfill Kirchhoff's law of charge conservation, which becomes

$$I_{a1} - I_{b1} = I_{a2} - I_{b2} \quad (1.70)$$

Assuming a wave incident to the boundary from one side, e.g. from 1, the backwards travelling current and voltage of the second element are zero

$$U_{b2} = 0 \quad I_{b2} = 0 \quad (1.71)$$

The impedance at the boundary is therefore

$$\frac{U_{a2}}{I_{a2}} = Z_2 = \frac{U_{a1} + U_{b1}}{I_{a1} - I_{b1}} \quad (1.72)$$

according to the boundary conditions above. This can be modified to

$$Z_2 = \frac{U_{a1} + U_{b1}}{(U_{a1} - U_{b1})/Z_1} = Z_1 \frac{1 + U_{b1}/U_{a1}}{1 - U_{b1}/U_{a1}} = Z_1 \frac{1 + R}{1 - R} \quad (1.73)$$

with the reflection coefficient R defined as the voltage amplitude ratio of the forward- and backward traveling waves:

$$R = \frac{U_b}{U_a} = \frac{Z_2 - Z_1}{Z_2 + Z_1} \quad (1.74)$$

On the other hand, if the transmission line element no. 2 is supposed to be properly terminated $Z_{3,4,\dots,\infty} = Z_2$, the effective impedance Z_{in} at the input of transmission line no. 1 with length L becomes

$$Z_{in} = \frac{Z_2 + Z_2 \tanh \gamma_1 L}{1 + \frac{Z_2}{Z_1} \tanh \gamma_1 L} \quad (1.75)$$

according to the impedance transformation formula (Bächtold, 1994). This relation allows to subsequently concatenate all individual sections up to an equivalent system input impedance $Z_{in,sys}$. The reflection coefficient is then

$$R_{sys} = \frac{Z_{in,sys} - Z_{source}}{Z_{in,sys} + Z_{source}} \quad (1.76)$$

with Z_{source} the source impedance (usually 50Ω).

1.4.5 Transmission line waves and free waves

The electric and magnetic fields generated by a signal travelling on a two- or multiple conductor transmission line embedded in a single dielectric correspond to a valid solution for the Helmholtz equation for free waves, i.e. a special TEM wave. Because both waves must have the same attenuation and phase constants, the propagation constant is linked to the wave number

$$\gamma = \alpha + j\beta = jk \quad (1.77)$$

therefore

$$\gamma = \sqrt{j\omega\sigma\mu - \omega^2\varepsilon\mu} \quad (1.78)$$

For non-ferromagnetic materials with $\mu = \mu_0$, $\varepsilon = \varepsilon_0(\kappa' - j\kappa'')$ and σ :

$$\gamma = \frac{\omega}{c_0} \sqrt{-\kappa' + j\left(\kappa'' + \frac{\sigma}{\varepsilon_0\omega}\right)} = \frac{\omega\sqrt{\kappa'}}{c_0} \sqrt{-1 + j \tan \delta} \quad (1.79)$$

The term in parentheses is the effective imaginary permittivity κ''_{eff} . An electromagnetic wave propagates with the phase velocity:

$$v = \frac{\omega}{\text{Im}(\gamma)} = \frac{\omega}{\text{Im}(\sqrt{j\omega\sigma\mu - \omega^2\varepsilon\mu})} \quad (1.80)$$

The frequency ω remains in the equation, therefore the wave velocity is frequency dependent. Simplified relations can be obtained for special cases. For example if the medium is non-ferromagnetic, and polarization losses are much smaller than conduction losses ($\kappa'' \ll \sigma/\varepsilon_0\omega$) then

$$v = \frac{c_0}{\sqrt{\frac{1}{2}\left(\kappa' + \sqrt{\kappa'^2 + \frac{\sigma^2}{\varepsilon_0^2\omega^2}}\right)}} \quad (1.81)$$

Furthermore, if conduction losses are also ignored, $\sigma = 0$, then

$$v = \frac{c_0}{\sqrt{\kappa'}} \quad (1.82)$$

The averaging of the propagation velocity through a layered media with layers of thickness L changes depending on the ratio wavelength λ/L (Chan and Knight, 2001). In terms of permittivity, the averaging changes from refractive index averaging to arithmetic averaging with the transition zone occurring at $\lambda/L \approx 4$. For two layers with dielectric constants κ'_1, κ'_2 the effective dielectric constant κ'_{eff} for a wave, travelling through both media changes as

$$\frac{\lambda}{L} \geq 4 \quad (1.83)$$

$$\sqrt{\kappa'_{\text{eff}}} = \frac{c_{\text{tot}}}{L_{\text{tot}}} = \frac{\sqrt{\kappa'_1} + \sqrt{\kappa'_2}}{2} \quad \rightarrow \quad \kappa'_{\text{eff}} = \frac{\kappa'_1 + \kappa'_2}{2} \quad (1.84)$$

Schaap et al. (2003) demonstrated that the refractive index averaging regime is appropriate for most soils and TDR probe lengths.

The spatial attenuation coefficient is obtained from the propagation constant:

$$\alpha = \text{Re}(\gamma) = \text{Re}\left(\sqrt{j\omega\sigma\mu - \omega^2\varepsilon\mu^*}\right) \quad (1.85)$$

For non-ferromagnetic materials and $\varepsilon = \varepsilon_0(\kappa' - j\kappa'')$, the attenuation coefficient becomes

$$\alpha = \text{Re}\left(\frac{\omega}{c_0} \sqrt{-\kappa' + j\left(\kappa' + \frac{\sigma}{\varepsilon_0\omega}\right)}\right) = \frac{\omega\sqrt{\kappa'}}{c_0} \sqrt{\frac{1}{2}\left(\sqrt{1 + \tan^2\delta} - 1\right)} \quad (1.86)$$

Once again, losses are the combination of conduction and polarization. In the case of a low-loss medium, $\tan\delta \ll 1$ the attenuation coefficient can be simplified to

$$\alpha = \frac{\omega\sqrt{\kappa'}}{2c_0} \tan\delta \quad (1.87)$$

The impedance for a TEM transmission line can be calculated with quasi-static field analysis. A TEM mode has no field components in propagation direction. Therefore, the electromagnetic field distribution in a plane perpendicular to the transmission line is solely defined by the charges on the conductors in the same plane. This poses a static, 2-D electromagnetic problem. There are various ways to solve such problems analytically and numerically (Ramo et al., 1993). In the case of a two-rod transmission line, the impedance becomes

$$Z = \frac{120}{\sqrt{\kappa}} \operatorname{arcosh} \frac{D}{d} [\Omega] \tag{1.88}$$

with conductor diameter d and distance between the centers of the conductors D .

1.4.6 Single conductor waveguide

A single conductor structure can act as a waveguide (Sommerfeld, 1899; Goubau, 1950). It primarily conducts a TM mode with $E_z \neq 0, H_z = 0$ (Stratton, 1941). Because of the cylindrical symmetry of the guide, E_z can be separated in the form

$$E_z = R(r)\Phi(\phi), \tag{1.89}$$

therefore Eq. 1.37 can be decomposed into

$$r^2 \frac{\partial^2 R}{\partial r^2} + r \frac{\partial R}{\partial r} + (k_T^2 r^2 - n^2)R = 0 \quad \frac{\partial^2 \Phi}{\partial \phi^2} + n^2 \Phi = 0. \tag{1.90}$$

The expression Φ is a harmonic differential equation with solution

$$\Phi(\phi) = a_n \cos n\phi + b_n \sin n\phi, \tag{1.91}$$

and the expression in R is a Bessel differential equation. The general solution of this linear differential equation of second order is expressed by the combination of two linearly independent partial solutions, e.g. (Abramowitz and Stegun, 1984)

$$R(r) = aH_n^{(1)}(k_T r) + bJ_n(k_T r)$$

This representation of the general solution is most meaningful from a physical standpoint of view. The Bessel function J of a real argument corresponds to a standing wave solution. The Hankel function H relates to a spreading wave, for an argument in the first quadrant of the complex plane (positive imaginary part), $aH_n^{(1)}$ describes an outgoing wave (which is exponentially damped).

For $k_T r$ in the first quadrant of the complex plane:

Function	$k_T r = 0$	$k_T r < 1$	$k_T r \gg 1$	$k_T r = \infty(1 + j)$
$J_n(k_T r)$	0	like $\pm(k_T r)^n$	like $\sin(k_T r)$	real-valued
$H_n^{(1)}(k_T r)$	$-\infty$	$\log(k_T r)$	like $e^{-k_T r}$	0

For a domain including $r = 0$, and an integer value of n all physically relevant solutions are of the form $R(r) = aJ_n(k_T r)$ alone. There (may) exist other solutions, but they are not physical. For a domain extending to $r = \infty$ all physically relevant solutions are given by $R(r) = aH_n^{(1)}(k_T r)$ because a non-zero field value at infinity would correspond to infinite power. It is only in a domain excluding 0 and infinity, where the physical solutions needs both linearly independent solutions as given above.

The full solution for the general case is

$$\begin{aligned}
 E_z(r, \phi) &= A_0 H_0^{(1)}(k_T r) + B_0 J_0(k_T r) \\
 &+ \sum_{n=1}^{\infty} \left(A_n H_n^{(1)}(k_T r) \cos n\phi + B_n H_n^{(1)}(k_T r) \sin n\phi \right. \\
 &\left. + C_n J_n(k_T r) \cos n\phi + D_n J_n(k_T r) \sin n\phi \right). \tag{1.92}
 \end{aligned}$$

A_n, B_n, C_n, D_n are parameters, n is the mode order.

The fundamental and the only mode of interest is $n = 0$. The higher modes $n > 0$ suffer from severe attenuation (Stratton, 1941). Knowing $H_z = 0$ and the function for E_z all field vector components can be calculated using the formulas given above. If a coated wire in a homogeneous medium is considered, the solution in the dielectric domain (subscript “d”), which does neither include $r = 0$ nor $r = \infty$ becomes

$$E_{z,d} = A_d \frac{k_z}{k_D} (H_0^{(1)}(k_D r) + a_d J_0(k_D r)) e^{j(\omega t - k_z z)} \tag{1.93}$$

$$E_{r,d} = j A_d \frac{k_z}{k_D} (H_1^{(1)}(k_D r) + a_d J_1(k_D r)) e^{j(\omega t - k_z z)} \tag{1.94}$$

$$H_{\phi,d} = j A_d \frac{k_d^2}{\omega \mu_d k_D} (H_1^{(1)}(k_D r) + a_d J_1(k_D r)) e^{j(\omega t - k_z z)} \tag{1.95}$$

with the parameters A_d, a_d , the transverse wave number $k_D = \sqrt{k_d^2 - k_z^2}$, and the full wave number $k_d = \omega \sqrt{\epsilon_d \mu_d}$.

Because $r = 0$ is included in the metal domain, the solution given above in the conductor is

$$E_{z,m} = A_m \frac{k_z}{k_M} J_0(k_M r) e^{j(\omega t - k_z z)} \tag{1.96}$$

$$E_{r,m} = j A_m \frac{k_z}{k_M} J_1(k_M r) e^{j(\omega t - k_z z)} \tag{1.97}$$

$$H_{\phi,m} = j A_m \frac{k_m^2}{\omega \mu_m k_M} J_1(k_M r) e^{j(\omega t - k_z z)} \tag{1.98}$$

with the parameter A_m , the transverse wave number $k_M = \sqrt{k_m^2 - k_z^2}$ and the full wave number $k_m = \sqrt{\omega \mu_m \sigma_m} e^{-j\pi/4}$.

In the soil medium, because $r = \infty$ is included in the domain, the solution is

$$E_{z,s} = A_s \frac{k_z}{k_S} H_0^{(1)}(k_S r) e^{j(\omega t - k_z z)} \quad (1.99)$$

$$E_{r,s} = j A_s \frac{k_z}{k_S} H_1^{(1)}(k_S r) e^{j(\omega t - k_z z)} \quad (1.100)$$

$$H_{\phi,s} = j A_s \frac{k_s^2}{\omega \mu_s k_S} H_1^{(1)}(k_S r) e^{j(\omega t - k_z z)} \quad (1.101)$$

with the parameter A_s , the transverse wave number $k_S = \sqrt{k_s^2 - k_z^2}$ and the full wave number $k_s = \omega \sqrt{\epsilon_s \mu_s}$.

In general, the parameters A_d, A_m, A_s , and a_d are not equal. The transverse wave numbers k_D, k_M and k_S are different. In contrast, to maintain a coherent wave front, the wave number in propagation direction, k_z , must be equal in all domains.

The boundary conditions (section 1.4.2) require that E_z is continuous across all boundaries, the same applies for H_ϕ , i.e. the ratio E_z/H_ϕ must be continuous at the boundaries. For a conductor with circular cross-section and radius r_c , this ratio becomes at the metal surface

$$\frac{\mu_m J_0(k_M r_c)}{k_m^2 J_1(k_M r_c)} = \frac{\mu_d (H_0^{(1)}(k_D r_c) + a_d J_0(k_D r_c))}{k_d^2 (H_1^{(1)}(k_D r_c) + a_d J_1(k_D r_c))} \quad (1.102)$$

from which follows

$$a_d = \frac{\mu_d k_m^2 J_1(k_M r_c) H_0^{(1)}(k_D r_c) - \mu_m k_d^2 J_0(k_M r_c) H_1^{(1)}(k_D r_c)}{\mu_d \mu_m J_1(k_D r_c) J_0(k_M r_c) - k_d^2 k_m^2 J_1(k_D r_c) J_1(k_M r_c)} \quad (1.103)$$

Similarly, from the boundary conditions at the dielectric-soil interface at radius r_d one obtains

$$a_d = \frac{\mu_d k_s^2 H_1^{(1)}(k_S r_d) H_0^{(1)}(k_D r_d) - \mu_s k_d^2 H_0^{(1)}(k_S r_d) H_1^{(1)}(k_D r_d)}{\mu_d \mu_s J_1(k_D r_d) H_0^{(1)}(k_S r_d) - k_d^2 k_s^2 J_1(k_D r_d) H_1^{(1)}(k_S r_d)} \quad (1.104)$$

Equating these two relations for a_d the transcendental eigenvalue equation for the only remaining variable k_z is obtained. For an uncoated rod, the eigenvalue equation simplifies to

$$\frac{\mu_m J_0(k_M r_c)}{k_m^2 J_1(k_M r_c)} = \frac{\mu_s H_0^{(1)}(k_S r_c)}{k_s^2 H_1^{(1)}(k_S r_c)} \quad (1.105)$$

Both eigenvalue equations have an infinite number of roots, a primary one which is near k_s and side roots, which belong to asymmetric (leaky) modes. Asymmetric modes are highly damped according to Stratton (1941). No physical solution can be found if the dielectric constant of the coating is lower than the dielectric constant

of the soil. For any practical case $\kappa'_d > \kappa'_s$ and thus $\kappa'_{rd} > \kappa'_r$ with $\kappa'_{rd} = \kappa'_d/\kappa'_0$ and $\kappa'_r = \kappa'_s/\kappa'_0$.

An uncoated single-rod probe for time domain reflectometry for measuring soil water content has been introduced by Oswald et al. (2004). The results of his work is summarized in the next chapter, along with the examination of a coated single-rod probe for soil moisture TDR.

1.5 Conventional soil water measurement with TDR

1.5.1 Direct readout of the mean dielectric constant

Based on the preceding sections, soil water content measurements with time domain reflectometry are possible due to several facts. With a suitable open-ended transmission line, the signal round trip time can easily be determined. The velocity of a signal on a transmission line is a function of the dielectric constant of the embedding medium, in the loss-less case $\kappa' = \sqrt{c_0/v}$. In the frequency range $f = 10^8 - 10^9 \text{ Hz}$ the real part of the dielectric constant of soils is mainly a function of the volumetric water content and can be described with an empiric relationship $\theta(\kappa')$, e.g. the one by (Topp et al., 1980). If the medium is inhomogeneous along a transmission line embedded in a soil, the refractive index averaging is applicable according to (Schaap et al., 2003), thus the effective dielectric constant represents the correct mean water content.

The mean volumetric water content of a soil, if it is homogeneous in the plane perpendicular to an inserted open-ended transmission line, can therefore be determined by measuring the travel time of a signal (Fellner-Feldegg (1969); Fellner-Feldegg and Barnett (1970); Hoekstra and Delaney (1974); Davis and Chudobiak (1975); Topp et al. (1980) for the main historical perspective). In principle, the signal used should be band-limited to $f = 10^8 - 10^9 \text{ Hz}$ (a chirp signal). However, this would require some kind of correlation technique for evaluation. Common TDR measurement equipment instead use a step signal, the reason for this is also historically (see section 1.5.3). Consequently, an evaluation procedure, which weights frequency components in the upper frequency range more is used (Baker and Allmaras, 1990; Heimovaara and Bouten, 1990). By means of regression, tangents are fitted to the probe head reflection slope and to the end reflection slope, Figure 1.3. They are intersected with tangents fitted to a certain range before these reflections. From these intersections the two-way travel time of the signal including the travel time through the head section is obtained. Preliminary measurements in water and air allow to determine the head section offset.

Common probe rod designs are focussed on minimizing disturbance of the soil, round cross-sections are chosen and the diameter of the conductors is kept as small as possible but large enough to avoid bending. Usual rod cross-section diameters are around 3 mm. The spacing of the rods is kept as small as possible to reduce

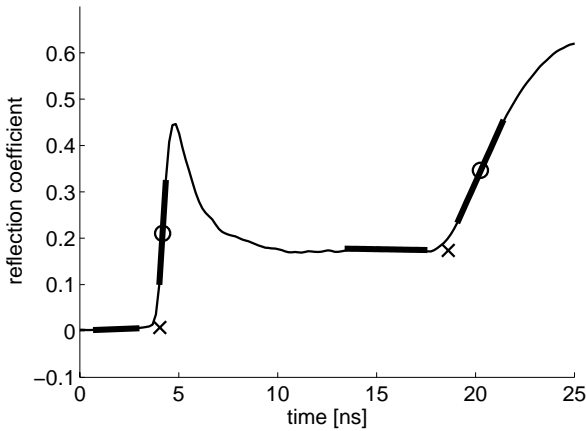


Figure 1.3: A typical soil moisture TDR trace. Indicated is the evaluation method of Baker and Allmaras (1990) and of Heimovaara and Bouten (1990): tangents are fitted to the head and to the end reflection through the turning points of the slopes, the time between the two intersections (marked with crosses) is read out.

probe size but large enough to cover the measured volume. A typical value for rod separation is 30 mm. In principle, a balun (balanced-unbalanced) transformer should be used at the connection of the coaxial cable from the measurement device to the probe rods, as the probe rod is a symmetric transmission line, whereas the coaxial cable is not. In general, this balun is omitted, because it reduces the measurement bandwidth. If no balun is used, even modes develop on the coaxial line. The latter can be suppressed with ferrite filters. An impedance transformer is not used commonly either, the usual algorithm to determine the travel time as described above even requires a reflection from the probe head.

Careful calibration can result in accurate ($\kappa' \pm 0.1$) measurements of permittivity (Robinson et al., 2003).

Despite the wide-spread use of soil water content measurement with the above summarized conventional TDR method, some fundamental issues remain unsolved:

- The evaluation procedure using tangent fitting is questionable for dispersive media, e.g. soils with high specific surface (clays) which exhibit considerable surface conduction and a relaxation frequency below 1 GHz due to the high amount of bound water, or for saline soils. Different frequency components of the step signal travel with different velocities. From inverse analysis of waveforms it is known, that the point at which the tangent lines intersect represents the fastest moving part of the signal (Weerts et al., 2001).

Topp et al. (2000) proposed to use the rise time of the reflection from the end of the probe to estimate this frequency, which they called “maximum passable” frequency f_{max} . However, experiments conducted by Or and Rasmussen (1999) showed a better match for a certain frequency below f_{max} (depending on the medium), which they termed “effective” frequency. The topic remains unsettled, but its importance has decreased in the light of most recent developments in terms of soil spectroscopy and profile reconstruction (see below).

- Even if the question of the “effective” frequency for dispersive soils could be answered precisely, the uncertainty would remain which calibration function to apply in such cases. Calibration functions obtained for low-loss media will overestimate water content, as the effect of slow-down due to high losses is attributed to an apparent higher real part of the permittivity. The calibration function by Topp et al. (1980) is known to fail for clays, e.g. for bentonite (Dirksen and Dasberg, 1993).

A known disadvantage of two-rod TDR probes is their limited sampling volume, the shape thereof is equivalent to the energy density distribution u around the probe (Knight, 1992; Petersen et al., 1995):

$$u = \frac{1}{2} \epsilon_0 \kappa'_s |\nabla \Phi|^2 \quad (1.106)$$

with Φ the electrostatic potential. In a charge free volume, Φ has to satisfy the Laplace equation

$$\nabla^2 \Phi = 0 \quad (1.107)$$

which can be readily solved using a two-dimensional field solver. Figure 1.4 shows the energy density distribution of a probe with conductor cross-section diameter of 3 mm and a separation of 30 mm between the rods in a homogeneous dielectric with $\kappa' = 10$. The probe is mainly sensitive at the surface of the rods and towards the center of the probe. The cross-section of the sampling volume has the shape of an “8”. Chapter 2 discusses the issue of sampling volume in detail.

1.5.2 Direct readout of the electrical conductivity with TDR

TDR can be used to measure bulk electrical conductivity in addition to permittivity (Giese and Tiemann, 1975; Nadler et al., 1991). Heimovaara and de Water (1993) used the reflection coefficient at infinite time r_∞ as a method of calculating the sample resistance:

$$R_{tot} = Z_c \frac{1 + r_\infty}{1 - r_\infty} \quad \text{Resistance } [\Omega] \quad (1.108)$$

where R_{tot} is the total resistance of the transmission line, Z_c is the source impedance of the reflectometer. This relationship is not exact, as r_∞ also depends on the material properties beyond the probe end. r_∞ has to be scaled according to the open and

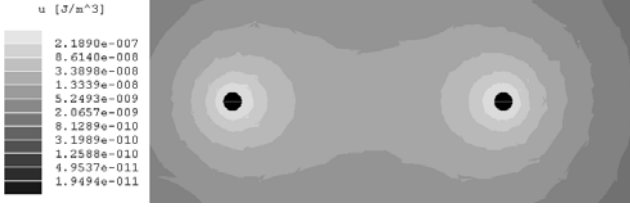


Figure 1.4: Energy density distribution of a two-rod probe in the cross-section plane. Rod diameter 3 mm, spacing between the centers of the conductors 30 mm, homogeneous dielectric with $\kappa = 10$. Obtained with Ansoft Maxwell 2D field solver.

short end reflection levels r_{open}, r_{short} (Castaglione and Shouse, 2003):

$$r_{scaled} = 2 \frac{r_{sample} - r_{open}}{r_{open} - r_{short}} + 1 \tag{1.109}$$

Performing good repeatable measurements for the open and short are difficult using conventional probes. Conductivity measurements with this method finally depend on the geometric factor of the probe conductors

$$\sigma = \frac{1}{R_{tot} g} \tag{1.110}$$

The geometric factor g for two rods with length L , conductor diameter d and distance between the centers of the conductors D can be approximated as (Robinson et al., 2003)

$$g \approx \frac{12.1 L}{\ln \left(\frac{D}{d} + \sqrt{\left(\frac{D}{d}\right)^2 - 1} \right)} \tag{1.111}$$

The accuracy of this approximation increases with longer probes, with larger distance D and with smaller conductor diameter d .

1.5.3 TDR measurement systems

Time domain reflectometry has traditionally been used for the detection of cable defects in communication and power line systems. In the 60ies, the same reflectometers appeared in scientific labs for the determination of material properties. One of these models, the Tektronix 1502, is still in use today. In the meantime reflectometers specifically designed for soil moisture measurements have become available. The device TDR100 from Campbell Inc. is now the standard reflectometer used at the Institute of Terrestrial Ecology. Table 1.6 lists the TDR instruments used in this work with some important properties.

Table 1.6: TDR measurement systems (examples)

Manufacturer	Tektronix	Tektronix	Campbell Scientific
Device	11801 SD24	1502(B,C)	TDR100
Signal rise time t_r [ps]	35	200	170
Bandwidth $(0.35/t_r)$ [GHz]	10	1.75	2.05
Pulse amplitude [V]	0.25	0.3	0.25
Weight [kg]	22.3	6.5	0.7
Size [cm]	60x45x24	44x32x13	21x11x6
Transport	mobile	portable	portable
Display options	CRT, PC	LCD, PC	PC
Datalogger interface	none	optional	included
Device output	waveform	waveform	waveform, σ , κ' , θ
Waveform size	512-5120	251	100-2048
Connection type	SMA	BNC	BNC
Power supply	AC	AC, battery	Battery

1.6 Advanced TDR measurement evaluation

1.6.1 The differential equation for the reflection coefficient of the nonhomogeneous transmission line

The difficulty of a direct inversion to obtain the generating impedance profile is more comprehensible by analyzing the differential equation for the local reflection coefficient. A local, differential reflection coefficient can be defined as

$$d\Gamma = \frac{Z + dZ - Z}{Z + dZ + Z} \approx \frac{dZ}{2Z} = \frac{1}{2}d(\ln Z) = \frac{1}{2} \frac{d}{dz}(\ln Z)dz$$

with the local impedance Z of a differential slice and the impedance of the next slice, $Z+dZ$, with a small difference dZ (Figure 1.5).

Applying the impedance transformation formula (Eq. 3.16), the input impedance of the differential slice becomes

$$Z'_{in} = Z(Z_{in} + jZ \tan \beta l) / (Z + jZ_{in} \tan \beta l) \quad (1.112)$$

$$= Z(Z'_{in} + dZ'_{in} + jZ \tan \beta dz) / (Z + j(Z'_{in} + dZ'_{in}) \tan \beta dz) \quad (1.113)$$

with the input impedance Z'_{in} of the slice after the regarded differential slice.

As $\beta l \ll 1$ the tangent can be replaced by the argument. Products of differential terms can be neglected. Finally one obtains

$$\frac{dZ'_{in}}{dz} = j\beta \left(\frac{Z'^2_{in}}{Z} - Z \right)$$

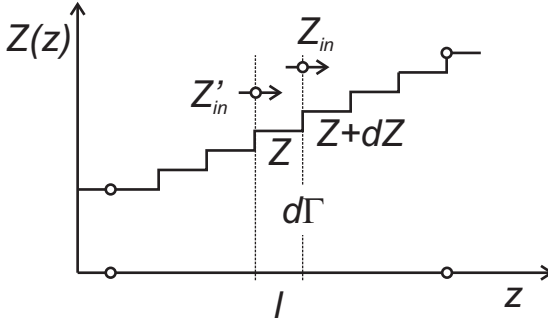


Figure 1.5: Illustration of the differential reflection coefficient on a nonhomogeneous transmission line.

On the other hand, with the definition of the reflection coefficient,

$$Z'_{in} = \frac{1 + \Gamma'_{in} Z}{1 - \Gamma'_{in}}$$

with its derivative

$$\frac{dZ'_{in}}{dz} = \frac{1 + \Gamma'_{in}}{1 - \Gamma'_{in}} \frac{dZ}{dz} + \frac{2Z}{(1 + \Gamma'_{in})^2} \frac{d\Gamma'_{in}}{dz}$$

By equating these two formulas and with $dZ/(Zdz) = d(\ln Z)/dz$, one obtains the differential equation for the reflection coefficient on a transmission line with variable impedance:

$$\frac{d\Gamma}{dz} = 2j\beta\Gamma - (1 - \Gamma^2) \frac{d(\ln Z)}{2dz}$$

This is a Riccati equation, with the non-linear term $(1 - \Gamma^2)$.

1.6.2 Attempts to solve the Riccati equation

Solving the Riccati equation would be the most direct way to extract more information from TDR waveforms. However, there is no general solution known for the Riccati equation. Attempts were made to inverse the Riccati equation by linearization. The simplest approach starts with neglecting the higher order term in the Riccati equation, $\Gamma^2 \ll 1$, then

$$\frac{d\Gamma}{dz} = 2j\beta\Gamma - \frac{d(\ln Z)}{2dz}$$

Issuing the variable substitution

$$\frac{d\phi}{dz} = 2\beta(z)$$

the differential equation can be integrated for a medium of length L

$$\Gamma_{in} = -\frac{1}{2} \int_0^{\phi L} e^{-j\phi} \frac{d \ln Z}{d\phi} d\phi$$

This integration corresponds to a Fourier transformation, if no reflections for $z < 0$ and $z > L$ are present. The solution is therefore

$$\Gamma_i = \frac{1}{2} \text{FT} \frac{d}{d\phi} (\ln Z)$$

with the Fourier transform operation FT. Inverting the equation with the inverse Fourier transform IFT leads to the impedance profile

$$\exp\left(2 \int_0^\phi \text{IFT} \Gamma_i du\right) = \exp\left(2 \int_0^\phi r'(t) dt\right) = \exp(2r(t)) = Z(t)$$

The obtained impedance profile has no imaginary parts. The method is therefore only applicable for very low-loss dielectric media. On the other hand, as described in the sections before, there are a multitude of loss effects apparent in soils in general. For water-content profiles in soils, the method was presented by Laurent and Pereira dos Santos (1994). The approach did not have any follow ups so far. Improved reconstruction would result if the quadratic term is not completely neglected. In practice, there is often a rather high reflection apparent at the probe head, e.g. $R = 0.6 \rightarrow R^2 = 0.36$, which is not small compared to 1. If the Riccati equation is divided by $(1 - \Gamma^2)$ it reads

$$\frac{1}{(1 - \Gamma^2)} \frac{d\Gamma}{dz} = \frac{2j\beta\Gamma}{(1 - \Gamma^2)} - \frac{1}{2} \frac{d(\ln Z)}{dz}$$

A truncated power series expansion for the non-linear term could be used as an approximation, e.g.:

$$\Gamma' = \Gamma / (1 - \Gamma^2) = \Gamma + \Gamma^3 + \Gamma^5 + \Gamma^7 \quad (1.114)$$

However, according to the substitution rules, Γ' has to satisfy

$$\frac{d\Gamma'}{dz} = \frac{1}{(1 - \Gamma^2)} \frac{d\Gamma}{dz}$$

The latter leads to

$$\Gamma' = \text{atanh } \Gamma = \Gamma + \Gamma^3/3 + \Gamma^5/5 + \sum_{n=3}^{\infty} \frac{\Gamma^{2n+1}}{(2n+1)}$$

which is in conflict with Eq. 1.114.

1.6.3 Modelling the medium

Since the direct inversion of the Riccati equation is impossible, a modelling approach has to be adopted.

Layer model in the time domain

The simplest model assumes a media with layers with frequency-independent properties. This assumption allows to conduct the analysis in the time domain entirely, assigning each transmission line element a voltage and a current. Applying a source impulse and propagating this pulse through the layer structure, the reflection waveform can be obtained. Yanuka et al. (1988) proposed this procedure for the case of a layered medium, as a method of simulating waveforms if the structure properties are known. A comparison between measured and simulated waveforms however showed, that the assumption of frequency-independent material properties clearly results in the inability to express dispersion effects common to soils.

A “layer-peeling” optimizing algorithm for the real-valued model was presented by Todoroff and Sun Luk (2001). A deliberate initial parameter distribution is corrected as the model is iterated: the initial impulse reaches a previously signal-free new segment at each next time step. Based on the multiple reflections before, the properties of the next slice can be calculated as the difference between the measured and the simulated trace. A fundamental problem exists, in that a change may be attributed to a permittivity change (water content) or an attenuation effect. Todoroff and Sun Luk (2001) calculated the profile as being loss-less (all changes attributed to water-content changes), but then were forced to use a filtering process with arbitrary hand-tuned parameters to get closer to the measured trace obtained from a field site measurement.

Earlier, Todoroff et al. (1998) and later, Oswald et al. (2003) approached the optimization problem of the frequency-constant model with genetic algorithms. Genetic algorithms are a sophisticated form of Monte Carlo simulations, where resulting profiles with a low fitting error are combined by a second random process and altered again. Genetic algorithms are the most general approach which is able to fit any parameter distribution. Consequently, Todoroff and Oswald were able to get an approximate fit to the measured profile without any assumption regarding the losses. However, the result was obtained at the cost of huge computative effort, as the convergence of genetic algorithms is extremely slow. Even with tomorrows computer power, genetic algorithms could only perhaps optimize the simplified frequency-constant model in reasonable time. With the many frequency dependent material properties of soils, and with conductivity having a dominant effect on the waveform we are clearly forced to adopt a more sophisticated model and an optimization process with a soil-characteristic physical background.

Frequency dependent single layer model

van Gemert (1973) proposed a procedure for a single layer model - a homogeneous soil - with frequency-dependent parameters. First, the time-domain reflection coefficient is measured without the probe rods attached. This reflection coefficient, denoted with $v_0(t)$, describes the cable tester, the cable and the probe head. Second, the reflection coefficient is measured with the probe rods attached. This response function $r(t)$ describes the entire system including the sample being measured. The relation between $v_0(t)$ and $r(t)$ is a convolution integral:

$$r(t) = \int_{-\infty}^t v_0(t - \tau)s(\tau)d\tau \quad (1.115)$$

where τ is the variable of integration and $s(t)$ the impulse response of the transmission line formed by the rods in the medium. Through Fourier transform, this relation is equivalent to the expression in the frequency domain

$$S_{11}(f) = \frac{R(f)}{V_0(f)} \quad (1.116)$$

with the scatter function S_{11} , with $R(f)$, the Fourier transform of $r(t)$, and with $V_0(f)$, the Fourier transform of $v_0(t)$. The impedance of the medium can then be derived as

$$Z(f) = Z_{\text{source}} \frac{1 + S_{11}(f)}{1 - S_{11}(f)} \quad (1.117)$$

with Z_{source} the source impedance of the reflectometer. For a two rod probe, the dielectric constant of the medium is then obtained by solving Eq. 2.10 for

$$\kappa = \left(\frac{120}{Z(f)} \operatorname{arcosh} \frac{D}{d} \right)^2 \quad (1.118)$$

To separate κ into permittivity and conductivity parts, Heimovaara (1994) and Friel and Or (1999) adopted the Cole-Cole relaxation model including losses

$$\kappa = \kappa'_{\infty} + \frac{\kappa'_0 - \kappa'_{\infty}}{(1 + j\omega\tau_a)^{\alpha}} - j \frac{\sigma}{\epsilon_0\omega} \quad (1.119)$$

to fit $\kappa(f)$ to scatter function data of different liquids. The optimization procedure depends on the model and the parameters chosen and is not critical, as the model has only a few parameters. The fitting may take place in the time domain, or, after Fourier transform, in the frequency domain.

Using inverse analysis of 2000 simulated TDR waveforms, Weerts examined the Debye model parameter sensitivity and determined correlations between model parameters and waveform characteristics. He found that conductivity has a strong influence on the general waveform character, whereas the end reflection slope steepness is mainly determined by the relaxation frequency.

Alternatively, a multiple section model may be used for the cable-head part of the measurement system. Lin (2003b) adopted the “layer-peeling” algorithm to the frequency domain for this purpose (see Chapter 3 for details). Because the materials involved in this part of the system can be assumed to be loss-less and to exhibit frequency-independent parameters a direct reconstruction is possible. The dielectric properties of the soil layer are assumed to follow a relaxation model. Lin (2003b) modeled the frequency-dependent dielectric permittivity of soil constituents (i.e., solid, air, water, and bound water) of two soil samples using the Debye model including losses

$$\kappa = \kappa'_{\infty} + \frac{\kappa'_0 - \kappa'_{\infty}}{1 + j \frac{\omega}{\omega_{rel}}} - j \frac{\sigma}{\epsilon_0 \omega} \quad (1.120)$$

by fitting in the frequency domain. He used the dielectric mixing model by Dobson et al. (1985) to obtain the parameters of the soil constituents. The method was confirmed by the experimental results as being superior to the scatter function method at high frequencies if an appropriate dielectric relaxation model was used.

Frequency dependent multiple layer model

A more realistic modelling fragments the probe part in cascaded transmission line elements. Each transmission line element, i.e. each layer, has its complex valued impedance Z_i . Based on the transformation formula Eq. 3.16 the input reflection coefficient in the time domain can be computed, if the impedances are known. Feng and Lin (1999) demonstrated that this approach can be accurate in terms of simulating TDR waveforms. They compared the waveform obtained from a two-layer sample with a wet and a dry part of thickness 10 cm each to simulated waveforms. The parameters of the layers, their complex, frequency-dependent impedance, were obtained by analyzing the layers separately, using a Cole-Cole model fitted to the scatter function, as explained above.

To summarize, recent developments in advanced evaluation of TDR measurements have shown that

1. the method of equivalent input impedance renders a correctly simulated TDR trace if the complex, frequency dependent impedances of the slices are known
2. a multisection model including sections for the probe head should be assumed rather than using the scatter function method. The loss-less head-section can efficiently be reconstructed with a “layer-peeling” algorithm.
3. The dielectric constant in the sections in the medium should be modeled with a relaxation model including losses

Chapter 3 details on the reconstruction technique further, based on these insights. To our knowledge for the first time, a method of optimization in case of a multilay-

ered, dispersive soil is described. The algorithm is applied to reconstruction of in situ field site profiles.

Chapter 2

Single-rod probes: sensitivity and calibration

This chapter perpetuates the investigations about single-rod probes for time-domain reflectometry, which were initialized by Oswald et al. (2004). It is especially focussed on the possibility of tailoring the radial sensitivity of a single-rod probe (SRP) by coating the rod with a high dielectric constant material. A further aim consisted in verifying the expected larger sampling volume for SRPs compared to two-rod probes (TRPs). Mode converters are needed to excite the correct SRP wave if the probe is used with a standard TDR measurement device. Two different mode converters were compared for their performance. The evaluation of SRP traces and the calibration of the probe are crucial issues for the practical use. It has been found, that the common algorithm for TRPs by Baker and Allmaras (1990) and Heimovaara and Bouten (1990) is also applicable to TDR traces obtained with an SRP. Several approaches were developed to gain an ideal calibration medium which has a tunable, homogeneous and time-stable dielectric constant in the range common to soils, i.e. $\kappa' = 3 \dots 25$. Though calibration was finally performed with an inhomogeneous sand-water mixture, a possible alternative is indicated where gelling agents are used to prevent drainage.

For later use throughout this chapter, the coordinate system is defined according to the Figures 2.1, 2.2 and 2.3. The main variables for the SRP are its length L_{SRP} , the diameter of the conductor d , the conductivity of the conductor σ_c , the coating thickness w_d , the coating dielectric constant κ'_d and the coating loss tangent $\tan \delta_d$. The radius of the conductor is $r_c = d/2$, the radius of the probe is $r_d = d/2 + w_d$. For the two-rod probe, d denotes the diameter of the conductors, D the distance from center to center of the conductors in the perpendicular plane and σ_c the conductivity of the rods.

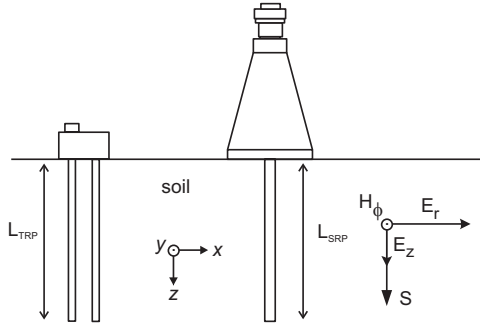


Figure 2.1: Cartesian coordinate system used in this chapter. The z-direction is parallel to the rod(s), the x-y plane is perpendicular to it. The length of the TRP rod is denoted by L_{TRP} , the length of the SRP rod is L_{SRP} .

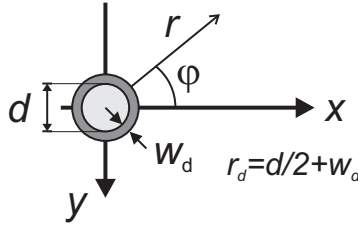


Figure 2.2: Geometric variables in the plane perpendicular to the SRP rod. Additional variables are: the conductivity of the rod σ_c , the relative dielectric constant of the coating κ'_d and the loss tangent of the coating $\tan \delta_d$.

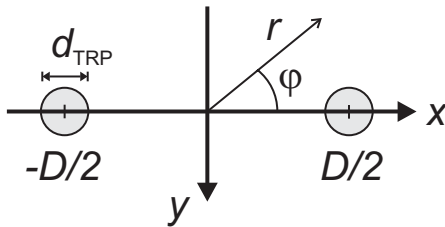


Figure 2.3: Geometric variables in the plane perpendicular to the TRP rods. An additional variable is the conductivity of the rods σ_c .

2.1 Calculated properties of coated and uncoated SRP waveguides

The electromagnetic properties of single conductor waveguides have been well studied for the environment of free space (Sommerfeld, 1899; Harms, 1907; Goubau, 1950). Oswald et al. (2004) examined these properties for uncoated waveguides in a homogeneous soil environment. Here, the properties of coated waveguides in a soil environment are investigated. For the purpose of comparison between uncoated and coated waveguides, some of the calculations of Oswald et al. (2004) are repeated.

At a given frequency f and in an environment with a homogeneous, complex, relative dielectric constant κ , a coated or uncoated single conductor wave guide is fully characterized by the wave number k_z , i.e. the number wave periods per unit length along the rod. The longitudinal wave number k_z is a result of a transcendental eigenvalue equation comprising f , κ , the conductor radius r_c , the conductivity σ_c of the conductor, the dielectric constant of the coating κ'_d (if any), and the coating thickness w_d .

For a chosen frequency f and for a given setup, k_z can be determined with Eq. 1.105. This equation has an infinite number of solutions but only the so called primary solution corresponds to an useful low-loss mode. All other solutions constitute asymmetric (leaky) modes which are highly damped and useless for practical purposes (Stratton, 1941). Due to the transcendental nature of Eq. 1.105 solutions can only be obtained with a numeric search process. However, this is a relatively simple task for the primary solution, where the real value of k_z is very close to the wave number of the soil medium, $k_z \approx k_s$, and the imaginary part of $k_z \approx 0$. Therefore, a good starting point for the search process is defined. A Matlab script was developed, which searches for the primary solution on a subsequently refined grid around the start point. The results obtained with this script were verified against literature (Sommerfeld, 1899; Goubau, 1950; Kaden, 1951) and with the results gained with the two-dimensional multiple multipole electromagnetic solver MaX-1 (Hafner, 1999).

For the investigations the conductor of the SRP is assumed to be a section of an infinitely long rod embedded in medium with a homogeneous, complex dielectric constant κ and a homogeneous permeability $\mu = \mu_0$. The parameters of the SRP were varied in following ranges:

- The diameter of the rod was varied in the range $d = 5 \dots 15$ mm corresponding to practical probes, where d is a trade-off between stability and disturbance of the soil.
- The conductivity of the rod was varied in the range $\sigma_c = 1.5 \dots 60$ MS/m, according to the possible metals used for the rod. Steel has a conductivity $\sigma_c = 1.75\text{-}8.7$ MS/m, aluminum has $\sigma_c = 35.38$ MS/m, copper has $\sigma_c = 58.0$ MS/m. Alloys have conductivities in the same range (Weast, 1988).

- The dielectric constant of the coating should be $\kappa'_d > \kappa'_s$ for the propagating wave (see theory section in the introduction). TDR probes are preferentially calibrated with water, therefore $\kappa'_d > 80$ is required.
- Two values were used for the coating loss tangent, $\tan \delta_d = 0.001$ and $\tan \delta_d = 0.1$. The former corresponds to a low-loss coating, the latter is a coating with high losses.
- The dielectric constant of the soil was varied in the range $\kappa'_s = 3..25$, where $\kappa'_s = 3$ corresponds to a dry soil and $\kappa'_s = 25$ to a water saturated soil.
- The soil loss tangent was varied in the range $\tan \delta_s = 0..0.1$, except for the calculation about the influence of very high losses on the wave velocity, where $\tan \delta_s = 1$ and higher was assumed.
- The frequency f was varied in the range $f = 0.3..3$ GHz, which is the main frequency band of the two most common TDR reflectometers, the Tektronix 1502 cable tester, and the TDR100 reflectometer (cf. section 1.6).

2.1.1 Wave velocity

The velocity of a harmonic wave on the guide is given by the real part of the wave number:

$$v = \frac{2\pi f}{\text{Re}(k_z)} \tag{2.1}$$

with the excitation frequency f . In Figure 2.4 v was plotted for the SRPs and a TRP defined in Table 2.1.

For all those probes, the v has a very similar dependence on κ'_s . Contrary, v is only slightly influenced by the other parameters. The Figure shows especially that the wave velocity on a SRP is approximately equal to the velocity of a wave on a TRP:

$$v_{\text{SRP}} \approx v_{\text{TRP}} = \frac{c_0}{\sqrt{\kappa'_s}} \tag{2.2}$$

	d [mm]	D [mm]	σ_c [MS/m]	w_d [mm]	κ'_d	$\tan \delta_d$
TRP	5	30	60			
SRP	5 / 15	—	1.5 / 60	0 / 0.1 / 0.5	80 / 100	0.001 / 0.1

Table 2.1: Probe configurations for the calculations of v and α of Figures 2.4 and 2.5. The SRP configurations correspond to all combinations of the indicated values. For an uncoated SRP $w_d = 0$.

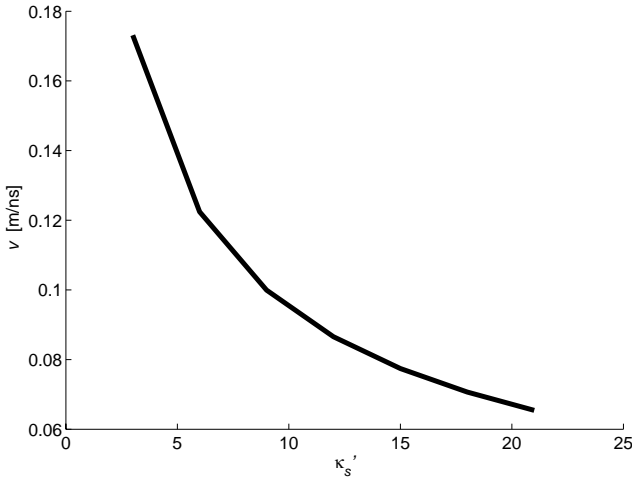


Figure 2.4: Wave velocity v vs. dependent on the dielectric constant κ'_s of medium with $\tan \delta_s = 0.001$ and with $\tan \delta_s = 0.1$ at the frequencies $f = 0.3, 1$ and 3 GHz for different SRP probes and a TRP as defined in Table 2.1.

For a TRP, the influence of the loss tangent on wave velocity is

$$\frac{v}{v_{\text{loss-less}}} = \sqrt{\frac{2}{\sqrt{1 + (\tan \delta_s)^2} + 1}} \quad (2.3)$$

with $v_{\text{loss-less}}$ the velocity in the lossless medium. Following from this equation, a loss tangent of $\tan \delta_s = 1.08$ results in a 10% reduction of the wave velocity. The same result was obtained numerically for the different SRP configurations defined above, if $\tan \delta_s = 1.08$. The influence of $\tan \delta_s$ on v is the same for the SRP as for the TRP.

2.1.2 Losses

The attenuation is caused by two contributions: the losses of the dielectrics in the medium and in the coating, and the resistive losses in the conductors. The losses of the dielectrics in [dB/m] are given by the imaginary part of the wave number:

$$\alpha_{\text{d,dB}} = 8.686 \operatorname{Im}(k_z) \quad (2.4)$$

For the resistive losses, the skin-effect resistance is calculated

$$R_{\text{skin}} = \sqrt{\frac{\pi f \mu}{\sigma_c}} \quad (2.5)$$

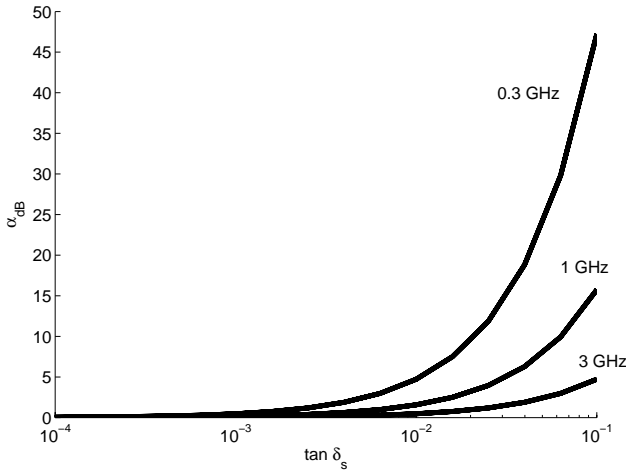


Figure 2.5: Attenuation $\alpha_{c,dB}$, including skin effect and dielectric losses vs. loss tangent $\tan \delta_s$ of the medium at the frequencies $f = 0.3, 1$ and 3 GHz for different SRP probes and a TRP as defined in Table 2.1.

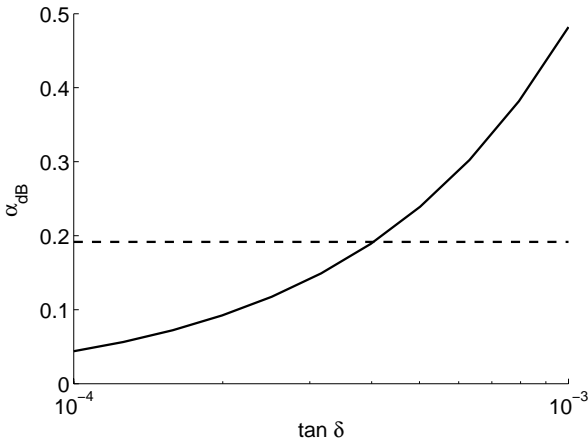


Figure 2.6: Attenuation $\alpha_{d,dB}$ of the dielectrics (coating and medium) and resistive (skin-effect) attenuation $\alpha_{c,dB}$ at 3 GHz vs. loss tangent $\tan \delta_s$ of the medium for the SRP with $d = 5$ mm, $\sigma_c = 1.5$ MS/m, $w_d = 0.5$ mm, $\kappa'_d = 100$, $\tan \delta_d = 0$. This SRP has the highest skin-effect losses (smallest d , highest σ_c) and the lowest attenuation in the dielectric (lowest $\tan \delta_d$, smallest w_d) of all coated SRPs in the parameter range. For $\tan \delta_s > 10^{-3}$, $\alpha_{d,dB} \gg \alpha_{c,dB}$.

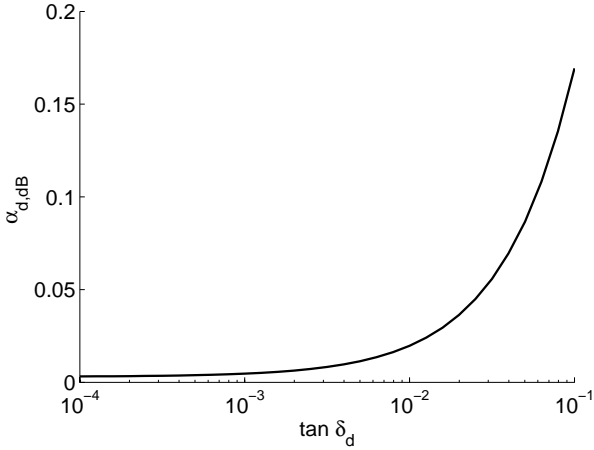


Figure 2.7: Attenuation $\alpha_{d,dB}$ of the coating at 3 GHz vs. loss tangent $\tan \delta_s$ of the coating for an SRP with $d = 5$ mm, $\sigma_c = 60$ MS/m, $w_d = 0.5$ mm, $\kappa'_d = 100$. Loss-less medium with $\kappa'_s = 3$. Compared with the total attenuation α_{dB} shown in Figure 2.5, the attenuation of the coating is negligible even at higher frequencies and for lossy coatings.

The resistance in [Ω/m] for a circular, cylindrical conductor is

$$R = \frac{R_{skin}}{2\pi a} \quad (2.6)$$

The attenuation due to the resistive losses is, in [dB/m],

$$\alpha_{c,dB} = 4.343 \frac{R}{Z} \quad (2.7)$$

with the wave impedance Z . Following Kaden (1951):

$$Z = \sqrt{\frac{\mu}{\epsilon}} \frac{1}{\log \left(0.68 \frac{1}{r_c \operatorname{Im}(k_z)} \right)} \quad (2.8)$$

In the case of the TRP, the resistance per unit length, R_{TRP} , is

$$R_{TRP} = \frac{2R_{skin}}{\pi d} \left(\frac{D/d}{\sqrt{(D/d)^2 - 1}} \right) \quad (2.9)$$

and the wave impedance

$$Z = \frac{120}{\sqrt{\kappa}} \operatorname{arcosh} \frac{D}{d} \quad (2.10)$$

both according to Ramo et al. (1993).

The total attenuation in [dB/m] is

$$\alpha_{\text{dB}} = \alpha_{\text{c,dB}} + \alpha_{\text{d,dB}}. \quad (2.11)$$

Figures 2.5, 2.6 and 2.7 show, that α_{dB} is dominated by the soil loss tangent $\tan \delta_s = \kappa'_s / \kappa''_s$ and becomes the same as the attenuation for two-rod probes.

2.1.3 Electromagnetic fields

According to the theory in the introduction, the SRP supports a transverse-magnetic mode with three non-zero field components, i.e., the azimuthal magnetic component H_ϕ , the radial electric component E_r , and the z-directed electric component E_z (Fig. 2.1). At the surface of the rod, E_z is several orders smaller than E_r . But as E_z decays slower than E_r as a function of r , the difference decreases. Up to a characteristic radius r_0 , the field components H_ϕ and E_r decay at rates inversely proportional to the radial distance r from the wave guide. For $r > r_0$ an approximately exponential law applies. In Figure 2.8 the field strengths are plotted for the example of an SRP with

d [mm]	σ_c [MS/m]	w_d [mm]	κ'_d	$\tan \delta_d$
5	60	0.5	100	0.001

at a frequency of 0.5 GHz and with the medium $\kappa'_s = 3$, $\tan \delta_s = 0$.

The local power density, defined by the Poynting vector $\vec{S} = \vec{E} \times \vec{H}$, can be split up in a longitudinal and a transverse component:

$$S_z = E_r \cdot H_\phi \quad (2.12)$$

$$S_T = E_z \cdot H_\phi \quad (2.13)$$

Inspecting Eq. 1.105 in the introduction, E_r and H_ϕ are found to be in-phase, but E_z has a $\pi/2$ phase shift. S_z therefore has a time-independent sign. It points in the same direction as the wave velocity and represents the power density transported by the wave. S_T in contrast has periodic sign, it is the power density transferred into and recovered from the electromagnetic fields around the probe.

Up to r_0 , a decay of H_ϕ and E_r with $1/r$ means a decay of S_z with $1/r^2$ (Fig. 2.9). According to Kaden (1951) the total power in the cross-section for $r > r_0$ is negligible. The radius r_0 can be approximated by calculating the negative inverse of the imaginary part of the transverse wave number

$$r_0 = \frac{-1}{\text{Im}(k_{Ts})} \quad (2.14)$$

with $k_{Ts} = \sqrt{k_s^2 - k_z^2}$ and the soil wave number $k_s = \omega \sqrt{\kappa'}/c_0$. Figures 2.10 and 2.11 show, that the characteristic radius depends significantly on f , κ'_s , on the ratio

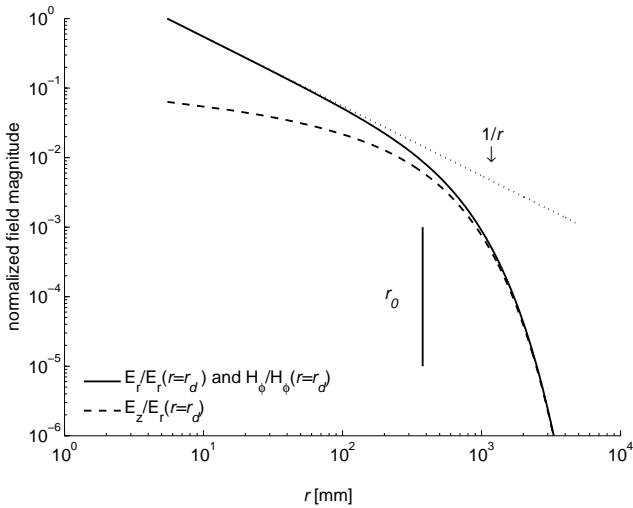


Figure 2.8: Magnitudes of the electric fields E_r and E_z , normalized to $E_r|_{r=r_c}$ and the magnitude of the magnetic field H_ϕ , normalized to $H_\phi|_{r=r_c}$. The magnitudes of the fields decay inversely proportional to the radius up to r_0 , indicated in the figure with a vertical line. At $r > r_0$ the decay is quasi-exponential.

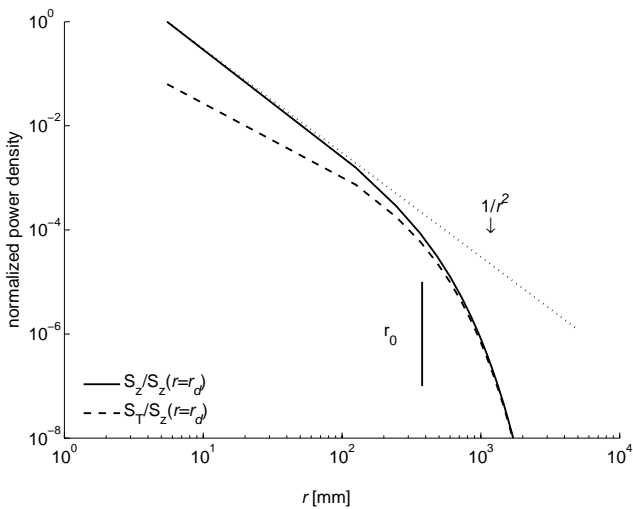


Figure 2.9: Magnitudes of the power densities S_z and S_r , normalized to $S_z|_{r=r_c}$. The magnitude of S_z decays inversely proportional to r^2 up to r_0 , indicated in the figure with a vertical line. At $r > r_0$ both power densities approach an exponential decay.

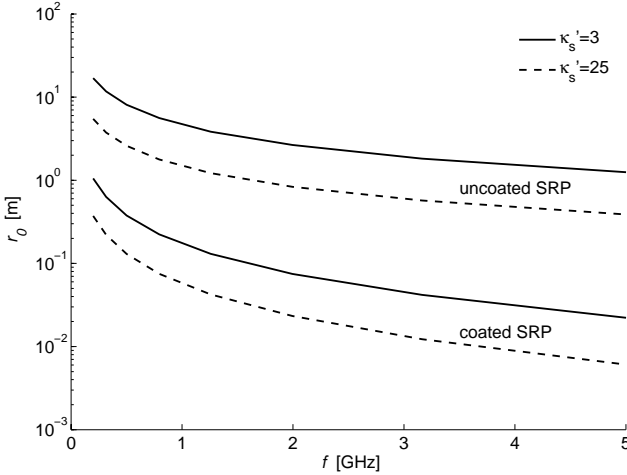


Figure 2.10: Characteristic radius r_0 as a function of f for $\kappa'_s = 3$ and 25. Uncoated and coated SRP with $d = 5$ mm, $\sigma_c = 60$. Coating: $w_d = 0.5$ mm, $\kappa'_d = 100$, $\tan\delta_d = 0.001$. The medium is lossless; frequency $f = 0.5$ GHz.

w_d/r_d and to a lesser degree on κ'_d . Above a certain value of w_d/r_d a further increase of w_d is without effect. A variation of the dielectric constant of the coating, from $\kappa'_d = 80$ to $\kappa'_d = 200$ has only a small effect on r_0 .

In the case of the uncoated rod, r_0 is very large. Therefore, S_z has already decreased to a negligible value before $r = r_0$. E.g., at 20 times the rod radius, S_z is 0.25% of the corresponding value at the surface of the rod.

2.1.4 3-D Simulations

The numeric solutions of Eq. 1.105 allow to study the undisturbed single-rod mode on a rod of infinite length. A 3-D simulation would be beneficial for the theoretic investigation of the electromagnetics for a rod of finite length embedded in an inhomogeneous medium. The 3-D numerical field analysis was performed with the software SEMCAD (Simulation platform for electromagnetic compatibility, antenna design and dosimetry, by Schmid & Partner Engineering AG, Zürich). SEMCAD is a versatile 3-D electromagnetic full-wave FDTD solver developed for problems with complex geometries and high inhomogeneity, e.g. for the portable-phone radiation dosimetry of the head. Unfortunately, the program version 1.7 available to the author did neither include a cylindrical TM-source nor a mode solver. The attempt to excite the SRP mode with the available line sources (dipoles) was not successful, a correct cylindrical TEM-mode, however, could be obtained. Consequently, the whole TDR system comprising the coaxial cable, the horn and the rod were

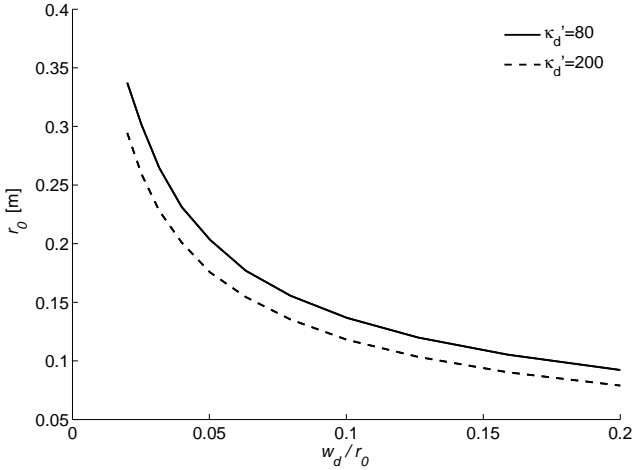


Figure 2.11: Characteristic radius r_0 as a function of the ratio w_d/r_c . Parameter: dielectric constant of the coating κ'_d . For an SRP with $d = 5$ mm, $\sigma_c = 60$ MS/m, $\tan\delta_d = 0.001$, in a loss-less medium with $\kappa'_s = 25$, at a frequency of $f = 0.5$ GHz. For the uncoated rod, $r_0 = 8$ m.

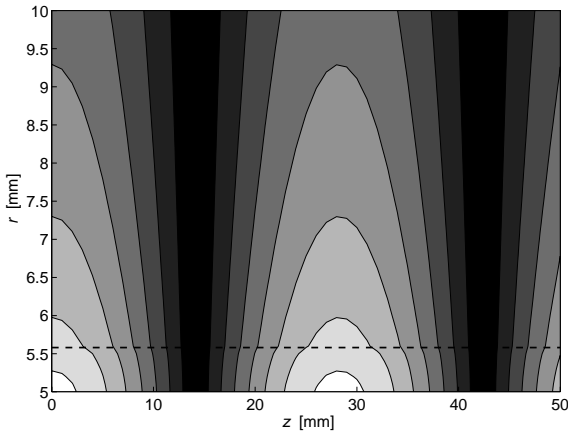


Figure 2.12: Contour plot of the magnitude of the electric field in radial direction away from the metallic surface of a 50 mm long section of an SRP with $d = 5$ mm, $\sigma_c = 60$ MS/m, $w_d = 0.5$ mm, $\kappa'_d = 100$, $\tan\delta_d = 0.001$, at a frequency of 3 GHz in a loss-less medium with $\kappa'_s = 3$. The lines connect points of equal magnitude. The dashed horizontal line marks the surface of the rod. On this boundary, the magnitude of the electric field is discontinuous.

modeled geometrically. However, even with the correct TEM mode in the coaxial cable, still no TM mode developed on the rod and the solver ran into numeric problems. The geometric significant dimensions span several orders of magnitude, from the discretization in the conductor in the 10^{-4} m range up to a simulation volume of several meters in radius for the uncoated rod. The discretization of the simulated volume must therefore include a large range of cell sizes to keep the size of the computational matrices low and the problem solvable within reasonable amount of time. The high irregularity of the mesh introduced small errors which were accumulated each iteration step and finally led to completely false results.

Though a correct 3-D electromagnetic modelling would have been instructive to understand the effects of an inhomogeneous medium, a simulation of the TDR reflection curve would have required an enormous computational effort, as the broadband TDR signal spans several frequency decades. The outcome of such a simulation would still have to be treated with considerable mistrust because of the model limitations. As 3-D simulations were neither very reliable nor necessary to proceed the investigations, but merely illustrative, they were finally dropped.

2.2 Waveguide coupler

Common TDR measurement systems have coaxial, transverse electromagnetic mode inputs and outputs. A mode converter must be used to couple a coaxial transmission line to an SRP. One of the simplest converters is a cone-shaped horn where the outer conductor of the coaxial cable is gradually extended (Fig. 2.13). Choosing the horn opening radius r_h is a trade-off: the launching loss and the reception loss at frequency f becomes small when $r_h \geq r_0$ (Goubau, 1950). Thus, optimum mode conversion at low frequencies requires very large horns. For practical sized horns a low-frequency cut-off must be accepted.

The conversion loss depends on the shape of the horn with its discontinuities: the transition from the coaxial cable to the tapered inner conductor and to the cone, and the transition from the horn end to the rod. Additionally, the coaxial TEM wave, when expanded in the horn, tends to form spherical waves (Goubau, 1954). The wave-front required at the horn opening, however, is plane, since the surface wave has plane phase surfaces (Fig. 2.14). Also, the field distribution at the opening of the horn does not match that of the surface wave. An estimation of the conversion loss would require an electromagnetic simulation with the exact geometric shapes in the converter range. The attempt to conduct such a simulation failed because of numerical problems (see previous section).

In this study, the performances of the two different horns depicted in Figure 2.13 were investigated. The small horn was available from the former work by Oswald et al. (2003). A second horn, with approximately double horn opening radius was designed by the author. This large horn was manufactured by pressing a thin metal sheet into the desired cone shape. The final radius of the rod is reached in the middle

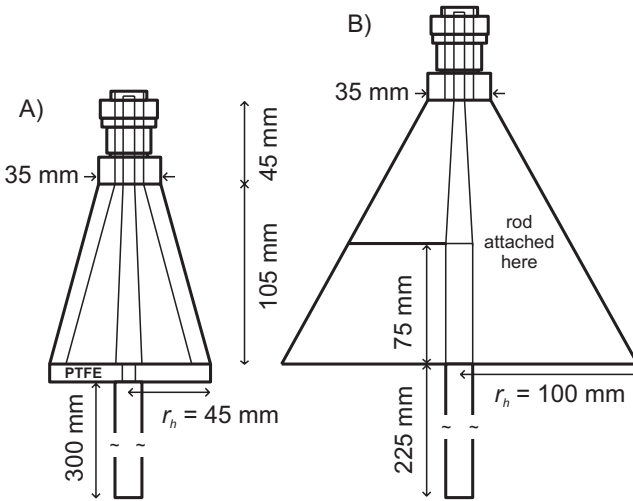


Figure 2.13: Linearly tapered horns as mode converters. A) An air-filled small horn with a tapering angle of 15.1° and an opening radius of 45 mm. The attached PTFE disc holds the conductor in place. The cone is made of a copper alloy and is 5 mm thick. B) A large horn with a tapering angle of 33.4° has an opening radius of 100 mm. The shell is made of a 0.5 mm thick copper alloy sheet. A plastic fixation keeps the rod in place at the center of the horn. The horns are shown with an attached rod of length 300 mm.

of the horn, as suggested by Goubau (1954). According to Goubau a discontinuity from the inner conductor of the horn to the attached rod causes significant radiation if located at the opening of the horn, and large standing waves, if located at the beginning of the horn.

As an alternative to the expensive and bulky horns, couplers comprising incompletely shielded coaxial cables have been studied (Kunz, 1972). The normally densely woven outer shielding of the coaxial cable is loosened successively towards the end of the outer conductor. The coaxial cable is tapered to the inner conductor, the dielectric and the coating of the coaxial cable. This represents a coated SRP rod in case of similar dielectric constants for the dielectric and the coating. As elegant this coupler type may seem, it has a crucial disadvantage from the perspective of TDR in being too narrowband. The bandwidth of the coupler increases with decreasing coupler length, but at the same time its input reflection coefficient rises. This trade-off renders the design of broadband couplers, with a constant efficiency from the sub-MHz range up to over 1.5 GHz, impossible. A constant conversion loss in the whole TDR band is important to maintain the slope steepness of the step signal and to preserve the high timing accuracy of the method. Therefore, no experiments with coaxial couplers were attempted.

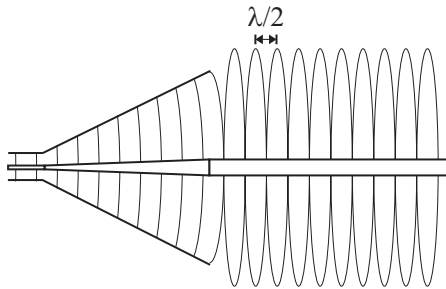


Figure 2.14: Sketched transition from the coaxial mode to the SRP mode.

2.2.1 Horn loss experiments

TDR signals on SRPs are attenuated by the two-way conversion loss of the launching and reception mode conversion. In Figure 2.15 the two-way conversion loss and the return loss of two different horn-shaped mode converters are compared. Two identical converters were attached to a copper alloy rod of 10 mm diameter and 1 m length, in air. The transmission loss of this setup is approximately equal to the two-way conversion loss of one mode converter. The transmission loss and the return loss were measured in the frequency range from 0 to 6 GHz using an HP 8702 network analyzer.

The results reveal a mean two-way conversion loss in the frequency band 1 to 3 GHz of 3.3 dB for the large horn and 6.5 dB for the small horn. The 10 dB attenuation limit occurs at 60 MHz for the large horn, at 195 MHz for the small horn. The return loss at the converter input (the mismatch) above 400 MHz is below -7 dB for both horns. As expected from the theory, the two-way conversion loss of the smaller horn is higher than for the large horn.

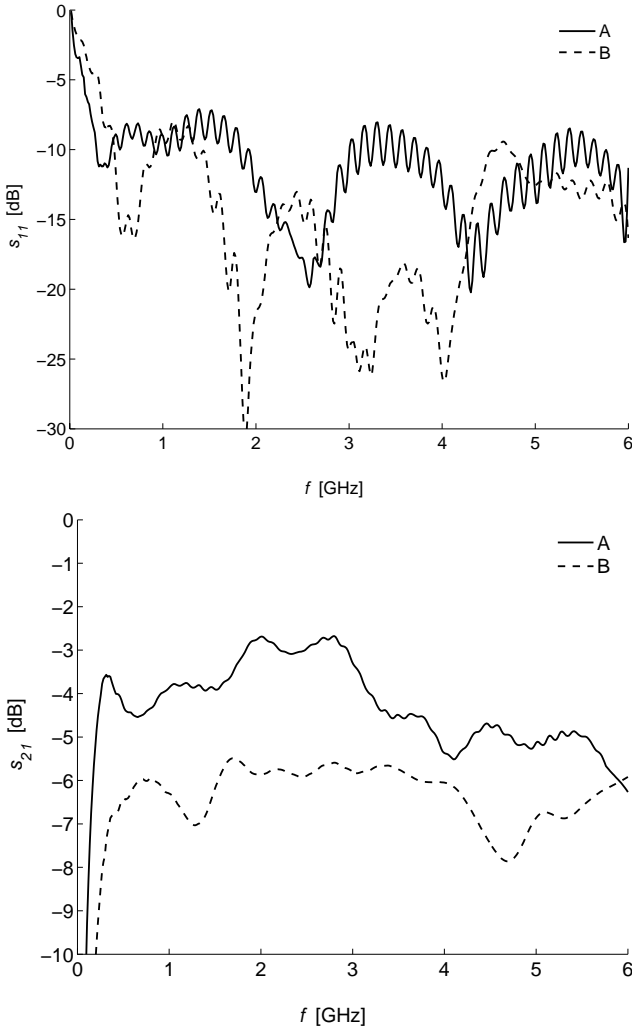


Figure 2.15: Reflection and transmission coefficients of a 1 m long copper alloy rod of diameter 10 mm which is (A) attached at both ends to the large horns with $r_h = 100$ mm, (B) attached to the small horns with $r_h = 45$ mm. The mean transmission loss in the frequency band 1 to 3 GHz is 3.3 dB for the large horns, 6.5 dB for the small horns. An attenuation of 10 dB occurs at 60 MHz for the large horns, at 195 MHz for the small horns. The horn types are specified in Figure 2.13.

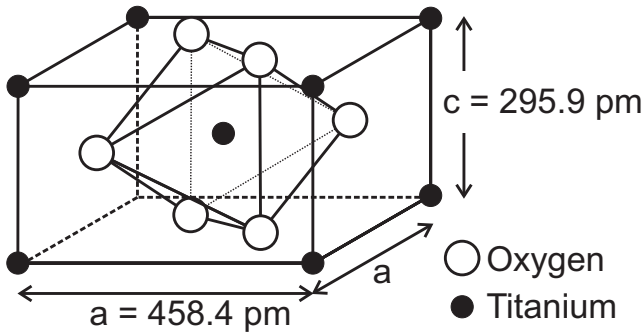


Figure 2.16: The crystal structure of TiO_2 in its rutile form (from Moulson and Herbert (2003)).

2.3 Realization of coated rods

In the introduction it was mentioned that no propagating mode is supported if the dielectric constant of the coating is lower than the dielectric constant of the soil. Soils usually exhibit a dielectric constant $\kappa'_s < 30$. However, TDR probes are preferentially calibrated in water, because of a higher accuracy than a calibration in air (Heimovaara and de Water, 1993). Therefore, the coating dielectric constant should be $\kappa'_d > 80$. On the other hand the above calculated properties of SRP show, that a pronounced field concentration effect with significantly lower r_0 compared to an uncoated rod can be achieved with a dielectric constant of the coating as low as $\kappa'_d = 80$ and a ratio $w_d/r_d = 0.2$.

Most solids have a low dielectric constant $\kappa' < 80$ (Weast, 1988). Solid dielectrics with higher permittivities (κ' around 100 and more) are based on special crystalline structures, which contain charged components able to rotate. A typical and prominent case are interlinked MO_6 groups, where M is either a quadrivalent ion such as Ti, Zr or Sn or a mixture of divalent, trivalent and pentavalent ions with an average charge of 4+ (Moulson and Herbert, 2003). The oxygen octahedra share corners, edges or faces in such a way that the O^{2-} ions form a close-packed structure (Fig. 2.16). TiO_6 octahedra are the most commonly found groups in medium- and high-permittivity dielectrics. The behaviour of rutile TiO_2 ceramic is typical of these types of dielectrics. TiO_2 in its pure rutile form typically exhibits a dielectric constant of $\kappa' \approx 100$ with negligible frequency dispersion up to over 10 GHz and a low loss tangent of $\tan \delta \approx 3 \cdot 10^{-4}$.

Coating a metal rod, which has a circular shaped cross-section, with a ceramic layer is a difficult task (according to a discussion with H. J. Schindler, ceramics section of the Swiss Federal Laboratories for Materials Testing and Research, EMPA, Dübendorf, Switzerland). Very thin layers in the nm range could be sputtered. For a

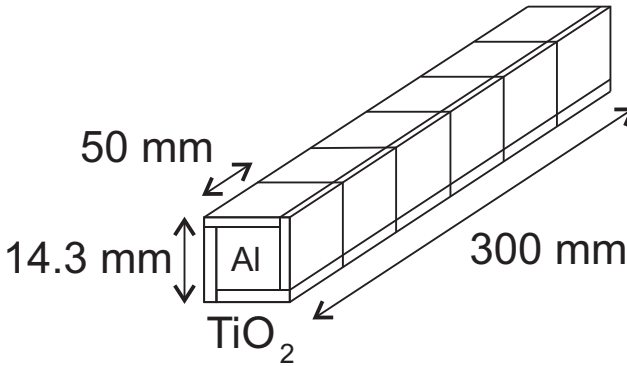


Figure 2.17: Coated probe: The metal conductor is a 300 mm long aluminum rod with square cross-section (side length 11.1 mm). The coating consists of TiO₂ high-dielectric substrate slices of size 50x12.7x1.6 mm³ ($\kappa'_d = 100$, $\tan \delta = 0.0023$, Trans-Tech Inc., USA) glued to the aluminium rod.

layer with thickness in the mm range this process would be far too time consuming and costly.

Fujiyasu and Pierce (2004) coated TRPs with an epoxy-ceramic nanocomposite containing barium titanate (40% of volume). Barium titanate as a sintered solid has a dielectric constant in the range 2000 to 4500. However, it is a ferromagnetic material ($\mu_{\text{rel}} > 1$), like most materials with very high permittivity (Moulson and Herbert, 2003). Moreover, its dielectric parameters are much more dispersive than in the case of MO₆ based dielectrics. The TRP rods were coated by briefly immersing them in the nanocomposite solution. When the coating was subsequently hardened in the oven, cracks developed, which were remedied by locally reapplying the composite with a brush. The dielectric constant of the coating obtained this way was found to be highly dispersive, decreasing from 77 at 10 kHz to 21 at GHz frequencies. The use of TiO₂ powder (99.9+ % crystalline rutile form, powder particle size $< 5\mu\text{m}$, Sigma-Aldrich product no. 224227) has been considered for an analogous coating procedure, however, a pressed solid block of the powder only exhibited a dielectric constant of $\kappa' = 13$.

Alternative ideas of filling a ceramic tube with liquid metal or heat shrinking the tube onto a metal rod would fail with a high probability because of different thermal expansion coefficients (H.J. Schindler, personal communication). A probe coated this way would also be rather susceptible to break when handled, due to the brittleness of the ceramics. Besides these technical problems, ceramic tubes in the sizes requested are not a standard product and would be very expensive. On the other hand, TiO₂ rutile ceramics are readily available in plate shape, with thicknesses in the mm range, from several manufacturers, e.g. from Trans-Tech (Adamstown, MD, USA), Resomics (muRata, Kyoto, Japan) or Dorado International (Seattle,

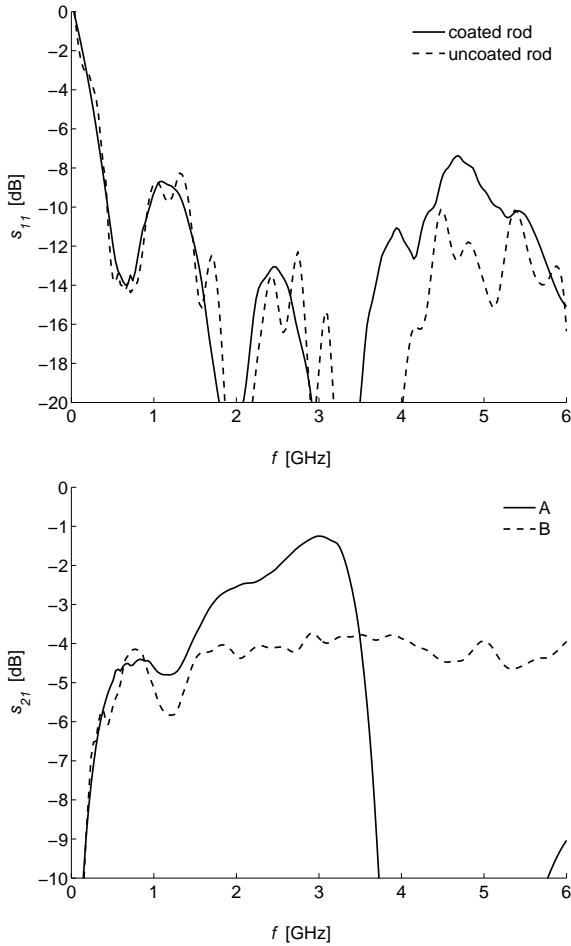


Figure 2.18: Reflection and transmission coefficient for the coated rod and for an uncoated rod with same metal cross-sectional area. Two small horns with $r_h = 45$ mm provided the coupling.

USA). Therefore a coated probe based on a rod with a square cross-section was constructed (Fig. 2.17). Preparatory measurements using an uncoated SRP with square cross-section (sidelength s) and an uncoated SRP with round cross-section (diameter s) yielded similar results.

2.4 Sensitivity analysis: SRP vs. TRP

2.4.1 Sensitivity of the probes in a quasi-homogeneous medium

The spatial sensitivity of an SRP is governed by the electromagnetic field distribution of the guided wave. Knight (1992) defined a weighting function w_0 , which relates the spatially distributed dielectric constant $\kappa'(\vec{r})$ to the apparent dielectric constant in the origin of a polar coordinate system in the perpendicular plane of a probe as

$$\kappa'_{\text{eff}} = \int_0^{2\pi} \int_0^\infty w_0 \kappa'(\vec{r}) r \, dr \, d\varphi \quad (2.15)$$

The latter is only valid for a quasi-homogeneous medium, i.e. the spatially distributed dielectric constant $\kappa'(\vec{r})$ exhibits only a small variance. In such a case the approximate weighting function is proportional to the power density and has total integral unity. If S_T and the flux outside the radius r_0 are neglected, the spatial weighting function for a single-rod probe in a quasi-homogeneous dielectric becomes

$$w_0(r, \varphi) = w_{\text{nf}} \cdot \frac{1}{r^2} \quad (2.16)$$

with the normalizing factor

$$\frac{1}{w_{\text{nf}}} = \int_0^{2\pi} \int_{r_c}^{r_0} \frac{1}{r^2} r \, dr \, d\varphi = 2\pi \ln \frac{r_0}{r_c} \quad (2.17)$$

Figure 2.19 compares this result to the weighting functions derived by Knight (1992) for the TRP, for both axes x and y as defined in Figure 2.3. Knight found that the general weighting function for a TRP is

$$w(r, \phi) = \frac{A^2}{\pi \ln \left((D/2 + A)/r_c \right) (A^4 - 2A^2 r^2 \cos 2\phi + r^4)} \quad (2.18)$$

with $A = \sqrt{D^2/4 - r_c^2}$. The comparison reveals that

- the SRP is as susceptible as the two-rod probe (Annan, 1977) to inhomogeneities like air-gaps occurring at the surface of the conductor. A larger conductor diameter reduces this effect.
- the value of the weighting function in the far field is higher for an SRP, indicating a larger influence range.

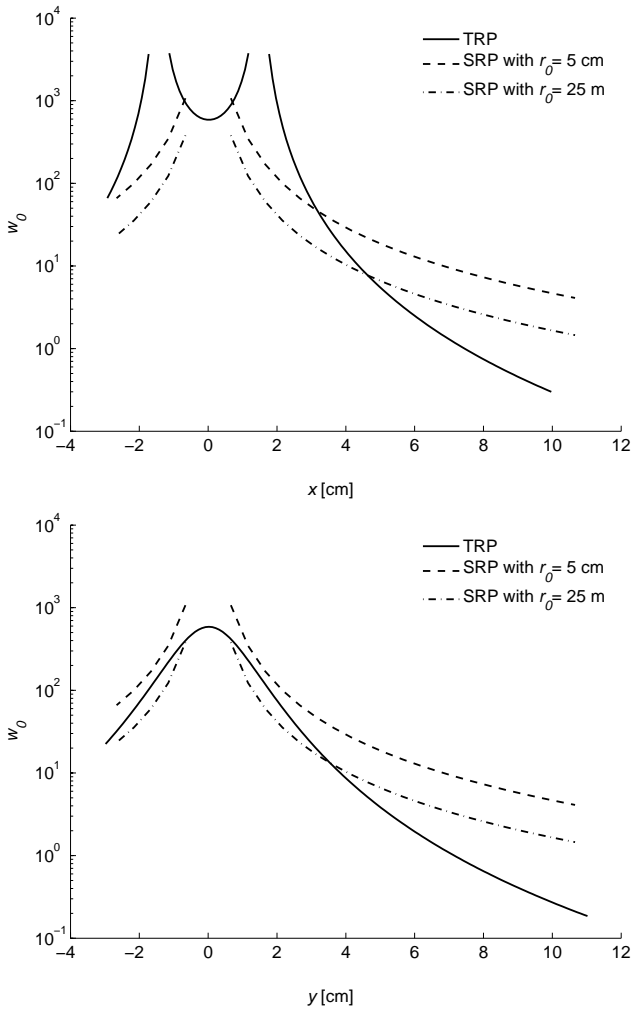


Figure 2.19: Weighting functions in x- and y-axis direction (according to Fig. 2.3) for a TRP with $d = 5$ mm, and $D = 30$ mm compared to the weighting functions of two SRPs with $d = 10$ mm and different r_0 .

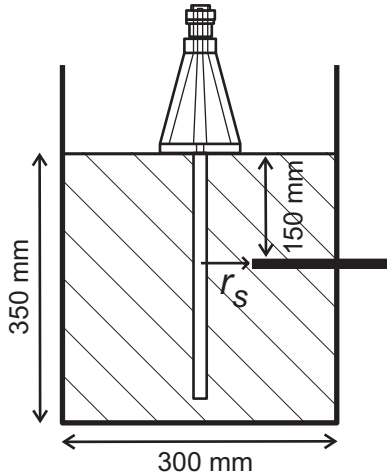


Figure 2.20: Setup for the first sensitivity experiment. The single-rod probe was mounted in a tank with dry sand (particle size 0.08 mm to 0.2 mm). A steel stick with diameter 10 mm was inserted laterally towards the probe. The reflection coefficient of the peak in the time-domain signal due to this scatterer as a function of the radial distance r_s was measured.

2.4.2 Sensitivity of the probes to scattering objects

Two experiments were carried out to compare the behavior of four different SRPs in the presence of conductive scattering objects in the sampling volume. Conductors correspond to a material with an infinite dielectric constant. A wave impinging on a metallic surface is completely reflected. A water-filled cavity with the same shape as the scattering objects used would cause a smaller reflection coefficient. A third experiment focussed on the effect of scattering objects with low dielectric constant (a “stone”) in water-saturated gravel (“wet soil”).

Four different probes were used:

- a coated rod and an uncoated aluminum stick according to Figure 2.17, combined with
- the small/the large horn (Fig. 2.13)
- a TRP with $d = 5$ mm, $D = 31$ mm, $L_{TRP} = 300$ mm.

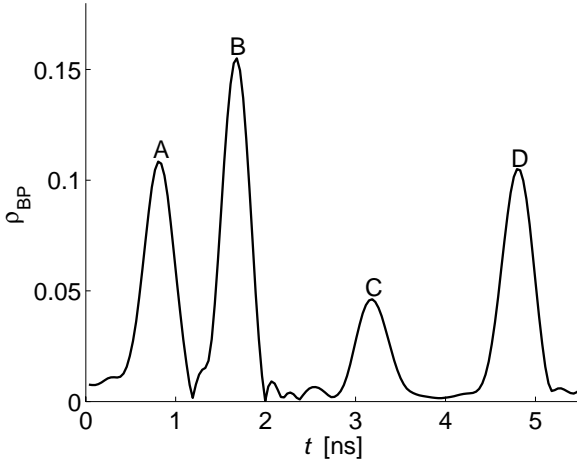


Figure 2.21: Sample trace (bandpass response) from the sensitivity experiment with the perpendicular stick. Clearly discernible are (A) the reflection from the transition coaxial-cable to horn, (B) the reflection from the end of the horn, (C) the reflection from the scatterer and (D) the reflection from the end of the probe.

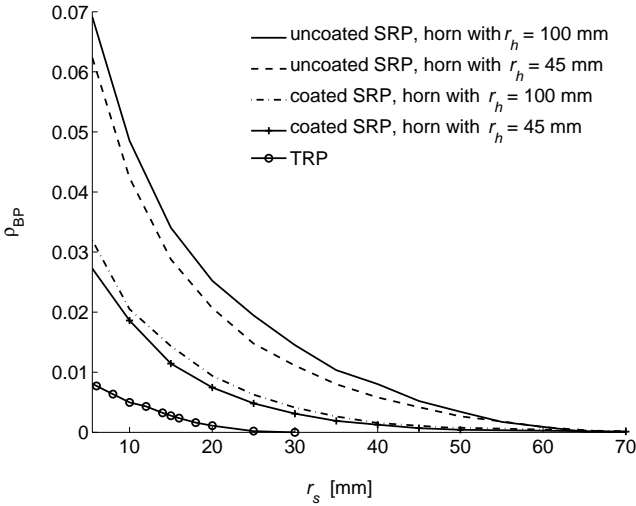


Figure 2.22: Sensitivity experiment with the perpendicular stick. Reflection coefficient ρ_{BP} due to the scatterer vs. the distance r_s .

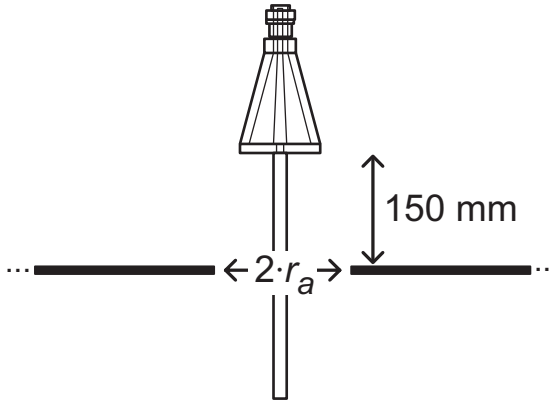


Figure 2.23: Setup for the aperture experiment. A 1 mm thick quadratic aluminum sheet of 1 m^2 area has an opening of variable radius $r_a = 15 \dots 80 \text{ mm}$ in its center. The SRP is positioned in the center of the opening.

Lateral stick as a scatterer

In this experiment, the SRPs were mounted in a tank filled with dry quartz sand (Fig. 2.20). As a scatterer, a steel stick with a diameter of 10 mm was inserted perpendicular to the probe axis and moved stepwise towards the rod. In the case of the two-rod probe the stick was moved towards the center axis.

Using a HP 8753 vector network analyzer the frequency response as a function of radial distance r_s between the steel stick and the probe was measured for the frequency 30 MHz to 5 GHz. With the built-in inverse Fourier transform function the measurement was converted into a time-domain signal (bandpass response). This procedure allowed to obtain a higher signal to noise ratio than using a commercial TDR measurement device with band-limited step response. According to Figure 2.21, the peak due to the scatterer can be identified in the trace and the corresponding bandpass reflection coefficient ρ_{BP} was determined.

Figure 2.22 shows that in all four cases the influence of the scatterer on the time-domain trace is not measurable for $r_s > 70 \text{ mm}$. The SRPs with the coated rod show about half the reflection coefficient of probes with the uncoated rod. The different mode converters have an insignificant influence on the measured reflection coefficient. The two-rod probe compared with the SRPs shows a reflected amplitude which is significantly smaller.

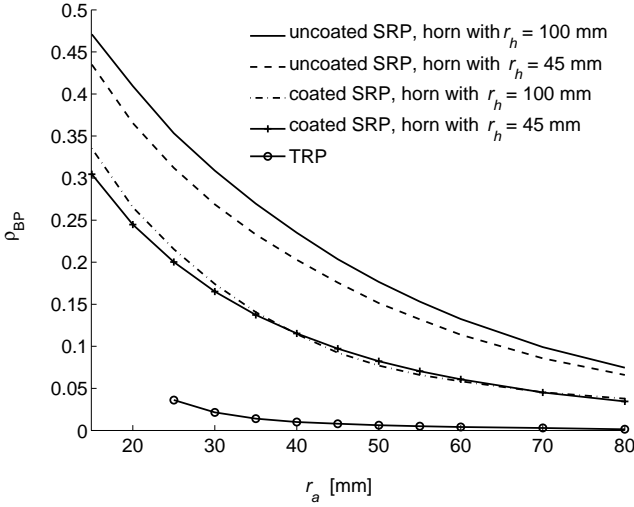


Figure 2.24: Reflection coefficient ρ_{BP} of aperture scatterer vs. radius r_a .

Aperture as a scatterer

A large scatterer was used in this second experiment: a quadratic aluminum sheet with an area of 1 m^2 and a circular aperture of radius 80 mm in the center, according to Figure 2.23. The size of the opening was reduced by using rings, which were consecutively attached to the aluminum sheet until the aperture radius r_a was 15 mm. The probe was mounted to pass through the center of the opening. The band-pass time domain function of the HP 8753 network analyzer was used, from 30 MHz to 5 GHz. The experiment was performed with the four SRPs and with the dual rod probe. Again, the peak due to the scatterer was identified in the trace and the corresponding bandpass reflection coefficient ρ_{BP} was read out.

Figure 2.24 shows that for all four SRPs the influence of the large scatterer is still visible at $r_a = 80$ mm. There is no difference regarding the measured reflection amplitude between the coated SRP with the small horn and the coated SRP with the large horn. For the uncoated SRPs with different horns only a small difference was observed. The two-rod probe compared with the SRPs again shows a significantly smaller reflection coefficient.

Cavities with low dielectric constant

For the third experiment, a tank was filled with gravel and saturated with deionized water to simulate a very wet soil, where the effect of “dry” stones in the measurement range of an TDR probe would be largest (Fig. 2.25). Gravel, because of its

large particle size, can be saturated fast without the danger of entrapping air. This was advantageous for this experiment, where three closed-pore polystyrene cubes of side lengths $s = 50$ mm, 100 mm and 140 mm respectively, had to be buried and reburied several times at several centimeters below the gravel surface. Polystyrene cubes were selected as stone substitutes because of their well-defined shape. With a dielectric constant of $\kappa' = 2.6$ polystyrene is below the dielectric constants of stones, which are in the range of $\kappa' = 4 \dots 8$. The outcome of the experiments marks therefore an upper boundary in the sense, that the effect of a real stone instead of the substitute would be minor for any common stone material.

A polystyrene cube was placed at different distances r_p in direction of the y-axis from a TDR probe mounted vertically in the tank (Fig. 2.25). For each distance the full TDR trace was recorded with a TDR100 reflectometer. Due to the high-pass characteristic of the small horn (Fig. 2.15), frequency components of the step signal below 200 MHz are not transmitted. TDR curves obtained with an SRP therefore look different compared with usual two-rod probe curves. Nevertheless it is still possible to use the algorithm by Baker and Allmaras (1990) and Heimovaara and Bouten (1990) to determine the travel time of the signal. Figure 2.26 illustrates this approach. Tangents are fitted both to the probe-head leading edge and the end reflection edge. They are intersected with tangents fitted to a short range before these reflections. From the intersections the two-way travel time of the signal is obtained, which includes the travel time through the head section (in this case the horn).

All traces were processed with this algorithm which provides the apparent dielectric constant κ'_{eff} . From the latter a volumetric water content θ was calculated with the relation of Topp et al. (1980). The experiment was repeated with all three polystyrene cube sizes and two TDR probes: a TRP with $d = 5$ mm, $D = 31$ mm and $L_{\text{TRP}} = 300$ mm and an uncoated SRP with $d = 10$ mm, $\sigma_c = 16.2$ MS/m, $L_{\text{SRP}} = 300$ mm with the small horn ($R = 45$ mm).

Figure 2.27 shows, that the influence of a “stone” in the proximity of the probe is larger for an uncoated SRP than for an TRP of comparable size.

2.4.3 Conclusions regarding the sensitivity investigations

Two different kinds of sensitivity comparisons have been conducted. First, SRPs and TRPs were compared regarding their radial sensitivity in the case of a quasi-homogeneous medium. Second, SRPs and TRPs were compared regarding the radial sensitivity to different scattering objects.

Both comparisons show, that an uncoated SRP has a larger influence range compared to a TRP of equal size. For the case of a single, small scattering object, e.g. a stone or a water cavity, the influence range of an SRP is around 6 cm and twice the size of the influence range of a TRP. For a quasi-homogeneous medium, the averaging in the sampling volume is more balanced in the case of an SRP and the weighting function decays slower. The SRP is therefore more suitable for

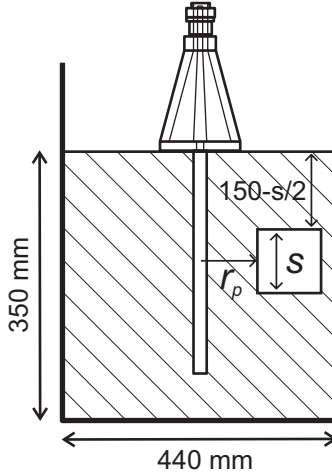


Figure 2.25: Setup for the third sensitivity experiment. A polystyrene cube was placed in water-saturated gravel (particle size 2 mm to 3 mm, volumetric water content $\theta = 0.427 \text{ m}^3 \text{ m}^{-3}$) at several distances from a vertically installed TDR probe. The experiment was repeated with three cubes of different size and with TRP and a SRP probes.

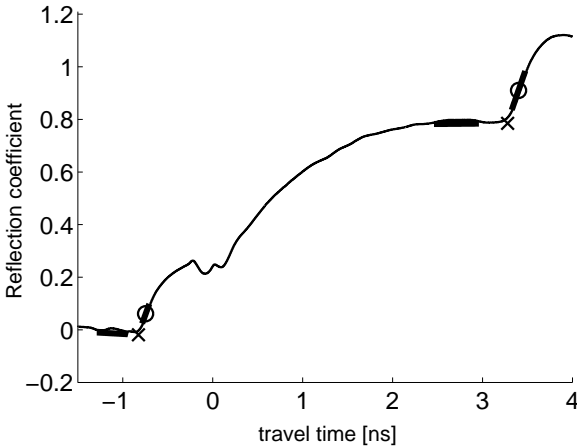


Figure 2.26: Evaluation of a TDR trace obtained with an SRP (example). The algorithm is explained in the text.

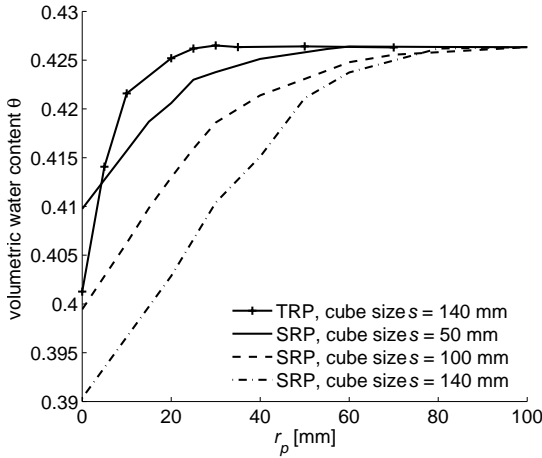


Figure 2.27: Apparent volumetric water content θ vs. distance r_p .

non-local measurements of water content with TDR.

2.5 Calibration

The calibration of the TDR probes consists in determining the relationship between the volumetric water content θ of a medium, varied from zero to full saturation, and the apparent dielectric constant κ'_{eff} , obtained from the analysis of the TDR traces. Ideally, the calibration is performed with a soil-sample from the fieldsite, where the probes are intended to be installed. However, this can become a very laborious and time consuming task, especially if the probes are used in different soil types. A common short-cut is to calibrate the probes only in air and immersed in water, and to assume the empiric $\theta - \kappa'_{\text{eff}}$ relationship of Topp et al. (1980). An intermediate solution would use a soil substitute for calibration.

The knowledge of the exact volumetric water content in the measurement range of the probe is crucial for an accurate calibration. For this task, the availability of a medium with a time independent, homogeneous water content would be beneficial. Though the latter seems to be achieved easily, a closer look reveals significant difficulties for water content levels between the residual water content and full saturation. In the unsaturated range above residual water content, any mixture of water and particles is susceptible to drainage, rendering a vertically inhomogeneous water content distribution. Several ways to circumvent this problem and to obtain an optimal calibration medium were studied.

2.5.1 Very fine grain material

Very fine grained materials, e.g. clays, can exhibit high residual water contents up to $\theta_r = 0.4$ because of small pore sizes. Unfortunately, the latter corresponds to a medium with a large specific surface. A substantial part of the water is more or less bound to the particle surface, with reduced ability to polarize in an oscillating electromagnetic field. Clays or equivalent fine grain materials with high water content are therefore very lossy with a significant influence of the losses on the speed of a propagating electromagnetic wave. Finally, TDR traces obtained from such a medium lack of a pronounced end reflection which makes an accurate travel-time analysis impossible.

2.5.2 Coarse grain material

Instead of using a fine grain material at residual water content as a calibration medium, a water saturated coarse grain material with low porosity could be utilized. Low porosity can be achieved with a large grain size distribution. However, such mixtures tend to separate when agitated, leading to inhomogeneity. Smaller sized grains accumulate at the bottom, because they fall easier through narrow gaps.

Alternatively, coarse grains of well defined shape and size can arrange themselves to a dense packing with low porosity. Approximately cube shaped gravel of 2 to 3 mm sidelength was experimentally found to have a porosity of $\phi = 0.42$. Spheres, however, have an ideal volume filling rate of 0.74 independent of the sphere radius. No source for coarse grains with other regular shapes like tetrahedrons, octahedrons or dodecahedrons could be found.

2.5.3 Solid particles

Different manufacturers offer low-loss dielectric materials with $\kappa' = 80$, which could be used to mimic the dielectric behaviour of water up to ≈ 15 GHz, where the relaxation of water is not yet noticeable. The homogeneity of a mixture of sand and small ceramic chunks could be judged by eye, because of the different colors of the materials. The mixture appears to be electrically homogeneous, if the sizes of the ceramic particles are well below the smallest wavelength of the TDR signal in the medium. For a common soil at full saturation $\kappa'_s \approx 25$ and with a TDR reflectometer bandwidth of 1.5 GHz (e.g. TDR100, Tektronix 1502) the smallest signal wavelength relevant is around

$$\lambda_{\min} = \frac{c_0}{f_{\max} \sqrt{\kappa'_s}} = 4 \text{ cm} \quad (2.19)$$

The particle size should be 4 mm or less. Though such particles are available, they are far too expensive for the purpose intended, e.g. 50 cm² (0.05 liters) cost about \$2000.

2.5.4 Liquids

To use a liquid as the soil substitute for calibration has the advantage, that the medium has not to be remixed before each calibration. The calibration with liquids consists in relating the apparent dielectric constant measured with TDR to the true dielectric constant, obtained with a reference measurement method. Alcohols, in principle, would be the most interesting liquids for calibration. They are able to form hydrogen bonds in much the same way as water but exhibit lower dielectric constants (Table 2.2). The dispersion of the dielectric constant, like for the case of water, is well described with a Debye type relaxation spectrum. Unfortunately however, the relaxation frequencies increase with chain length and fall into the measurement bandwidth of the TDR device for the longer molecules with lower dielectric constants. In such a case, there is no clear reference value available for κ' (Robinson et al. (2003) for an example of this problem with a mixture of propanol and water). After all, monomolecular fluids would only permit calibration at some discrete dielectric constant values.

Mixtures of two alcohols or of an alcohol with water exhibit a single relaxation time at an frequency position which reflects the molar ratios of the two components. For a mixture with a low dielectric constant, the relaxation frequency would be near the component with a low κ' and fall into the measurement bandwidth of the TDR device.

A mixture with $\kappa' = 3...25$ depending on the ratio of the volumetric parts of the components would be favorable. This would at least require a very low dielectric, apolar component and a clearly polar molecule. Two such substances in general do not mix well. In such a case two distinct relaxation times are observed and they do not differ greatly from those of the pure solvents. This suggests that the molecules do not experience average environments, but form aggregates which are microassemblies of like molecules. Therefore, the relaxation times resemble those of the pure solvents and the relaxation volumes are significantly larger than the molecular volumes, indicating that the relaxation processes are occurring within an aggregate of molecules (Gabriel et al., 1998). With different mixture ratios of acetone and n-hexane, Sen et al. (1992) could vary the dielectric constant of the composition in the range $\kappa' = 2...20$ at 1.25 GHz. Pure acetone has a high relaxation frequency of 46.8 GHz and n-hexane has a low $\tan\delta < 0.01$ at 1.25 GHz. The mixture therefore might exhibit constant dielectric properties up to the GHz range, independent of the volumetric ratio of the components.

However, even if a suitable calibration liquid would be found, the process suffers from the disadvantage of missing $\theta - \kappa'_{\text{eff}}$ data points. The probe might be calibrated with liquids to measure the correct dielectric constant of a medium. But the relationship between the dielectric constant and the water content for a certain bulk medium still is left to be determined.

Alcohol	κ'_0	f_{rel} [GHz]
Methanol	32.8	3.09
Ethanol	24.6	0.94
Propan-1-ol	19.5	0.48
Pentan-1-ol	15.8	0.20

Table 2.2: Debye parameters for some alcohols (Gabriel et al., 1998)

2.5.5 Gelating agents

Drainage can be slowed down or even prevented by increasing the viscosity of the fluid, e.g. with gelling agents. For water, thickeners are known in cooking as e.g. corn starch, gelatine or agar. In the usual TDR frequency range from 0.2 to 3 GHz, none of these gelling agent preserve the complex dielectric constant of free water exactly. For agar gels however the change is small (Roebuck and Goldblith, 1975). Additionally, agar gels exhibit densities close to the density of free water. This was the motivation to investigate agar-gel sand mixtures.

Materials, methods and results

Agar is obtained from the cell walls of red algae or seaweeds (mainly *sphaerococcus euchema*, *gelidium* and *gracilaria*). It consists to 90% of heteropolysaccharides (thereof are 70% agarose, which is the gelling agent and 30% non-gelling agaropektin), to 7% of sulfate and to 3% of pyruvate. Agarose is a linear polysaccharide made up of the basic unit agarobiose, which comprises alternating units of galactose and 3,6-anhydrogalactose.

Prior to the experiments with agar-gels and sand, the complex dielectric constant κ was measured in the frequency range from 0.2 to 3 GHz of a completely hydrated gel with gelling agent agar (Sigma-Aldrich Product Number 05038) and of a second completely hydrated gel with gelling agent agarose (Sigma-Aldrich Product Number 05056). The two gels were obtained by heating a mixture of 0.015 mass parts of the gelling agent (agar, respectively agarose) with 0.985 mass parts of deionized water up to 100° C. The pots with the boiling fluids were removed from the hot plates to cool down to room temperature, which resulted in rigid gels. The complex permittivity κ of the gels and of deionized water at room temperature were measured with the Agilent 85070 dielectric probe kit and an HP 8753ES network analyzer in the frequency range from 0.2 to 3 GHz. According to Figure 2.28, the real part of the dielectric constant, κ' , of the agar-gel and of the agarose-gel were found to be similar, but slightly lower than the values measured for deionized water. The difference is in the order of $\Delta\kappa' \approx 7$ over the whole frequency range. The agar-gel and the agarose-gel exhibit a slightly higher loss than deionized water above 1 GHz.

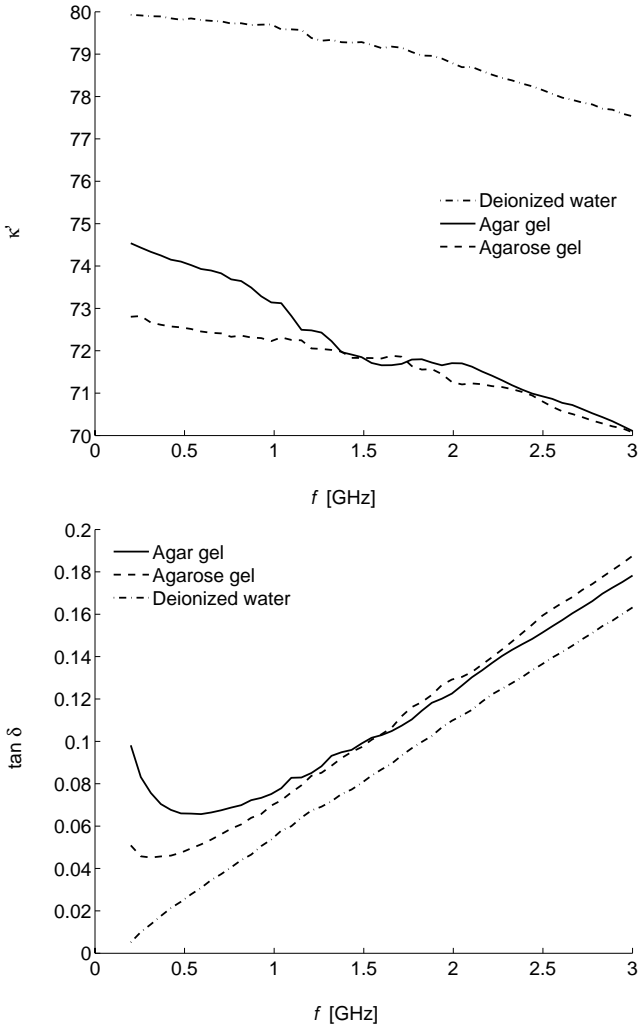


Figure 2.28: Dielectric constant κ' and $\tan \delta$ vs. frequency f of the agar gel, the agarose gel and deionized water. The gels contain 0.985 mass parts of deionized water and 0.015 mass parts of agar (Sigma-Aldrich Product Number 05038) or agarose (Sigma-Aldrich Product Number 05056).

Table 2.3: Agar-gel sand mixtures: results of TDR measurements. The volumetric water content θ was determined by drying out a sample of the mixture at 105° C for 24 h and by scaling the result according to the density of the columns. The real, relative, effective permittivity κ'_{eff} was measured with a TDR dual-rod probe system.

weight parts		density [kg/m ³]	θ [m ³ m ⁻³]	κ'_{eff}
sand	agar			
15	1	1302.6	0.07	4.4
15	2	1354.4	0.15	7.8
15	3	1420.9	0.22	12.6
15	4	1462.2	0.30	16.2
15	5	1479.8	0.36	21.1

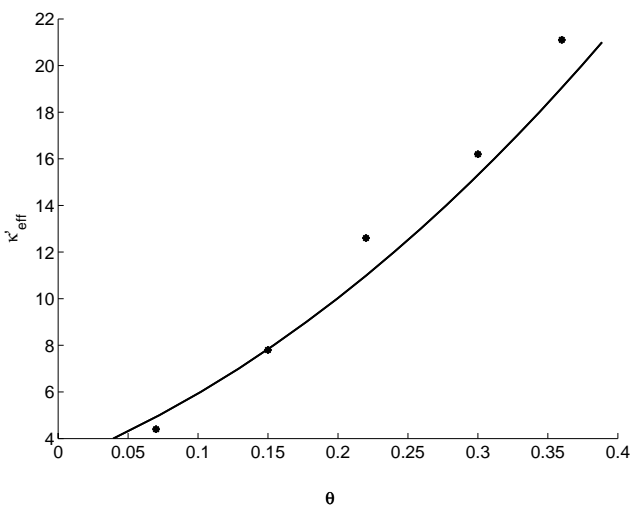


Figure 2.29: Measured dielectric constants of five different agar-gel sand mixtures (dots) as a function of water content, and the calibration curve by Roth et al. (1990).

The agar gel, which had a density of 980 kg m^{-3} , was further processed. It was crushed to particle size of 3 mm with a food mill. These gel particles were then mixed by hand with sand of grain size 0.08-0.2 mm in the mass ratios 1:15, 2:15, 3:15, 4:15 and 5:15. The mixtures were filled into cylindric containers with a diameter of 200 mm. The final filling height was 300 mm. The weight and the volume of the agar-gel-sand columns were determined and the densities of the mixtures calculated. Before filling the columns, 150 g of each mixture was taken and dried at 105°C for 24 hours. This process is applicable, because above 85°C all agar-water linkages are broken. The resulting gravimetric water content was converted to volumetric water content by use of the calculated densities.

A two-rod TDR probe with a probe length of 300 mm, rod spacing 30 mm, rod thickness of 5 mm, was vertically inserted from the top into the column. It was assumed that the water content along the rod varies only slightly. The TDR trace was measured using a Tektronix 1502B TDR scope and evaluated with the algorithm by Baker and Allmaras (1990) and Heimovaara and Bouten (1990). The measured dielectric constants are listed in Table 2.3 and plotted in Figure 2.29 together with the values predicted by the model of Roth et al. (1990):

$$\kappa' = \left((1 - \phi)\kappa_s'^a + \theta \kappa_w'^a + (\phi - \theta)\kappa_a'^a \right)^{1/a} \quad (2.20)$$

with the dielectric constant of the soil matrix $\kappa_s' = 4.5$, the dielectric constant of the agar-gel $\kappa_w' = 73$, the dielectric constant of soil air $\kappa_a' = 1$, the porosity $\phi = 0.35$ and the fitting factor $a = 0.46$.

The homogeneity of an agar-gel sand mixture in time was investigated with another column with a diameter of 200 mm. The tank was filled up to a height of 400 mm with a 3:15 gel-sand mixture. Immediately afterwards, the column was equipped with eight three-rod probes of rod length 12 cm, horizontally inserted and at different levels (Fig. 2.30). The TDR traces were recorded every 3 min over a period of 250 min with a Tektronix 1502B sampling scope and a CR10X Campbell datalogger. The traces were evaluated by the algorithm of Baker and Allmaras (1990) and Heimovaara and Bouten (1990). Figure 2.31 shows the time scale and extent of the drainage in the gel-sand mixture. After 250 min the initial volumetric water content of the column of $\theta = 0.22$ had changed as much as $\Delta\theta = +0.04$ for the probe no. 1 at the lowest level and $\Delta\theta = -0.02$ for probe no. 8 at the top level. Drainage was not completed at the end of the experiment.

As an alternative mixing concept, the sand part was poured directly into the boiling agar-water fluid and stirred until a homogeneous mixture was obtained. The blend was removed from the heat and was kept agitating. At the gelling point at around 35°C this became an increasingly difficult and finally impossible task. Cooled down at room temperature, the mixture became a very inhomogeneous and brittle solid. TDR probes could only be inserted with force, breaking the consolidated brick.

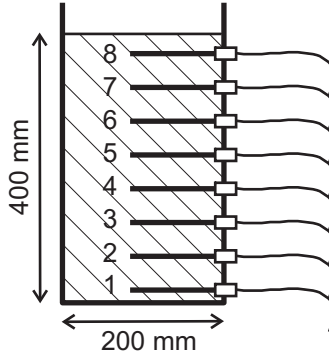


Figure 2.30: Setup for the homogeneity experiment. Eight three-rod probes were inserted horizontally at different levels into a column with an agar-gel sand mixture (mass ratio 3:15).

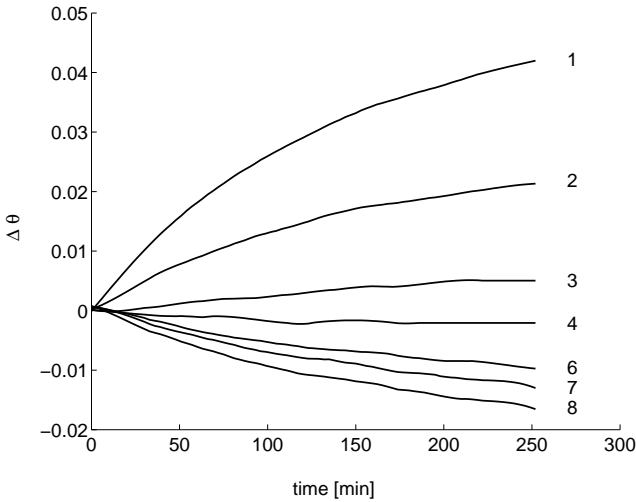


Figure 2.31: Relative volumetric water content $\Delta\theta$ as a function of time. Plotted is the difference of the volumetric water content θ compared to the initial state ($\theta = 0.22$) at the different levels (probe no. 5 failed).

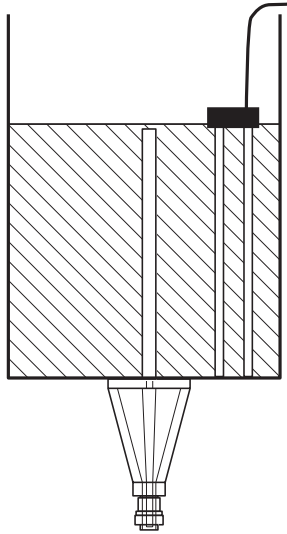


Figure 2.32: Setup for the calibration in the wet range of soils. The single-rod probe was mounted from below in a cylindrical tank with radius 120 mm, then the pass-through in the bottom was sealed. A temporarily mounted two-rod probe was used for reference measurements.

Discussion and conclusion

According to Figure 2.29, mixtures of agar-gel with sand follow the calibration curve of Roth et al. (1990) well. This is not surprising, as the dielectric properties in the frequency range 0.2 to 3 GHz and the densities of agar gels were found to be similar to those of free water. The difference of the real part of the permittivity is $\kappa'_{\text{agar gel}}/\kappa'_{\text{water}} \approx 0.9$. The water content of the agar-gel sand mixtures have to be determined by gravimetry for best accuracy at higher water contents. The influence of the increased losses of agar-gels on wave velocity is completely negligible. The velocity is reduced to 99.98% of its loss-less value with losses as high as $\tan \delta = 0.1$ (cf. section wave velocity). Agar-gels are therefore suitable dielectric substitutes for free water in soil-water mixtures in the frequency range from 0.2 to 3 GHz. The measured drainage effect in the agar-gel sand column is attributed to the appearance of free water, which was released by the agar gel during the mixing process and due to the pressure in the non-consolidated packing. Agar gels are susceptible to mechanical stress; pressure and friction easily extricate bound water.

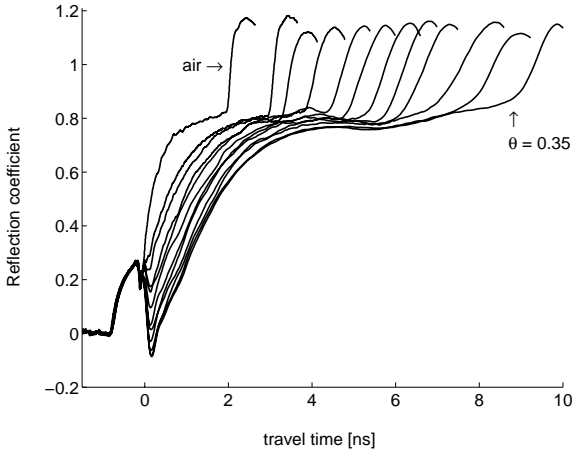


Figure 2.33: Calibration traces, truncated to the significant part for better display. From left to right: air, 0.0, 0.02, 0.05, 0.07, 0.09, 0.12, 0.15, 0.18, 0.24, 0.28, 0.35 volumetric water content. The traces are different from those of usual two-rod probe curves because low-frequency components of the TDR step signal are not transmitted by the single-rod probe.

2.5.6 Calibration with a vertically inhomogeneous medium

Due to the failure of the approaches explained above, the SRP was finally calibrated with an inhomogeneous medium and a special calibration setup. An uncoated SRP with the small horn was mounted bottom-top in a tank with 120 mm radius and 400 mm height (Fig.2.32). The moist sand with 0.08 to 0.2 mm particle size was filled into the tank up to a few centimeters higher than the probe end. Drainage was still apparent but no water could escape. It was assumed that the SRP and the two-rod probe measure the length-weighted average water content if refractive index averaging is dominant (Schaap et al., 2003). A high bandwidth TDR device and an appropriate evaluation algorithm, which mainly tracks the higher frequency part of the signal, support this assumption. The Tektronix 11802 scope with an SD 24 TDR sampling head used for the measurements has a rise time of $t_r = 35$ ps corresponding to a theoretical bandwidth of $0.35/t_r = 10$ GHz (Strickland, 1970). The effective bandwidth is slightly lower because of cable losses. Preliminary measurements in water and air allowed to determine the head-section offset for the SRP. The velocity of the signal was calculated from the two-way travel time. Therefrom, the dielectric constant κ'_s was derived via the relation $v = c_0/\sqrt{\kappa'_s}$. For each SRP measurement a reference curve with the two-rod probe was collected. The average volumetric water content was calculated for each case on the basis of the added sand and water. All calibration measurements were taken at room temperature with deionized water.

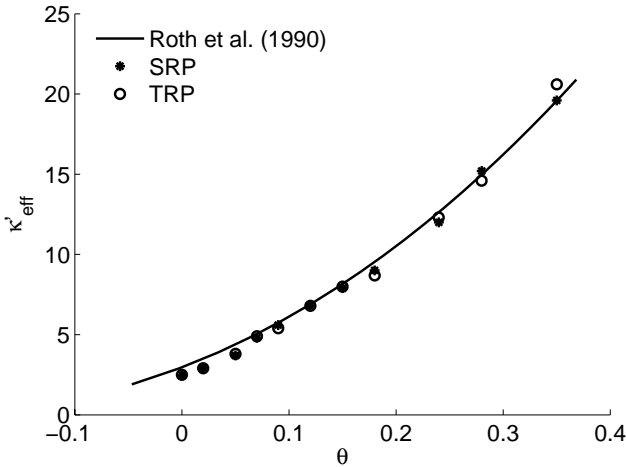


Figure 2.34: Calibration measurements of the relative dielectric constant κ'_{eff} vs. volumetric water content θ . The calibration curve by Roth et al. (1990) is plotted as a solid line.

Figure 2.34 shows, that the dielectric constants as measured with the SRP match the reference values well. The differences between the SRP and the two rod measurements increase with a higher water content, though no systematic deviation could be observed. The end reflection slope steepnesses of TDR curves of wet sand are smoother than those of dry sand, which reduces accuracy in determining the end reflection point. Figure 2.34 compares the measured permittivities with the values predicted by the model of Roth et al. (1990) with the dielectric constant of the soil matrix $\kappa'_s = 4.5$, the dielectric constant of water $\kappa'_w = 80.2$ at 20°C , the dielectric constant of soil air $\kappa'_a = 1$, the porosity $\phi = 0.35$ and the fitting factor $a = 0.46$. The calculated values and the measured data are in good agreement, which supports the assumption of refractive index averaging to be appropriate.

Chapter 3

Profile reconstruction algorithms

Profile reconstruction algorithms for TDR measurements attempt to reconstruct the water content profile along a probe from a recorded TDR curve. Direct inversion formulas are known, but their application range is limited, as explained in the introductory chapter. More sophisticated reconstruction algorithms comprise an electric soil model, a forward solver and an optimizing procedure. With the forward solver the expected TDR curve is simulated. The optimizing procedure compares the simulated and measured TDR curve and adjusts the parameters of the model in order to reduce the difference. This process is iterated until the match between the simulated and the measured curve is as good as requested. At this final point, the values of the model parameters are assumed to describe the electric soil properties correctly.

3.1 Electric soil model

Recent developments in advanced evaluation of TDR measurements have shown that a multisection model with Debye-type parameters for each layer is a promising approach (Feng and Lin, 1999; Weerts et al., 2001; Lin, 2003a). Such a model is shown in Figure 3.1. Each of the N layers has four parameters: the relaxation frequency $f_{\text{rel}}[n]$, the dielectric constant $\kappa'_0[n]$ at frequencies well below $f_{\text{rel}}[n]$, the dielectric constant $\kappa'_\infty[n]$ at frequencies well above $f_{\text{rel}}[n]$ and the conductivity $\sigma[n]$. This model is versatile, but has a very large variable space. An appropriate reconstruction algorithm is hard to develop. In a practical case, however, the soil structure is often roughly known. Here, the case of a non-reactive, homogeneous soil with a low specific surface area $A_s = 0 - 100 \text{ m}^2/\text{g}$ is assumed. This assumption is made to simplify the experiments performed to test the algorithm. As will be explained at the end of this chapter, the algorithm, developed below, is not restricted

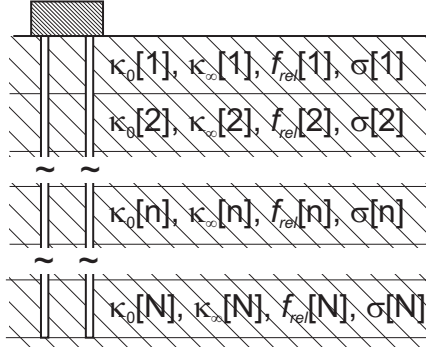


Figure 3.1: Multislice-Debye soil model: the soil is discretized in N horizontal layers with the Debye parameters $\kappa_0, \kappa_\infty, f_{rel}, \sigma$.

to this soil class.

Bound water effects are negligible for soils with a low specific surface area. The relaxation frequency of water in the pore space corresponds approximately to the relaxation frequency of free water, which is $f = 17$ GHz. Therefore, it is possible to set $f_{rel}[n] \forall n = f_{rel} = 17$ GHz. The relaxation frequency is well out of the measurement bandwidth of common TDR reflectometers, which is around 1.5 GHz. However, f_{rel} is still low enough to have a noticeable effect on the dielectric constant, especially on the dielectric losses, e.g. $\tan \delta \approx 0.2$ at 2 GHz.

For the specified soil class, the dielectric constant well above f_{rel} can be assumed to be $\kappa'_\infty[n] \approx 1 \forall n$.

Figure 3.2 illustrates the simplified electric soil model, which has two variables per layer, the Debye parameter $\kappa'_0[n]$ and the conductivity $\sigma[n]$.

3.1.1 Coupling of water content and conductivity

Local conductivity and local water content determine the shape of the measured TDR trace very similarly, as will be explained in detail later. This fundamental problem can only be solved through the establishment of a relationship between $\kappa'_0[n]$ and $\sigma[n]$. However, the relation between local conductivity and local water content can assume a broad variety of forms, depending on the soil type. In order to constitute such a relationship, restrictions on the soil type have to be made. The simplified model of the previous section is already confined on non-reactive soils with a low specific surface, where surface conductivity can be neglected and no ion exchange processes with the soil matric are apparent. The conductivity σ of the porous media is then mainly a function of the pore water conductivity σ_{el} . Under

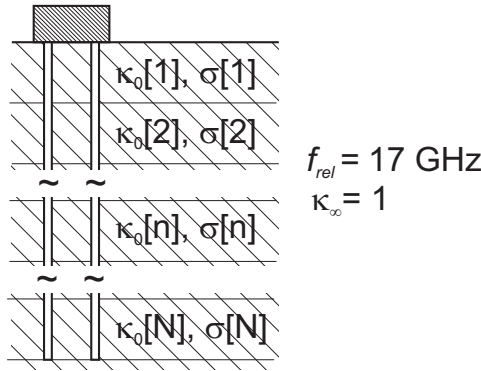


Figure 3.2: Simplified multislice-Debye model for soils with a low specific surface area, $A_s = 0 - 100 \text{ m}^2/\text{g}$, where $f_{rel} = 17 \text{ GHz}$ and $\kappa_\infty = 1$ for all layers.

these circumstances, the empiric rule termed “Archie’s law” (Archie, 1942) can be applied, which relates σ_{el} , the soil porosity ϕ , and the degree of saturation S to the conductivity σ of the porous medium with a, c and k as fitting coefficients:

$$\sigma = a\sigma_{el}S^c\phi^k \quad (3.1)$$

For soils of the mentioned class, $a \approx 1$, $k \approx 1.88$, $c \approx 4 \dots 5$ according to Santamarina et al. (2001) and Hunt (2004).

The degree of saturation S is defined as

$$S = \frac{\theta - \theta_r}{\theta_s - \theta_r} \quad (3.2)$$

with the water content at saturation, $\theta_s \approx \phi$, and the residual water content θ_r . For a small layer, which is an element of the soil matrix, θ_r and a, c and m are constants. Two saturation states S_1 and S_2 for this layer then relate to the corresponding water contents θ_1 and θ_2 as

$$\frac{S_2}{S_1} \approx \frac{\theta_2 - \theta_r}{\theta_1 - \theta_r} \quad (3.3)$$

The ratio of the conductivities σ_1 and σ_2 becomes

$$\frac{\sigma_2}{\sigma_1} \approx \left(\frac{\theta_2 - \theta_r}{\theta_1 - \theta_r} \right)^c \quad (3.4)$$

if the pore fluid conductivity σ_{el} remains approximately constant. It is clear, that the latter is a strong assumption.

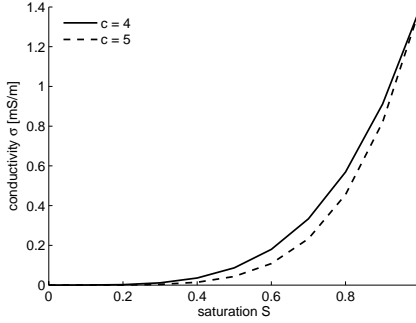


Figure 3.3: Conductivity σ vs. saturation S as described by Archie's law for $a = 1$, $\sigma_{el} = 0.01$ mS/m, $c = 4$ and $c = 5$, $\phi = 0.35$, $k = 1.88$.

3.2 Simulation of the TDR curve

The complex dielectric constant $\kappa[n]$ of each layer is given by the Debye equation with an additional conductivity term:

$$\kappa[n] = \kappa'_{\infty} + \frac{\kappa'_0[n] - \kappa'_{\infty}}{1 + j \frac{\omega}{\omega_{rel}}} - j \frac{\sigma[n]}{\epsilon_0 \omega} \quad (3.5)$$

with $\omega_{rel} = 2\pi f_{rel}$. The impedance Z and the propagation constant γ for an electromagnetic wave on the two-rod transmission line are

$$Z[n] = \sqrt{\frac{\mu_0}{\epsilon_0}} \frac{\pi}{\sqrt{\kappa[n]}} \operatorname{arcosh} \frac{D}{d} \quad (3.6)$$

according to Ramo et al. (1993), and

$$\gamma[n] = \frac{2\pi f}{c_0} \sqrt{-\kappa[n]} \quad (3.7)$$

The input impedance for each segment is

$$Z_{in}[n] = \frac{Z_{in}[n+1] + Z[n] \tanh \gamma[n] l}{1 + \frac{Z_{in}[n+1]}{Z[n]} \tanh \gamma[n] l} \quad (3.8)$$

The probe end is modeled with the impedance $Z[N+1] = Z_e$. Applying Eq. 3.8 iteratively, $Z_{in}[1]$ can be obtained.

The wave phase velocity $v[n]$ results from the imaginary part of γ in each layer:

$$v[n] = \frac{2\pi f}{\operatorname{Im} \gamma[n]} = \frac{\operatorname{Im} \sqrt{-\kappa[n]}}{c_0} \quad (3.9)$$

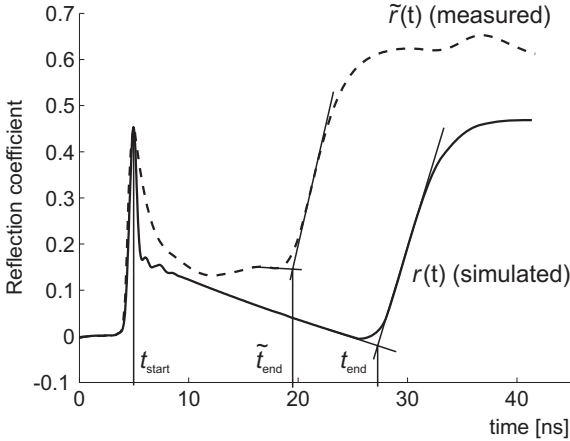


Figure 3.4: Measured example TDR trace $\tilde{r}(t)$ and simulated example TDR trace $r(t)$. Indicated are the time points t_{start} , \tilde{t}_{end} , t_{end} .

The cumulative travel time is defined as

$$T[n] = \sum_{n=1}^N \frac{l}{v[n]} \quad (3.10)$$

The simulated reflection coefficient in the frequency domain is

$$R(f) = \frac{Z_{in} - Z_w}{Z_{in} + Z_w} \quad (3.11)$$

with Z_w the wave impedance of the coaxial cable. Through inverse Fourier transform (IFT) the TDR curve can be obtained

$$r(t) = \text{IFT } R(f) \quad (3.12)$$

The simulated TDR trace is, if necessary, time-shifted to match the measured trace in the area of the probe start, as shown in Figure 3.4. The common start of the probe rods in the TDR traces is denoted by t_{start} . The ends of the probe rods in the TDR traces are denoted by \tilde{t}_{end} for the measured trace, t_{end} for the simulated trace. These end reflection points are determined with the algorithm by Baker and Allmaras (1990) and Heimovaara and Bouten (1990).

The volumetric water content $\theta[n]$ of the layer n can be obtained with a calibration function, e.g. the one by Topp et al. (1980):

$$\theta[n] = -5.3 \cdot 10^{-2} + 2.92 \cdot 10^{-2} \kappa'_0[n] - 5.5 \cdot 10^{-4} \kappa'_0{}^2[n] + 4.3 \cdot 10^{-6} \kappa'_0{}^3[n] \quad (3.13)$$

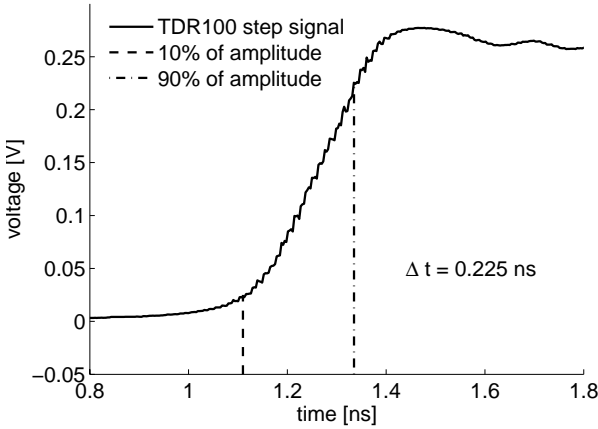


Figure 3.5: TDR100 step signal of the reflectometer used in the experiments, as recorded with the reflectometer itself. The signal rise time from 10% to 90% of the maximal signal amplitude of 0.25 V is approximately 225 ps.

3.3 Inclusion of limited signal rise-time

The simulation procedure developed so far relies on a reflectometer with zero step signal rise time. In reality, TDR measurement devices have a finite measurement bandwidth. For a TDR100 reflectometer, e.g., the specified maximum signal rise time is 300 ps. Step signal rise time is defined as the time for a signal to rise from 10% to 90% of the maximum signal amplitude. Figure 3.5 shows the step impulse of the TDR100 reflectometer used for the experiments described further below, it was found to have a signal rise time of 225 ps.

The ideal step signal from 0 to 1 with zero rise time shall be denoted with $s(t)$ and the real step signal with $s'(t)$. A frequency response $H(f)$ can then be defined as:

$$H(f) = \frac{\text{FT } s'(t)}{\text{FT } s(t)} \quad (3.14)$$

with FT the Fourier transform. $H(f)$ can then be used to filter the simulated reflection coefficient $R(f)$,

$$R'(f) = H(f) \cdot R(f) \quad (3.15)$$

which yields the filtered reflection coefficient $R'(f)$. From the latter, a TDR trace is obtained, which includes the effects of the limited reflectometer signal rise time. The signal $s'(t)$ can be acquired with the reflectometer itself: the initial signal step from 0 to the nominal voltage on the 50 Ω line is recorded. The ideal signal $s(t)$ can be generated artificially.

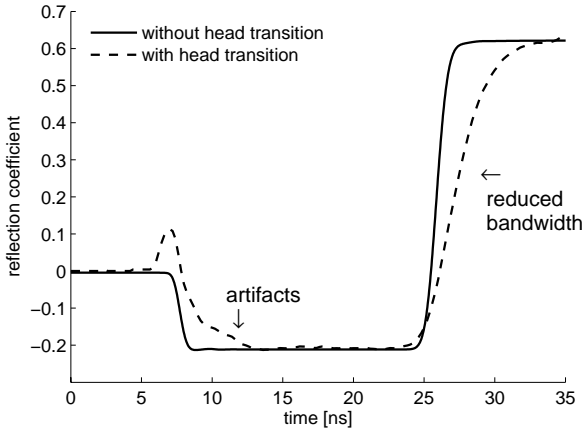


Figure 3.6: Sample TDR traces of deionized water, measured with a probe with distributed head transition and simulated for a probe without a head transition. The step signal of the simulated trace has a rise time of 225 ps. The distributed head transition has a significant influence on the trace shape.

3.4 Distributed probe head transition

The structure of the model developed so far assumes a direct transition from the coaxial cable with impedance Z_w to the two-rod transmission line with input impedance Z_{in} . In such an ideal case, the impedance would change abruptly from Z_w to Z_{in} at the connection point. Different conductor geometries of the coaxial and the two-rod transmission line as well as the change from an unbalanced to a balanced wave guide makes the transition more complex in reality. A non-ideal transition can become a source of problems:

- The bandwidth of the transition can be considerably lower than the signal bandwidth. Precision deteriorates.
- Multiple reflections due to the transition section can load the beginning of the measurement curve with artifacts. If the transition section is not properly modeled, the reconstruction algorithm may be misled by these artifacts.

The example of Figure 3.6 illustrates both these effects.

A simple model for a distributed transition comprises M elements with impedances $Z_h[m]$, propagation constants $\gamma_h[m]$ and lengths $s[m]$. This transition model is appended to the electric soil model, i.e. the impedance $Z_h[M+1]$ of the element beyond the last element of the head corresponds to the input impedance $Z_{in}[1]$ of the

rod section, $Z[M+1] = Z_{in}[1]$. By applying the impedance transformation formula iteratively,

$$Z_{h,in}[m] = \frac{Z_{h,in}[m+1] + Z_h[m] \tanh \gamma_h s[m]}{1 + \frac{Z_{h,in}[m+1]}{Z_h[m]} \tanh \gamma_h s[m]} \quad (3.16)$$

the probe equivalent input impedance $Z_{h,in}[1]$ results. From the latter, the reflection coefficient $R(f)$ is obtained with Eq. 3.11.

The definition of the head model values for a given TRP is, in principle, not a straight-forward task. The transmission scattering parameter s_{21} of the probe head section alone can not be measured directly, common network analyzers have only coaxial connectors. Indirect measurements would include other parts of the transmission line. However, it was found that in practice the head section can be modeled with a few elements, whose parameter values are adjusted manually to obtain a good fit between $r(t)$ and $\tilde{r}(t)$ in the head section of the traces.

3.5 Optimization

3.5.1 Error functions

The objective is to minimize the deviation between the measured TDR trace $\tilde{r}(t)$ and the simulated waveform $r(t)$ for $t = 0 \dots \infty$. However, it can be difficult to simulate the end reflection slope as it also depends on the complex electric field distribution in the medium beyond the probe rods. Therefore, the end reflection is simply modeled with an quasi infinite impedance, e.g. $Z_e = 100 \text{ M}\Omega$ and a restricted error function is established:

$$\eta = \int_{t=t_{\text{start}}}^{\max(\tilde{t}_{\text{end}}, t_{\text{end}})} (r(t) - \tilde{r}(t))^2 dt \quad (3.17)$$

This error function, as shown in Figure 3.7, measures the difference between the calculated and the measured trace from t_{start} up to the last end reflection time point of the two traces. The optimization goal is reached when $\eta < \eta_{\text{max}}$ with the user defined maximum allowed error η_{max} . In such a case, the layer variables $Z[n]$ and $\gamma[n]$ of the model are assumed to describe the effective electric properties of the layers.

A second error function ξ is defined as

$$\xi = \int_{t=t_{\text{start}}}^{\min(\tilde{t}_{\text{end}}, t_{\text{end}})} (r(t) - \tilde{r}(t))^2 dt$$

This error function measures the difference between the calculated and the measured trace from t_{start} up to the first end reflection time point of the two traces. The error limit ξ_{max} is defined as $\xi_{\text{max}} = \xi$ at $\eta = \eta_{\text{max}}$. Figures 3.7 and 3.8 illustrate the case $\eta > \eta_{\text{max}}$ and $\xi < \xi_{\text{max}}$, where the simulated TDR curve matches the measured

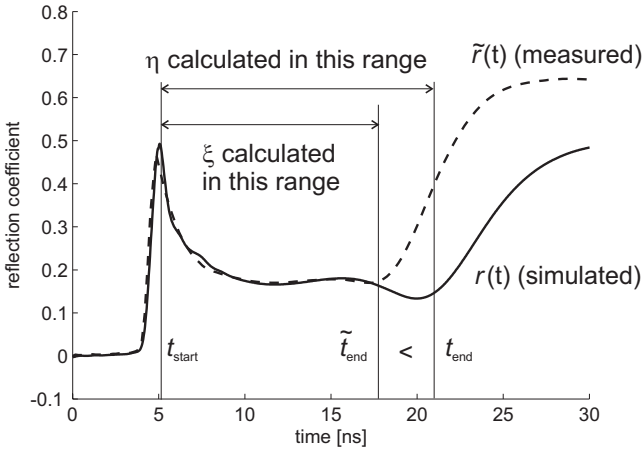


Figure 3.7: Sample measured and simulated TDR traces for the case $\eta > \eta_{\max}$ and $\xi < \xi_{\max}$, where $\tilde{t}_{\text{end}} < t_{\text{end}}$. Due to a too low value for the pore water conductivity σ_{el} , a part of the difference between $r(t)$ and $\tilde{r}(t)$ was attributed wrongly to a higher water content.

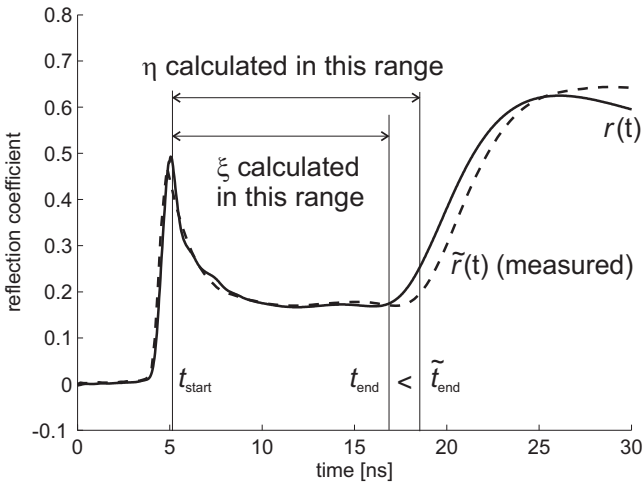


Figure 3.8: Sample measured and simulated TDR traces for the case $\eta > \eta_{\max}$ and $\xi < \xi_{\max}$, where $t_{\text{end}} < \tilde{t}_{\text{end}}$. Due to a too high value for the pore water conductivity σ_{el} , a part of the difference between $r(t)$ and $\tilde{r}(t)$ was attributed wrongly to a higher conductivity.

trace well, but only up to the first end reflection time point of the two traces. This case occurs, if the pore water conductivity value σ_{el} is not correct. Optimization is stopped, and has to be restarted with a adjusted σ_{el} value. If $t_{end} > \tilde{t}_{end}$, the overall water content of the profile model is too high. The source of this error is a too low value for σ_{el} . Contrary, if $t_{end} < \tilde{t}_{end}$, the overall water content of the profile mode is too low and the value for σ_{el} is too high.

3.5.2 Parameter adaptation

If η is small, $\tilde{r}(t)$ and $r(t)$ correspond approximately to the same locations for $\forall t$ and the difference function

$$\Delta r(t) = r(t) - \tilde{r}(t) \quad (3.18)$$

can be calculated. At times where $\Delta r(t) > 0$, the difference at the corresponding location z may be attributed to

- a higher true local water content $\tilde{\theta}(z) > \theta(z)$. This means a higher real part of κ'_0 (Eq. 3.13) and a true local impedance with lower magnitude $|\tilde{Z}(z)| < |Z(z)|$ (Eq. 3.6). The latter results in a lower measured reflection coefficient $\tilde{r}(t)$ which yields a positive difference $\Delta r(t) > 0$.
- a higher true local conductivity $\tilde{\sigma}(z) > \sigma(z)$. This means a higher imaginary part of κ'_0 and therefore a lower magnitude $|\tilde{Z}(z)| < |Z(z)|$ with the same effect as a higher local water content.
- a multiple reflection effect

Analogously, $\Delta r(t) < 0$ may be attributed to a lower true local water content or to a lower true local conductivity or to both.

In our model, multiple reflection effects are captured with the method of equivalent input impedance. The source of the change $\Delta r > 0$, however, cannot be determined without a relation between $\theta(z)$ and $\sigma(z)$. This explains, why a coupling between water content and conductivity had to be established.

The start point of the layer n corresponds to the time point $T[n-1] + t_{start}$ in the simulated TDR trace. If a difference $\Delta r(t) \neq 0$ is observed, the local dielectric constant $\kappa_0[n, i]$ of iteration step i is changed to the new dielectric constant $\kappa_0[n, i+1]$ as follows

$$\kappa'_0[n, i+1] = \kappa'_0[n, i] + w \cdot \Delta r(T[n-1] + t_{start}) \quad (3.19)$$

with the optimization weighting factor w . The new local water content $\theta[n, i+1]$ is calculated with Eq. 3.13. The new conductivity value $\sigma[n, i+1]$ becomes with Eq. 3.4

$$\sigma[n, i+1] = \sigma[n, k] \left(\frac{\kappa'_0[n, i+1]}{\kappa'_0[n, i]} \right)^c \quad (3.20)$$

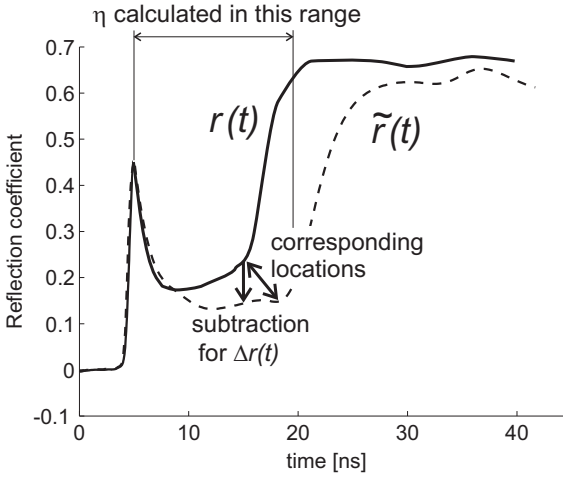


Figure 3.9: The difference function $\Delta r(t)$ is built by subtracting the measured TDR trace $\tilde{r}(t)$ from the simulated TDR trace $r(t)$ in the range of η (example).

For a large value of η , the difference $\Delta r(t)$ is meaningless, because reflection coefficients, which do not correspond to the same locations, are subtracted, as illustrated in Figure 3.9. Therefore, the modified difference function

$$\Delta r_b = r(b(t - t_{start}) + t_{start}) - \tilde{r}(t) \quad (3.21)$$

is defined with the scale factor

$$b = \frac{\tilde{t}_{end} - t_{start}}{t_{end} - t_{start}} \quad (3.22)$$

With this modification, the simulated reflection curve $r(t)$ is scaled, so that the end points of the scaled curve $r_b(t)$ and of $\tilde{r}(t)$ coincide. Scaling of $r(t)$ prevents large errors in Δr if the simulated and the measured trace are very different in length. However, reflection coefficient values, which do not correspond to the same locations, might still be subtracted, this aspect is accounted for with a filtering of the difference function, as explained below.

The update equation 3.19 is

$$\kappa'_0[n, i + 1] = \kappa'_0[n, i] + w \cdot \Delta r_b(T[n - 1] + t_{start}) \quad (3.23)$$

with the modified difference function.

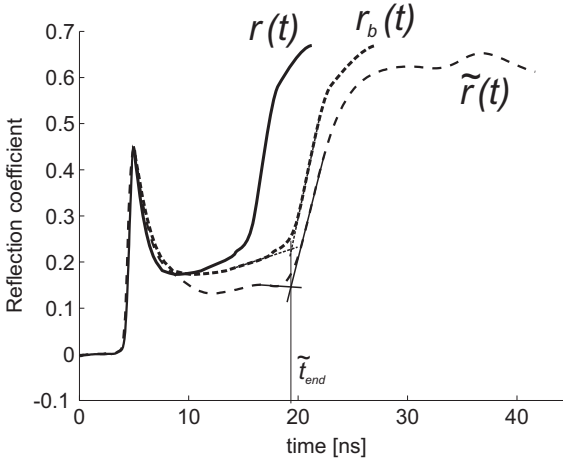


Figure 3.10: Sample measured TDR trace $\tilde{r}(t)$, a sample simulated TDR trace $r(t)$ and the shifted simulated TDR trace $r_b(t)$ with the same t_{end} as \tilde{t}_{end} .

3.5.3 Filtering of the difference function

In the optimizing process, Eq. 3.23 is applied iteratively for all layers. First trials with this parameter adaptation procedure exhibited self-amplifying artifacts in the simulated TDR trace. These artifacts resulted from $\Delta r_b(t)$, where $r(t)$ and $\tilde{r}(t)$ did not correspond to the same locations. To suppress this effect, a Savitzky-Golay filter SG is issued, with order o and frame size p (Savitzky and Golay, 1964). The filter is applied on the difference function to obtain a filtered difference function:

$$\Delta r_{SG} = SG(\Delta r_b) \quad (3.24)$$

The Savitzky-Golay filter method performs a local fit with order o in a frame of p data points to determine the smoothed value for each data point. Applying SG on Δr_b means that a local error is distributed to adjacent layers. This results in an optimization process which corrects global errors first before correcting local errors, while the ability to correct local errors is preserved.

3.6 Initialization of the layer variables

An estimate of the mean water content $\bar{\theta}$ can be obtained with the conventional TDR evaluation procedure where

$$\bar{\kappa} = \left(\frac{c_0(\tilde{t}_{end} - t_{start})}{2L} \right)^2 \quad (3.25)$$

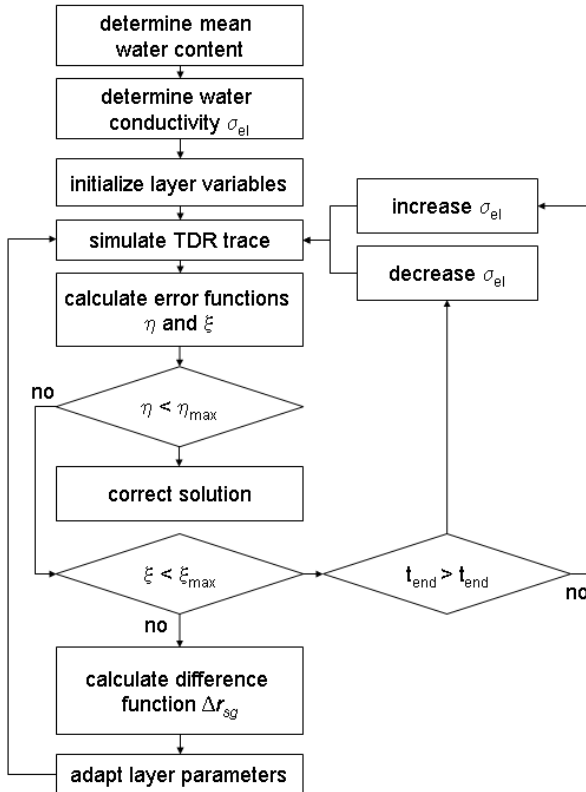


Figure 3.11: Flow chart of the reconstruction algorithm.

A reasonable initialization consists in assuming a homogeneous wet soil with the same water content $\bar{\theta}$ for all layers $\theta[n] = \bar{\theta} \forall n$, i.e., $\kappa'_0[n] = \bar{\kappa}'_0$. According to our model, the conductivity of all layers is then the same, i.e. $\sigma[n] = \bar{\sigma}$ with the mean conductivity $\bar{\sigma}$. The mean conductivity can be estimated with the method of Giese and Tiemann (1975) and Heimovaara and de Water (1993) where

$$\bar{\sigma} = \frac{1}{Z_0 g(D, d)} \cdot \frac{1 - r(\infty)}{1 + r(\infty)} \quad (3.26)$$

with the geometric factor

$$g(D, d) \approx \frac{12.1 L}{\ln\left(\frac{D}{d} + \sqrt{\left(\frac{D}{d}\right)^2 - 1}\right)} \quad (3.27)$$

and

$$Z_0 = \sqrt{\frac{\mu_0 \pi}{\epsilon_0}} \operatorname{arcosh} \frac{D}{d} \quad (3.28)$$

Inverting Archie's law, Eq. 3.1, the electrolyte conductivity is obtained:

$$\sigma_{\text{el}} = \frac{\bar{\sigma}}{a} S^{-c} \phi^{-k} \quad (3.29)$$

Figure 3.11 summarizes the algorithm in a flow-chart.

3.7 Laboratory experiment

A laboratory experiment was performed, where a long TRP was mounted vertically in a acrylic glass tank filled with dry quartz sand of grain size 0.02-0.8 mm. The TRP was attached to a coaxial cable, whose inner conductor and sheat were split up for connection just as far as necessary. The parameters of the experiment are listed in Table 3.1. Figure 3.12 illustrates the setup and shows the eight installed reference TRPs. The reference TRPs were mounted horizontally, protruding through the acrylic wall into the tank at the levels below surface as indicated in the Figure. The column was slowly wetted through a porous bottom plate with deionized, deoxygenated water until the water table reached the surface of the column. Subsequently, the column was drained by gravity with the end of the outlet hose 400 mm below the bottom of the tank. After each additional liter of outflow, measurements were made of all probes with a TDR100 scope and a CR10X datalogger. A total of 15 different drainage states was measured. The TDR traces of the horizontal probes were evaluated with the algorithm by Baker and Allmaras (1990) and Heimovaara and Bouten (1990) to obtain the mean water content at the different levels, which allowed to sketch water content profiles. The measurements with the vertical probe were processed with the reconstruction algorithm, with the parameters listed in Table 3.1. The head transition effects, except for the artifacts, could be modeled with

tank	vertical probe	reference probes	model	algorithm
$W = 440$ mm	$d = 14$ mm	$d = 5$ mm	$N = 40$	$w = 10$
$w = 5$ mm	$D = 114$ mm	$D = 31$ mm	$M = 1$	$o = 3$
$h = 1000$ mm	$L = 960$ mm	$L = 145$ mm	$Z_h[1] = 1500 \Omega$ $s[1] = 20$ mm	$p = 361$ 2500 data points

Table 3.1: Parameters for the laboratory experiment and the corresponding profile reconstructions.

a single element of length $s = 20$ mm with a very high impedance $Z = 1500 \Omega$. This is clearly an artificial model, as the probe head is an electrically distributed system.

Except for the top 10 cm, the reconstruction for the water content profile was approximately correct for all 15 measured drainage states. Figure 3.13 shows some of the reconstructions together with the sketched water content profiles. The failure of the reconstruction in the top layers can be attributed to the artifacts and the bandwidth limitation introduced with the probe head.

The estimated pore water conductivity resulted to be $\sigma_{el} = 0.5 \pm 0.2$ mS/m, which corresponds to the measured value $\tilde{\sigma}_{el} = 0.6$ mS/m of the deionized water used in the experiment.

3.8 Field experiment

In order to obtain a real-world data set, an experiment at one of the institute's field sites was performed. The experiment site at Sellenbüren is densely covered with spruce. The topsoil consist of a 5 cm thick humic layer. Below and down to a depth of more than 70 cm, a primarily sandy soil follows. Six TDR probes were buried horizontally at the levels below surface indicated in Figure 3.14. Table 3.2 lists the parameters of the experiment. A long TDR probe was driven vertically into the soil, at a horizontal distance of 100 mm from the vertical transect formed by the tips of the horizontally installed TDR probes. The vertical TRP was attached to a coaxial cable, whose inner conductor and sheat were split up for connection just as far as necessary. All probes were connected to the TDR100 reflectometer and full traces for all probes were measured at noon daily and recorded with a CR10X data logger.

The measurement period spanned 67 days, started at the 6th of September 2004 and ended at the 11th of November 2004. At the beginning of the measurement period, the soil was homogeneously dry because of a long period without rainfall before the start of the experiment. Several heavy rainfall events during the experimental period then led to a variety of naturally generated profiles.

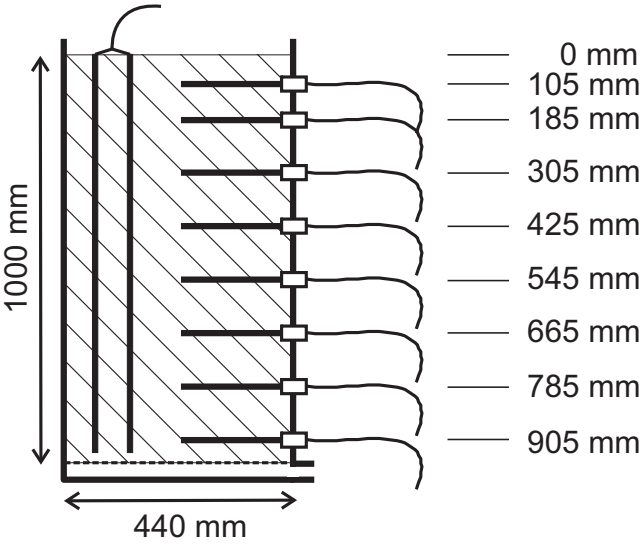


Figure 3.12: Initial setup for the laboratory experiment. Acrylic glass tank with wall thickness 5 mm filled with dry quartz sand with grain size 0.02-0.8 mm. The column was equipped with eight horizontal TRPs at the indicated levels below surface and a long, vertical TRP.

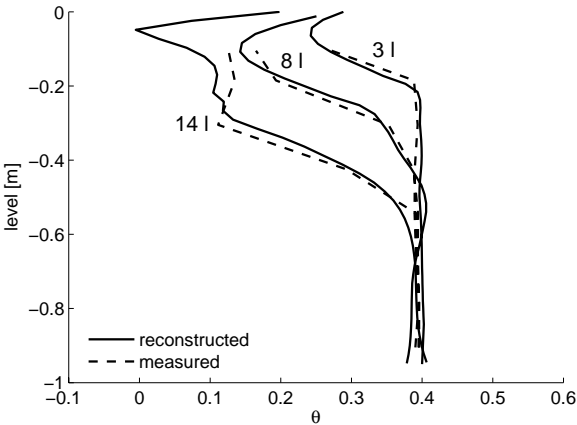


Figure 3.13: Measured and reconstructed water content profiles of the laboratory experiment after 3 liter, 8 liter and 14 liter of drained water.

soil	vertical probe	reference probes	model	algorithm
5 cm humic sand	$d = 14 \text{ mm}$	$d = 5 \text{ mm}$	$N = 40$	$w = 10$
	$D = 120 \text{ mm}$ $L = 700 \text{ mm}$	$D = 30 \text{ mm}$ $L = 18 \text{ mm}$	$M = 1$ $Z_h[1] = 1500 \Omega$ $s[1] = 20 \text{ mm}$	$o = 3$ $p = 661$ 2500 data points

Table 3.2: Parameters for the field experiment and the corresponding profile reconstructions.

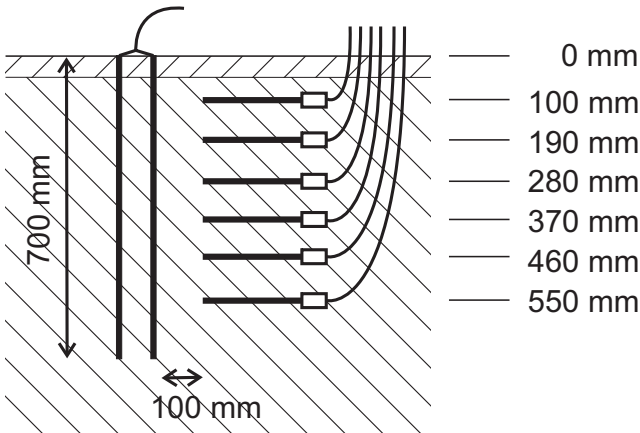


Figure 3.14: Setup of the field site experiment.

The traces from the vertical TDR probe were processed with the algorithm. The obtained water content profiles $\theta(z)$ were compared to the water content profile measured with the horizontal reference probes. While the quantitative match was poor, the reconstructed profiles follow the general trend of the measured profile. With the assumption of $\theta_r = 0.1$, $\phi = 0.4$ and $c = 4$, the algorithm yielded variable pore water conductivity in the range $\sigma_{el} = 12 \dots 20 \text{ mS/m}$. These are reasonable values. Fellow researchers at a field site nearby have been measuring the conductivity of the rain water over the past two years (personal communication, David Rais, WSL Birmensdorf). According to them, rain water conductivity had a mean value of 19.8 mS/m with a standard deviation of 8.3 mS/m . The difference between the measured and the reconstructed profile is attributed to the too strong assumption of constant pore water conductivity.

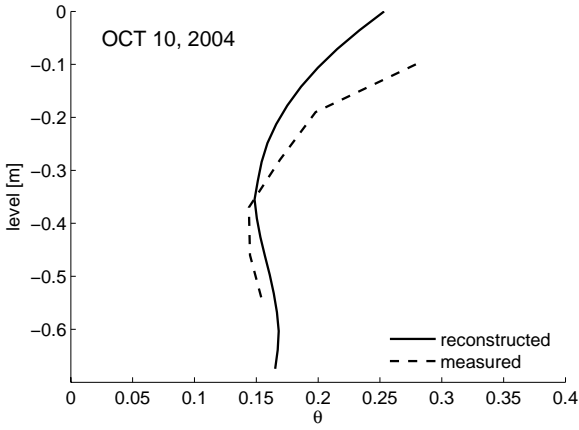


Figure 3.15: Example reconstruction of a field site measured profile, from October 10, 2004.

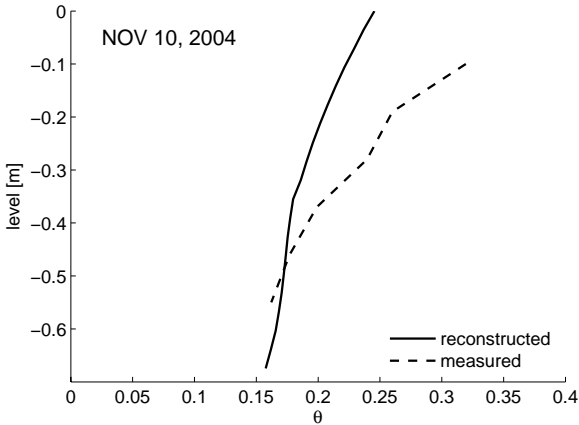


Figure 3.16: Example reconstruction of a field site measured profile, from November 10, 2004.

3.9 Discussion and conclusion

To the author's knowledge, this is the first time, a profile reconstruction algorithm is presented for a multislice-Debye soil model. The algorithm has been developed for the case of a non-reactive soil with a low specific surface area. This focus was set with the container experiment in mind. The idea was to demonstrate the feasibility of this new approach. If modified, the algorithm is not restricted on the mentioned soil class. More sophisticated calibration functions than Archie's law are known, which take into account surface conduction and ion exchange processes (e.g. the models of Bussian (1983), Mualem and Friedman (1991), or Revil et al. (1998)). The soil layer discretization can be adjusted to coincide with natural layers. The relaxation frequency may be expressed as a function of the local water content. Therefore, more complex soils can be handled by the algorithm. The prerequisite is a more detailed knowledge about the physics of the soil under test.

A debatable weakness of this approach is the assumption of constant pore water conductivity. This assumption is a consequence of the fact, that a TDR measurement is only a snapshot of a current soil state. A single TDR measurement does not inform about the history of the transport processes which happened in the measured soil. The knowledge of the latter is, however, mandatory for a more sophisticated assumption regarding the pore water conductivity. This leads to the conclusion, that future reconstruction algorithms should utilize time series of TDR measurements rather than a single snapshot, and that they should be coupled to a solute transport model.

It has been shown, that progress in TDR soil water content profile reconstruction can be achieved, if a reasonable link between local water content and local conductivity can be established. It is clear, that the presented algorithm is just an approach. However, the work is considered to point to the most promising direction for the further development of soil water content profile reconstruction from TDR measurements, where the empiric knowledge about pore water conductivity is essential.

Chapter 4

Coplanar strips for TDR measurements

Laboratory studies of transport processes in soils or in soil-like materials are often performed with some kind of container, which holds the investigated medium. In many cases, these columns are sorbed with water, drained, or set under a constant water flow. The local water content has to be monitored or is an important result variable. For this purpose, horizontally mounted TRPs protruding from the container wall into the column are commonly used. The accuracy of the estimated average water content measured with a probe increases with rod length. However, short probes are preferred, because they interfere less with the container medium. Very short probes could in principle be used, if the water content in the container is approximately constant in a horizontal plane. On the other hand, the accuracy of the evaluation algorithm suffers, if the probes are shorter than 100 mm (Robinson et al., 2003).

As an alternative, TDR probes made of two parallel coplanar metal strips (CPS) attached horizontally to the inside container wall were studied. Figure 4.1 shows a cross-section of this CPS probe in the vertical plane. TRPs are sensitive to the water content in their proximity only. Clearly, wall-mounted CPS as TDR probes are only a valid alternative to protruding TRPs if the water content in the horizontal plane of the probe is approximately constant.

4.1 Theory

The electromagnetic field of a TDR probe which consists of a CPS attached to a container wall differs significantly from a protruding TRP. A dispersionless TEM mode on a multiconductor transmission line structure is only possible, if the dielectric is homogeneous in the direction transverse to the wave propagation. This is

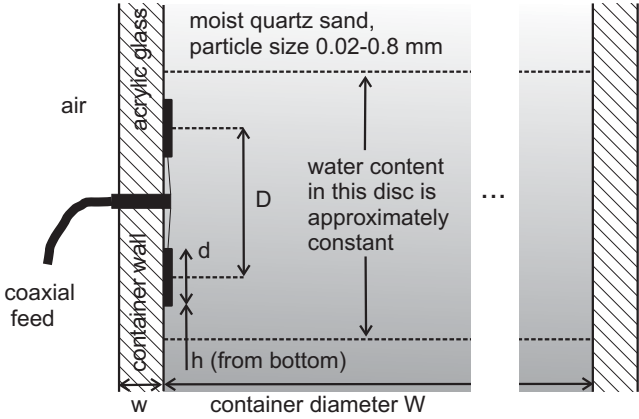


Figure 4.1: Cross section through a container with a mounted CPS with conductor widths d , center-center distance D , height h , container wall thickness w , container diameter W . Not indicated is the conductor thickness w_c of the CPS.

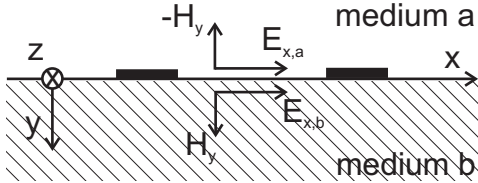


Figure 4.2: CPS on an interface of two media. The boundary conditions state, that the tangential electric field vector is constant across the interface. The magnetic field vector normal to the interface is continuous, if the permeabilities of the two media are equal.

often the case for a protruding TRP, because the vertical water content gradient in the TRP radial sensitivity range is normally small. A CPS attached to a container wall is quite a different case: there are three media with different dielectric constants which influence the electromagnetic field distribution. The CPS is on one side exposed to the container filling with dielectric constant κ'_s and on the other side attached to the container wall with dielectric constant κ'_c , whereafter air with $\kappa' = 1$ follows.

A simple example shows the difference between a transverse homogeneous and an transverse inhomogeneous medium. Figure 4.2 depicts a CPS probe on the interface of two media a and b with different dielectric constants κ'_a and κ'_b . The permeabilities is assumed to be $\mu_a = \mu_b = \mu_0$. The electromagnetic boundary equations state that the component of the electrical field tangential to the interface is continuous

$$E_{x,a} = E_{x,b} \quad (4.1)$$

With Maxwell's equations this can be expressed as

$$\kappa'_b(\nabla \times H)_{x,a} = \kappa'_a(\nabla \times H)_{x,b} \quad (4.2)$$

If the former equation is expanded, and with the continuity of the normal component of the magnetic field in the case of equal permeability

$$\mu_a H_{y,a} = \mu_b H_{y,b} \quad (4.3)$$

the following equation is obtained

$$\kappa'_a \frac{\partial H_{z,b}}{\partial y} - \kappa'_b \frac{\partial H_{z,a}}{\partial y} = (\kappa'_a - \kappa'_b) \frac{\partial H_y}{\partial z} \quad (4.4)$$

From $H_y \neq 0$ follows, that Eq. 4.4 should be non-zero on its left hand side, which can only be the case, if H_z is non-zero. An analogous procedure yields $E_z \neq 0$. The resulting propagation mode is therefore not a pure TEM mode, but a hybrid mode with electric and magnetic field components in propagation direction. Such a mode has a different wave velocity than a TEM mode and could in principle exhibit considerable dispersion.

CPS in a dielectric inhomogeneous environment have been well investigated (Gupta et al. (1979) for a review). The simplest analysis assumes that the field components in propagation direction can be neglected. The resulting mode is quasi-TEM. This allows to follow the quasi-static approach, where the transmission line parameters of a TEM are obtained by solving the electrostatic problem in the transverse plane. According to Zinke and Brunswig (2000), the quasi-static approach is valid for frequencies

$$f < \frac{c_0}{40\sqrt{\kappa'_s}(d+D)} \quad (4.5)$$

For CPS in air environment on a substrate with infinite thickness and κ'_s , the quasi-static approach yields an effective dielectric constant (Ramo et al., 1993)

$$\kappa'_{\text{eff}} = \frac{\kappa'_s + 1}{2} \quad (4.6)$$

from which the propagation velocity of the wave follows with

$$v = c_0 / \sqrt{\kappa'_{\text{eff}}} \quad (4.7)$$

CPS probes mounted on a container wall are similar to this case. The substrate is formed by the container filling and has a quasi-infinite thickness. In contrast, there are two additional dielectrics, the container wall with its thickness w and its dielectric constant κ'_c and the surrounding air. This can best be analyzed numerically with a 2-D field solver. From the capacitance C' for a unit length of the CPS, the effective dielectric constant can then be calculated with

$$\kappa'_{\text{eff}} = \frac{C'}{C'_s} \kappa'_s \quad (4.8)$$

where C'_s is the capacitance also obtained with a numerical analysis of the same CPS fully embedded in the medium with κ'_s .

4.2 Simulations

CPS probes intended to be used in an experiment were analyzed with the ANSOFT MAXWELL SV program, a 2-D field solver available from www.ansoft.com. The parameters of the CPS and of the container they are attached to, are listed in Table 4.1. The dielectric constant of the simulated container filling was varied in the range $\kappa'_s = 3..30$. Figure 4.3 plots the calculated effective dielectric constant κ'_{eff} versus the dielectric constant κ'_s of the medium. The results show an approximately linear dependence.

4.3 Experiments

An experiment with the parameters listed in Table 4.1 was performed, to investigate the behavior of CPS in a example case. Four CPS were mounted at different levels in a large container. They were attached to 50 Ω coaxial cables which were fed through bore holes and split up right at the start of the strips (Fig. 4.1). The container was made of acrylic glass with a dielectric constant of $\kappa'_c = 3.4$. Four reference TRP probes were mounted horizontally, protruding through the container wall into the container at the levels $h_{\text{ref}} = h + d/2 + D/2$, i.e. at the height of the middle line between the CPS. The values of h_{ref} are listed in Table 4.1.

Table 4.1: Parameters of the experiment with CPS mounted as TDR probes on a container wall.

container	height	h_c	960 mm
	wall thickness	w	5 mm
	inner diameter	W	440 mm
	wall dielectric const.	κ'_c	3.4
CPS probes	strip width	d	6 mm
	strip thickness	w_c	0.1 mm
	strip separation	D	19 mm
	strip length	L	295 mm
TRPs	installation height	h	535, 655, 775, 855 mm
	rod diameter	d	5 mm
	rod separation	D	30 mm
	rod length	L	145 mm
	installation height	h_{ref}	547.5, 667.5, 787.5, 867.5 mm

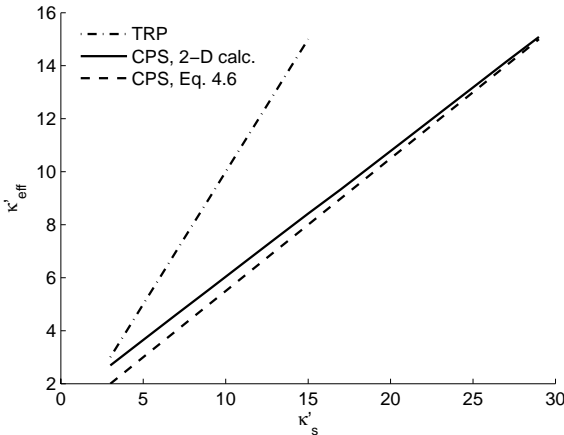


Figure 4.3: Effective dielectric constant κ'_{eff} for the CPS probes of the experiment vs. dielectric constant of the container filling κ'_s , once according to Eq. 4.6, once simulated with the 2-D field solver ANSOFT MAXWELL SV. For the TRP $\kappa'_{eff} \approx \kappa'_s$.

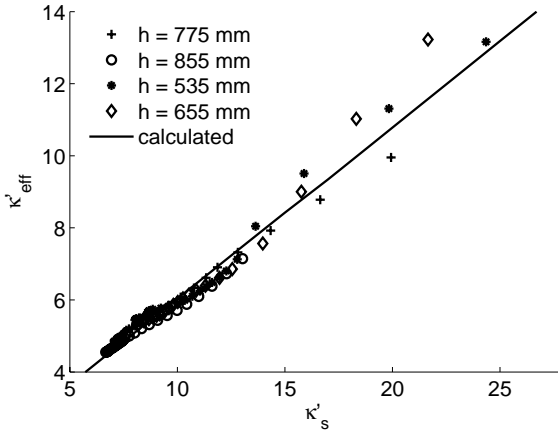


Figure 4.4: Measured effective dielectric constant κ'_{eff} for the CPS of the experiment vs. κ'_s measured with the reference TRPs. The straight line is the expected relationship based on 2-D field calculations.

The container was filled with dry quartz sand of particle size 0.08 to 0.2 mm. The sand was fully saturated from the bottom with deionized, deoxygenated water. Subsequently, the column was drained by gravity. The outlet of the drainage hose was 400 mm below the column bottom.

Full TDR traces of all probes were acquired with a TDR100 reflectometer and recorded with a CR10X datalogger. Measurements were taken after each additional liter of drained water. All TDR traces were analyzed using the algorithm by Baker and Allmaras (1990) and Heimovaara and Bouten (1990). The end-reflection rise time of the CPS traces did not differ from the end-reflection rise time of the traces from the conventional probes, which indicates negligible distortion in the case of the CPS. In Figure 4.4, the resulting effective dielectric constant κ'_{eff} of the CPS are plotted versus the dielectric constant κ'_s measured with the corresponding conventional TDR probe.

Figure 4.5 shows an example for the energy density distribution around the CPS of the experiment with a container medium $\kappa'_s = 10$ obtained with the MAXWELL SV simulation program.

4.4 Discussion and conclusion

For the CPS of the experiment, the quasi-static approach should only hold for frequencies up to 95 MHz at $\kappa'_s = 10$ according to Eq. 4.5. The results of the experi-

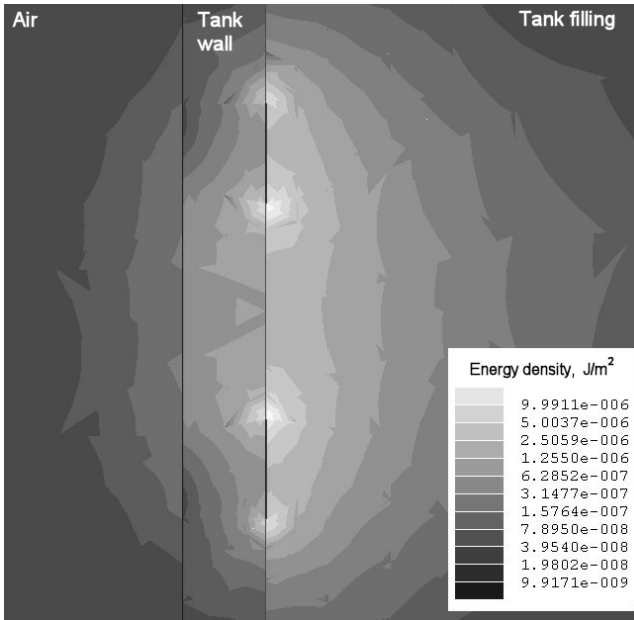


Figure 4.5: Energy density around a CPS of the experiment in the vertical cross-section plane. The dielectric constant of the medium is $\kappa'_s = 10$, the voltage across the conductors is 2 volts. Most of the energy is located in the container medium.

ment, however, show, that the measured κ_{eff} values match the calculated ones well in the range $\kappa'_s = 6 \dots 12$, although the bandwidth of the TDR signal is around 1.5 GHz. Variance increases for the measured values of the CPS with higher dielectric constant of the medium. These deviations may be attributed to the limits of the calculating approach. A part of the differences may also be caused by inhomogenities in the medium and by limited measurement accuracy. Nevertheless, the outcome suggest that CPS as wall-mounted TDR probes can be a valuable alternative to protruding TRPs for laboratory column experiments. Further designs should, however, use a lower value for D in order to secure, that the frequency limit of the quasi-static approach is high enough.

Chapter 5

Outlook

In the opinion of the author, future research in the field of TDR soil moisture measurement methods should focus on the following:

- The design and manufacture of a cost-effective single-rod probe for field use, with a small horn converter and a detachable, uncoated rod.
- Field studies, which compare and verify the measurements of a single-rod probe in a broader range of media, with soil samples taken in the proximity of the installed probe.
- The design and manufacture of a two-rod probe with minimized effects of the distributed head transition, the primary intended use of which would be for profile reconstruction.
- Adaptation of the reconstruction algorithm to different soil types with natural layers; field experiments aimed at testing the method and involving taking samples of the soil and the pore water to determine porosity, amount and conductivity.
- Container experiments with CPS probes and soil columns.

List of Figures

- 1.1 Soil water characteristics for the three sand types specified in Table 1.1. 4
- 1.2 Cole-Cole plots of the real, relative permittivity κ' versus the imaginary, relative permittivity κ'' for free water according to the Debye (D), the Cole-Cole (C-C) and the Davidson-Cole (D-C) model of relaxation. 10
- 1.3 A typical soil moisture TDR trace. 24
- 1.4 Energy density distribution of a two-rod probe in the cross-section plane. 26
- 1.5 Illustration of the differential reflection coefficient on a nonhomogeneous transmission line. 28

- 2.1 Cartesian coordinate system used in this chapter. 36
- 2.2 Geometric variables in the plane perpendicular to the SRP rod. . . 36
- 2.3 Geometric variables in the plane perpendicular to the TRP rods. . . 36
- 2.4 Wave velocity v vs. dependent on the dielectric constant κ'_s of medium with $\tan\delta_s = 0.001$ and with $\tan\delta_s = 0.1$ at the frequencies $f = 0.3, 1$ and 3 GHz for different SRP probes and a TRP as defined in Table 2.1. 39
- 2.5 Attenuation α_{dB} , including skin effect and dielectric losses vs. loss tangent $\tan\delta_s$ of the medium at the frequencies $f = 0.3, 1$ and 3 GHz for different SRP probes and a TRP as defined in Table 2.1. . 40
- 2.6 Attenuation $\alpha_{d,dB}$ of the dielectrics (coating and medium) and resistive (skin-effect) attenuation $\alpha_{c,dB}$ at 3 GHz vs. loss tangent $\tan\delta_s$ of the medium for the SRP with $d = 5$ mm, $\sigma_c = 1.5$ MS/m, $w_d = 0.5$ mm, $\kappa'_d = 100$, $\tan\delta_d = 0$ 40
- 2.7 Attenuation $\alpha_{d,dB}$ of the coating at 3 GHz vs. loss tangent $\tan\delta_s$ of the coating for an SRP with $d = 5$ mm, $\sigma_c = 60$ MS/m, $w_d = 0.5$ mm, $\kappa'_d = 100$ 41
- 2.8 Magnitudes of the electric fields E_r and E_z , normalized to $E_r|_{r=r_c}$ and the magnitude of the magnetic field H_ϕ , normalized to $H_\phi|_{r=r_c}$. 43

2.9 Magnitudes of the power densities S_z and S_T , normalized to $S_z|_{r=r_c}$. 43

2.10 Characteristic radius r_0 as a function of f for $\kappa'_s = 3$ and 25. 44

2.11 Characteristic radius r_0 as a function of the ratio w_d/r_c 45

2.12 Contour plot of the magnitude of the electric field in radial direction away from the metallic surface of a 50 mm long section of an SRP with $d = 5$ mm, $\sigma_c = 60$ MS/m, $w_d = 0.5$ mm, $\kappa'_d = 100$, $\tan \delta_d = 0.001$, at a frequency of 3 GHz in a loss-less medium with $\kappa'_s = 3$. 45

2.13 Linearly tapered horns as mode converters. 47

2.14 Sketched transition from the coaxial mode to the SRP mode. 48

2.15 Reflection and transmission coefficients of a 1 m long copper alloy rod of diameter 10 mm which is (A) attached at both ends to the large horns with $r_h = 100$ mm, (B) attached to the small horns with $r_h = 45$ mm. 49

2.16 The crystal structure of TiO_2 in its rutile form (from Moulson and Herbert (2003)). 50

2.17 Coated probe: The metal conductor is a 300 mm long aluminum rod with square cross-section (side length 11.1 mm). 51

2.18 Reflection and transmission coefficient for the coated rod and for an uncoated rod with same metal cross-sectional area. 52

2.19 Weighting functions in x- and y-axis direction (according to Fig. 2.3) for a TRP with $d = 5$ mm, and $D = 30$ mm compared to the weighing functions of two SRPs with $d = 10$ mm and different r_0 . 54

2.20 Setup for the first sensitivity experiment. 55

2.21 Sample trace (bandpass response) from the sensitivity experiment with the perpendicular stick. 56

2.22 Sensitivity experiment with the perpendicular stick. 56

2.23 Setup for the aperture experiment. 57

2.24 Reflection coefficient ρ_{BP} of aperture scatterer vs. radius r_d 58

2.25 Setup for the third sensitivity experiment. 60

2.26 Evaluation of a TDR trace obtained with an SRP (example). 60

2.27 Apparent volumetric water content θ vs. distance r_p 61

2.28 Dielectric constant κ' and $\tan \delta$ vs. frequency f of the agar gel, the agarose gel and deionized water. 65

2.29 Measured dielectric constants of five different agar-gel sand mixtures (dots) as a function of water content, and the calibration curve by Roth et al. (1990). 66

2.30 Setup for the homogeneity experiment. 68

2.31 Relative volumetric water content $\Delta\theta$ as a function of time. 68

2.32 Setup for the calibration in the wet range of soils. 69

2.33 Calibration traces, truncated to the significant part for better display. 70

2.34 Calibration measurements of the relative dielectric constant κ'_{eff} vs. volumetric water content θ 71

3.1	Multislice-Debye soil model: the soil is discretized in N horizontal layers with the Debye parameters $\kappa_0, \kappa_\infty, f_{rel}, \sigma$	74
3.2	Simplyfied multislice-Debye model for soils with a low specific surface area, $A_s = 0 - 100 \text{ m}^2/\text{g}$, where $f_{rel} = 17 \text{ GHz}$ and $\kappa_\infty = 1$ for all layers.	75
3.3	Conductivity σ vs. saturation S as described by Archie's law for $a = 1, \sigma_{el} = 0.01 \text{ mS/m}, c = 4$ and $c = 5, \phi = 0.35, k = 1.88$	76
3.4	Measured example TDR trace $\tilde{r}(t)$ and simulated example TDR trace $r(t)$	77
3.5	TDR100 step signal of the reflectometer used in the experiments, as recorded with the reflectometer itself.	78
3.6	Sample TDR traces of deionized water, measured with a probe with distributed head transition and simulated for a probe without a head transition.	79
3.7	Sample measured and simulated TDR traces for the case $\eta > \eta_{max}$ and $\xi < \xi_{max}$, where $\tilde{t}_{end} < t_{end}$	81
3.8	Sample measured and simulated TDR traces for the case $\eta > \eta_{max}$ and $\xi < \xi_{max}$, where $t_{end} < \tilde{t}_{end}$	81
3.9	The difference function $\Delta r(t)$ is built by subtracting the measured TDR trace $\tilde{r}(t)$ from the simulated TDR trace $r(t)$ in the range of η (example).	83
3.10	Sample measured TDR trace $\tilde{r}(t)$, a sample simulated TDR trace $r(t)$ and the shifted simulated TDR trace $r_b(t)$ with the same t_{end} as \tilde{t}_{end}	84
3.11	Flow chart of the reconstruction algorithm.	85
3.12	Initial setup for the laboratory experiment.	88
3.13	Measured and reconstructed water content profiles of the laboratory experiment after 3 liter, 8 liter and 14 liter of drained water.	88
3.14	Setup of the field site experiment.	89
3.15	Example reconstruction of a field site measured profile, from October 10, 2004.	90
3.16	Example reconstruction of a field site measured profile, from November 10, 2004.	90
4.1	Cross section through a container with a mounted CPS with conductor widths d , center-center distance D , height h , container wall thickness w , container diameter W	94
4.2	CPS on an interface of two media.	94
4.3	Effective dielectric constant κ'_{eff} for the CPS probes of the experiment vs. dielectric constant of the container filling κ'_s , once according to Eq. 4.6, once simulated with the 2-D field solver ANSOFT MAXWELL SV.	97

- 4.4 Measured effective dielectric constant κ'_{eff} for the CPS of the experiment vs. κ'_s measured with the reference TRPs. 98
- 4.5 Energy density around a CPS of the experiment in the vertical cross-section plane. 99

List of Tables

1.1	Van Genuchten parameters for some sand types (unpublished, data by Lehmann, P., Institute of Terrestrial Ecology, ETHZ).	5
1.2	Real relative magnetic permeability μ'_{rel} of selected materials	7
1.3	Electrical conductivity of selected materials	8
1.4	Conductivity of NaCl solutions ($T = 20\text{ }^{\circ}\text{C}$)	8
1.5	Real relative permittivity κ' of selected materials	11
1.6	TDR measurement systems (examples)	27
2.1	Probe configurations for the calculations of ν and α of Figures 2.4 and 2.5.	38
2.2	Debye parameters for some alcohols (Gabriel et al., 1998)	64
2.3	Agar-gel sand mixtures: results of TDR measurements. The volumetric water content θ was determined by drying out a sample of the mixture at $105\text{ }^{\circ}\text{C}$ for 24 h and by scaling the result according to the density of the columns. The real, relative, effective permittivity κ'_{eff} was measured with a TDR dual-rod probe system.	66
3.1	Parameters for the laboratory experiment and the corresponding profile reconstructions.	87
3.2	Parameters for the field experiment and the corresponding profile reconstructions.	89
4.1	Parameters of the experiment with CPS mounted as TDR probes on a container wall.	97

Appendix A

Notation

Terms and short cuts

CPS	coplanar strips
SRP	single-rod probe
TDR	time-domain reflectometry
TRP	two-rod probe

Constants

$\epsilon_0 = 8.85 \cdot 10^{-12}$ As/Vm	Permittivity of vacuum
$\mu_0 = 4\pi \cdot 10^{-7}$ Vs/Am	Permeability of vacuum
$Z_0 = 377$ V/A	Impedance of free space
$c_0 = 3 \cdot 10^8$ m/s	Velocity of light in vacuum
$L = 6.022 \cdot 10^{23}$ mol ⁻¹	Avogadro number
$g = 9.81$ ms ⁻²	Gravitation constant
$j = \sqrt{-1}$	Imaginary Unit

In physics and mathematics the imaginary unit is commonly denoted by “i” whereas in electrical engineering “j” is used

Variables

$\alpha_{d,dB}$	Attenuation in the dielectric coating in dB/m
$\alpha_{c,dB}$	Attenuation in the conductor in dB/m
a	Fitting factor in permittivity model of Roth et al. (1990)
A_s	Specific surface
C'	Capacity per unit length of a wall-mounted CPS
C'_s	Capacity per unit length of a CPS embedded in the measured medium

ϵ^*	Complex permittivity
\vec{E}	Electric field vector
$\underline{\vec{E}}$	Complex amplitude of the electric field vector
E_r	Magnitude of the electric field vector in radial distance
E_z	Magnitude of the electric field vector in z-direction
f	frequency
d	diameter of the conductor(s) or width of the conductors (for CPS)
d_{SRP}	... of an SRP
d_{TRP}	... of a TRP
D	Distance center-center (TRP)
γ^*	Propagation constant
h	Matric head
h_w	Container height
H_ϕ	Magnitude of the azimuthal magnetic field component
κ^*	Complex, relative dielectric constant
κ'	Relative dielectric constant, real part
κ'_a	... of air
κ'_c	... of the container wall
κ'_d	... for the coating of an SRP
κ'_m	... of the soil matric
κ'_s	... of the soil
κ'_w	... of water
κ''	Dielectric constant, imaginary part
κ''_{eff}	Measured relative dielectric constant, real part
κ''_{eff}	Measured relative dielectric constant, imaginary part
k	Full wave number
k_d	in the dielectric coating
k_m	in the conductor
k_s	in the soil
k_z	wave number in z-direction
k_T	transverse wave number
k_{Td}	... in the dielectric coating
k_{Tm}	... in the conductor
k_{Ts}	... in the soil
λ	wave length
l	Side length of polystyrene cube (sensitivity experiments)
L_{SRP}	Length of the SRP rod
L_{TRP}	Length of the TRP rods
ϕ	Porosity
ψ_m	Matric potential

ρ	charge density
ρ_{BP}	reflection coefficient in bandpass response
ρ_S	surface charge density
r	radius or reflection coefficient
r_0	characteristic radius
r_a	radius of the aperture (sensitivity experiments)
r_c	radius of conductor
r_d	radius of SRP probe
r_h	radius of the horn opening
r_p	radial distance of the polystyrene cube (sensitivity experiments)
r_s	radial distance of the steel stick (sensitivity experiments)
R_{skin}	Skin-effect resistance
R	Resistance per meter, Ω/m
R_{TRP}	Resistance per meter, Ω/m , for a TRP
σ_c	Conductivity of the conductor in S/m
$\sigma_{c,SRP}$... of an SRP
$\sigma_{c,TRP}$... of a TRP
S	Degree of saturation
\vec{S}	Poynting vector
S_z	Magnitude of Poynting vector in z-direction
S_T	Magnitude of Poynting vector in transverse direction
$\tan \delta$	Loss tangent
$\tan \delta_d$... of the coating of an SRP
$\tan \delta_s$... of the soil
θ	Volumetric water content
θ_s	Volumetric water content at saturation
θ_r	Residual volumetric water content
t_r	signal rise time
μ	Complex permeability
μ_{rel}	Relative permeability, real part
ω	Angular frequency
v	Velocity of a wave
$v_{loss-less}$	Velocity of a wave in a loss-less medium
v_{SRP}	Velocity of a wave on an SRP
v_{TRP}	Velocity of a wave on a TRP
w	container wall thickness
W	container diameter
w_0	weighting function (sensitivity)
w_c	conductor thickness (for CPS)
w_d	thickness of dielectric coating (SRP)
w_{nf}	weighting function normalization factor
Z^*	Complex impedance

Operators

$$\vec{a} \times \vec{b} = \begin{vmatrix} a_y & b_y \\ a_z & b_z \end{vmatrix} \vec{e}_x + \begin{vmatrix} a_z & b_z \\ a_x & b_x \end{vmatrix} \vec{e}_y + \begin{vmatrix} a_x & b_x \\ a_y & b_y \end{vmatrix} \vec{e}_z$$

$$\nabla = \frac{\partial}{\partial x} \cdot \vec{e}_x + \frac{\partial}{\partial y} \cdot \vec{e}_y + \frac{\partial}{\partial z} \cdot \vec{e}_z \quad \text{Nabla operator}$$

$$\Delta = \nabla^2 = \frac{\partial^2}{\partial x^2} + \frac{\partial^2}{\partial y^2} + \frac{\partial^2}{\partial z^2} \quad \text{Laplace operator}$$

Bibliography

- Abramowitz, M., and I. A. Stegun. 1984. Pocketbook of mathematical Functions. Harri Deutsch.
- Annan, A. P. 1977. Time-domain reflectometry: Air-gap problem for parallel wire transmission lines. Geol. Surv. Can. Pap. 77-1B:59–62.
- Archie, G. 1942. The electrical resistivity log as an aid in determining some reservoir characteristics. Trans. Am. Inst. Mech. Eng. 146(54-61).
- Baker, J., and R. Allmaras. 1990. System for automating and multiplexing soil moisture measurement by time domain reflectometry. Soil. Sci. Soc. Am. J. 54(1).
- Bächtold, W. 1994. Lineare Elemente der Höchstfrequenztechnik. vdf, Zürich.
- Bussian, A. E. 1983. Electrical conductance in a porous medium. Geophysics 48:1258–1268.
- Castaglione, P., and P. Shouse. 2003. The effect of ohmic losses on TDR measurements of electrical conductivity. Soil. Sci. Soc. Am. J. 67:414–424.
- Chan, C., and R. J. Knight. 2001. Laboratory measurements of electromagnetic wave velocity in layered sands. Water Resources Research 37(4):1099–1105.
- Cole, K., and R. Cole. 1941. Dispersion and adsorption in dielectrics. J. Chem. Phys. 9:341–351.
- Davis, J., and W. Chudobiak. 1975. In situ meter for measuring relative permittivity of soils. Geol. Surv. Can. Pap. 75(1A):75–79.
- Debye, P. 1929. Polar Molecules. Chemical Catalog Company, New York.
- Dirksen, C., and S. Dasberg. 1993. Improved calibration of time domain reflectometry soil water content measurements. Soil. Sci. Soc. Am. J. 57:660–667.

- Dobson, M., F. Ulaby, M. Hallikainen, and M. El-Rayes. 1985. Microwave dielectric behaviour of wet soil. Part II: Dielectric mixing models. *Ieee Trans. on Geoscience and Remote Sensing* 23:35–46.
- Fellner-Feldegg, H. 1969. The measurement of dielectrics in the time domain. *J. Phys. Chem.* 73:616–623.
- Fellner-Feldegg, H., and E. Barnett. 1970. Reflection of a voltage step from a section of transmission line filled with polar dielectric. *J. Phys. Chem.* 74(9):1962–1965.
- Feng, W., and C.-P. Lin. 1999. Theoretical model of a multisection time domain reflectometry measurement system. *Water Resources Research* 35(8):2321–2331.
- Friel, R., and D. Or. 1999. Frequency analysis of time-domain reflectometry (TDR) with application to dielectric spectroscopy of soil constituents. *Geophysics* 64:1–12.
- Fujiyasu, Y., and C. Pierce. 2004. High dielectric insulation coating for time domain reflectometry soil moisture sensor. *Water Resources Research* 40(W04602).
- Gabriel, C., G. S., E. H. Grant, B. J. Halstead, and D. M. P. Mingos. 1998. Dielectric parameters relevant to microwave dielectric heating. *Chemical Society Reviews* 27:213–223.
- Giese, K., and R. Tiemann. 1975. Determination of the complex permittivity from a thin sample time-domain reflectometry, improved analysis of the step response waveform. *Adv. Molec. Relax. Processes* 7:45–59.
- Goubau, G. 1950. Surface waves and their application to transmission Lines. *Journal of Applied Physics* 21:1119–1128.
- Goubau, G. 1954. Designing Surface-Wave Transmission Lines. *Electronics* April:180–184.
- Gupta, K., R. Garg, and I. J. Bahl. 1979. *Microstrip lines and slotlines*. Artech.
- Hafner, C. 1999. *MaX-1: A Visual Electromagnetics Platform for PCs*. John Wiley & Sons, Chichester.
- Harms, F. 1907. Electromagnetic waves on dielectrically coated wires. (In German.) *Ann. d. Phys.* 23(4):44–60.
- Hasted, J. 1973. *Aqueous Dielectrics*. Chapman & Hall, London.
- Heimoaara, T. J. 1994. Frequency domain analysis of the complex dielectric permittivity of soils. *Water Resources Research* 30:189–199.

- Heimovaara, T. J., and W. Bouten. 1990. A Computer-Controlled 36-Channel Time Domain Reflectometry System for Monitoring Soil Water Contents. *Water Resources Research* 26(10):2311–2316.
- Heimovaara, T. J., and E. de Water. 1993. A computer controlled TDR system for measuring water content and bulk electrical conductivity of soils. Rep. 41 Laboratory of Physical Geography and Soil Science, University of Amsterdam.
- Hoekstra, P., and A. Delaney. 1974. Dielectric properties of soils at UHF and microwave frequencies. *J. Geophys. Res.* 79:1699–1708.
- Hunt, A. G. 2004. Continuum percolation theory and Archie's law. *Geophysical Research Letters* 31(L19503):1–4.
- Kaden, H. 1951. Advances in the theory of waves on wires. (In German.) *Arch. elektr. Übertragung* 5:399–414.
- Knight, J. H. 1992. Sensitivity of time domain reflectometry measurements to lateral variations in soil water content. *Water Resources Research* 28(9):2345–2352.
- Kunz, H. Die Anregung von Goubauwellen durch unvollständig abgeschirmte Koaxialkabel Ph. d. ETH Zürich 1972.
- Laurent, J.-P., and L. A. Pereira dos Santos Une nouvelle méthode de détermination des profils de teneurs en eau dans les sols par inversion d'un seul signal de réflectométrie temporelle (TDR) 1994.
- Lin, C.-P. 2003a. Analysis of nonuniform and dispersive time domain reflectometry measurement systems with application to the dielectric spectroscopy of soils. *Water Resources Research* 39(1):1012.
- Lin, C.-P. 2003b. Frequency Domain Versus Travel Time Analysis of TDR Waveforms for Soil Moisture Measurements. *Soil. Sci. Soc. Am. J.* 67:720–729.
- Moulson, A. J., and J. M. Herbert. 2003. *Electroceramics*. John Wiley & Sons.
- Mualem, Y., and S. P. Friedman. 1991. Theoretical prediction of electrical conductivity in saturated and unsaturated soil. *Water Resources Research* 27:2771–2777.
- Nadler, A., S. Dasberg, and I. Lapid. 1991. Time domain reflectometry measurements of water content and electrical conductivity of layered soil columns. *Soil. Sci. Soc. Am. J.* 55:938–943.
- Or, D., and V. Rasmussen. 1999. Effective frequency of TDR travel time-based measurement of bulk dielectric permittivity. Third Workshop on Electromagnetic Wave Interaction with Water and Moist Substances, Athens, GA..

- Oswald, B., W. Bächtold, H. Flühler, and H. Benedickter. 2003. Spatially resolved water content profiles from inverted time domain reflectometry signals. *Water Resources Research* 39(12):1357.
- Oswald, B., H. Benedickter, W. Bächtold, and H. Flühler. 2004. A single rod probe for time domain reflectometry. *Vadose Zone Journal*. Accepted for publication.
- Petersen, L., A. Thomsen, P. Moldrup, O. Jacobsen, and D. Rolston. 1995. High-resolution time domain reflectometry: Sensitivity dependency on probe design. *Soil. Sci.* 159:149–154.
- Ramo, S., J. R. Whinnery, and T. Van Duzer. 1993. *Fields and Waves in Communication Electronics*. John Wiley & Sons, Inc.
- Revil, A., L. M. Cathles, S. Losh, and J. A. Nunn. 1998. Electrical conductivity in shaly sands with geophysical application. *J. of Geophysical Research* 103(23):925–936.
- Robinson, D. A., S. B. Jones, J. M. Wraith, D. Or, and S. P. Friedman. 2003. A review of advances in dielectric and electrical conductivity measurements in soils using time domain reflectometry. *Vadose Zone Journal* 2:444–475.
- Roebuck, B. D., and S. Goldblith. 1975. Dielectric properties at microwave frequencies of agar gels. Similarity to the dielectric properties of water. *Journal of Food Science* 40:899.
- Roth, K., R. Schulin, H. Flühler, and W. Attinger. 1990. Calibration of time domain reflectometry for water content measurement using a composite dielectric approach. *Water Resources Research* 26:2267–2273.
- Santamarina, J. C., K. A. Klein, and M. A. Fam. 2001. *Soils and Waves*. John Wiley & Sons Ltd, Chichester.
- Savitzky, A., and M. J. E. Golay. 1964. Smoothing and differentiation of data by simplified least squares procedures. *Analytical Chemistry* 36:1627–1639.
- Schaap, M., D. A. Robinson, M. Friedman, and A. Lazar. 2003. Measurement and modeling of the dielectric permittivity of layered granular media using time domain reflectometry. *Soil. Sci. Soc. Am. J.* 67:1113–1121.
- Sen, A. D., V. G. Anicich, and T. Arakelian. 1992. Dielectric constant of liquid alkanes and hydrocarbon mixtures. *J. Phys. D.: Appl. Phys.* 25:516–521.
- Sommerfeld, A. 1899. About the propagation of electrodynamic waves along a wire. (In German.) *Ann. d. Phys.* 67(3):233–290.
- Stern, O. 1924. Zur Theorie der elektrischen Doppelschicht. *Z. Elektrochem.* 30:508–516.

- Stratton, J. A. 1941. *Electromagnetic theory*. McGraw-Hill Book Company, Inc., New York.
- Strickland, J. 1970. *Time-domain reflectometry measurements*. Tektronix Inc., Beaverton, OR.
- Todoroff, P., and J.-D. Sun Luk. 2001. Calculation of in situ soil water content profiles from TDR signal traces. *Institute of Physics Publishing, Measurement Science and Technology* 12:27–36.
- Todoroff, P., R. Lorion, and J.-D. Lan Sun Luk. 1998. L'utilisation des algorithmes génétiques pour l'identification de profils hydrique de sol à partir de courbes réflectométriques. *C. R. Acad. Sci. Paris, Sciences de la terre et des planètes* (327):607–610.
- Topp, G., J. Davis, and A. Annan. 1980. Electromagnetic determination of soil water content: Measurements in coaxial transmission lines. *Water Resources Research* 16(3):574–582.
- Topp, G., S. Zegelin, and I. White. 2000. Impact of real and imaginary components of relative permittivity on time domain reflectometry measurements in soils. *Soil. Sci. Soc. Am. J.* 64:1244–1252.
- van Gemert, M. 1973. High-frequency time-domain methods in dielectric spectroscopy. *Philips Res. Rep.* 28:530–572.
- Weast, R. C. 1988. *CRC Handbook of Chemistry and Physics*. CRC Press, Boca Raton.
- Weerts, A. H., J. A. Huisman, and W. Bouten. 2001. Information content of time domain reflectometry waveforms. *Water Resources Research* 37(5):1291–1299.
- Yanuka, M., G. Topp, S. Zegelin, and W. D. Zebchuk. 1988. Multiple Reflection and Attenuation of Time Domain Reflectometry Pulses: Theoretical Considerations for Applications to Soil and Water. *Water Resources Research* 24(7):939–944.
- Zinke, O., and H. Brunswig. 2000. *Hochfrequenztechnik 1*. Springer Verlag.

Curriculum Vitae

Surname	Nussberger
First Name	Mathis
Date of birth	11 September 1972
Citizen of	Zürich
School education	1988-1993 Mathematisch-Naturwissenschaftliches Gymnasium Rämibühl, Zürich Matura Typus C
Military service	1993
Higher education	1993-1998 Studies in electrical engineering, Swiss Federal Institute of Technology (ETH) Zürich
	1998 Diploma in electrical engineering (Dipl. El.-Ing. ETH)
	2001-2005 PhD-Studies in technical engineering, ETH Zürich
	2002-2004 Post diploma study in medicine physics, ETH Zürich
Occupation	1998-1999 Motorola AG, Hägendorf, RF lab
	1999-2001 Elektrobot AG, Bubikon, RF development
	2001-2005 Research and teaching assistant, ETH Zürich

